In presenting the dissertation as a partial fulfillment of the requirements for an advanced degree from the Georgia Institute of Technology, I agree that the Library of the Institute shall make it available for inspection and circulation in accordance with its regulations governing materials of this type. I agree that permission to copy from, or to publish from, this dissertation may be granted by the professor under whose direction it was written, or, in his absence, by the Dean of the Graduate Division when such copying or publication is solely for scholarly purposes and does not involve potential financial gain. It is understood that any copying from, or publication of, this dissertation which involves potential financial gain will not be allowed without written permission.

7/25/68

ENERGY TRANSFER IN COLLISIONS OF SMALL MOLECULES

A THESIS

Presented to

The Faculty of the Division of Graduate Studies and Research

By

Frederick Cecil Petty

In Partial Fulfillment

of the Requirements for the Degree

Doctor of Philosophy

in the School of Chemistry

Georgia Institute of Technology

March, 1971

ENERGY TRANSFER IN COLLISIONS OF SMALL MOLECULES

Approved:

[redacted]

Date approved by Chairman: March 29, 1971

ACKNOWLEDGMENTS

I got by with a little help from my friends:

My deepest gratitude goes to my advisor, friend, and scientific guru, Dr. Tom Moran, whose example and instruction got me through graduate school. Without his help this thesis would not exist.

I thank Dr. Peter Sherry and Dr. Ray Borkman for serving on my thesis reading committee.

I thank Mr. Malcolm Rucker for working wonders with primitive machine tools, Mr. Jerry O'Brien for being the best electronics technician in the world, and Mr. Don Lillie for finding time to blow glass and play volleyball when I needed it.

The help of my ionic colleagues, Dave Fullerton, Fred Hedrick, Phil Cosby, and George Turner, was invaluable.

I appreciate Dr. William Spicer's interest and help, especially in granting me a teaching assistantship; and I thank NASA for three years as a trainee.

Most of all, I thank Karen for everything.

TABLE OF CONTENTS

TABLE OF CONTENTS (Continued)

LIST OF TABLES

LIST OF ILLUSTRATIONS

LIST OF ILLUSTRATIONS (Continued)

LIST OF ILLUSTRATIONS (Continued)

SUMMARY

Inelastic collisions of small molecules were studied at two energetic extremes. High energy (2000 eV) collision induced dissociations of N_2^+, O_2^+, CO^+, and NO^+ were studied as a function of reactant ion internal energy by varying the kinetic energy of the ionizing electrons used to produce the reactant ions. Relative cross sections and product ion velocity distributions were obtained with a mass spectrometric apparatus. Dissociation was found to proceed via collision induced Franck-Condon type electronic transitions to repulsive portions of the molecular ion potential energy curves. This determination of the diatomic ion dissociation mechanism permitted determination of the internal energy of CO^+ and NO^+ ions resulting from unimolecular decomposition of triatomic ions.

Inelastic energy losses in low energy (16 eV) collisions of H_3^+ with Ne were measured in a tandem mass spectrometer designed to direct mass analyzed ion beams onto target molecules and scan the energy, mass, and angular distribution of charged interaction products. The experimental energy loss spectra correspond to that expected for vibrational excitation of H_3^+, and frequencies obtained from these inelastic energy data are found to agree with recent quantum mechanical calculations reported in the literature.

A similar investigation examined energy conversion in vibrationally inelastic, low energy CO^+ and Ar collisions with a higher resolution, ion impact spectrometer. In this apparatus a CO^+ beam interacts with a neutral Ar beam and the energy, mass, and angular distribution of scattered CO^+ is measured. Energy loss spectra were obtained for 1.56 to 25.5 eV incident CO^+ kinetic energy and 0 to 25 degrees laboratory scattering angle, and maxima in these spectra occur at energies corresponding to the known CO^+ spectroscopic vibrational spacings. The probabilities for multiquantum transitions were found to increase with both incident ion kinetic energy and scattering angle. Cross sections for vibrational excitation at small scattering angles are adequately described by a semiclassical oriented nonlinear encounter model in which an impact parameter treatment is used to estimate collisional energy transfer for a forced oscillator and time dependent wavefunctions are employed to evaluate transition probabilities. The energy widths of these inelastic peaks indicate simultaneous vibrational-rotational excitation to occur. Weakly inelastic processes are observed below the threshold for vibrational excitation, corresponding to pure rotational excitation of CO^+. The relative importance of rotational transitions increases with decreasing energy and scattering angle.

CHAPTER I

INTRODUCTION

A collision of a molecule ion with a neutral target atom or molecule proceeds in either an inelastic or elastic manner. In the former case, translational energy is conserved during the collision and the colliding entities retain their internal energy states. In the latter case, transfer between translational and internal energy occurs, i.e. some kinetic energy of the incident molecule is converted into electronic, vibrational, and/or rotational excitation. Collision-induced dissociation or ion-molecule reaction (mass transfer) may also result from inelastic collision.

Beam experiments provide an excellent method for study of inelastic collisions since the kinetic and internal energy of the incident molecule ion may be precisely specified, and the mass, scattering angle, and kinetic energy of charged interaction products may be determined. Knowledge of these data enable the testing of theoretical models for the collision process. To attempt an understanding of their mechanisms, ion-neutral collisions were studied at two energetic extremes in the present work.

At high energies (2000 eV), collisions of diatomic

molecules lead to their dissociation. The product atomic ions emerge with velocity distributions determined by the potential energy curves, internal energy states, and electronic transitions of the molecule ions. Gas phase, electron impact ionization produces molecule ions in selected internal energy states, and a mass spectrometric apparatus measures the velocity distributions of charged dissociation products. Thus one may seek to answer the question: Do diatomic molecule ions dissociate in high energy collisions via Franck-Condon type transitions? Understanding diatomic molecule ion collision-induced dissociation then allows determination of the internal energy of NO^+ and CO^+ formed by unimolecular decomposition of triatomic ions.

At low energies (2-25 eV), inelastic collisions excite vibrational and rotational transitions, with collisional kinetic energy loss determined by the molecular vibrational and rotational energy levels. Ion impact spectroscopy can therefore be used to measure vibrational frequencies whose optical determination is difficult, such as those of H_3^+. In the present work the kinetic energy loss of H_3^+ colliding with Ne at low energies was measured. Since several theoretical calculations of H_3^+ vibrational frequencies have been reported, this work provides a test of their validity.

In cases where vibrational frequencies are well known, experimental energy loss spectra can test the applicability of theoretical models of vibrational excitation by

collision. For this purpose, inelastic collisions of CO^+ with Ar were examined at 2 to 25 eV incident CO^+ kinetic energies and 0 to 20 degrees laboratory scattering angles, and an oriented nonlinear encounter model was used to calculate predicted transition probabilities for comparison with the experimental energy loss spectra.

CHAPTER II

COLLISION INDUCED DISSOCIATION OF DIATOMIC MOLECULE IONS AT HIGH ENERGIES

Introduction

Collision induced dissociations of 2000 eV N_2^+, O_2^+, CO^+, and NO^+ ions were studied as a function of reactant ion internal energy. Relative cross sections and product ion velocity distributions for dissociative scattering processes through angles less than two degrees were examined as a function of reactant ion internal energy by changing the kinetic energy of the ionizing electrons. Product ion velocity distributions are consistent with a mechanism that assumes Franck-Condon type transitions between electronic states of the reactant species. These dissociative reactions involving diatomic molecule ions have been used to probe the internal energy of NO^+ and CO^+ ions resulting from the unimolecular decomposition of triatomic molecule ions formed by electron impact ionization.

The collision induced dissociation of molecular ions has been the subject of a number of investigations over the years (1-8). However, most of these studies have examined the dissociation of H_2^+ ions because of the accurate theoretical data available (9-14) on this system and the intrinsic

interest in establishing its high energy reaction mechanism. Another impetus for these investigations has been the practical application (15) of the corresponding D_2^+ dissociative reactions in magnetic mirror traps of thermonuclear devices. A study of these H_2^+ collisions in the 5-80 keV energy range has shown (16) that scattering of the H^+ and H reaction products takes place predominantly through small angles and corresponds to electronic excitation of the $H_2^+ \Sigma_g$ molecule ion to the Σ_u repulsive curve. The angular distributions of the reaction products are in harmony with the assumption of vertical Franck-Condon type transitions (17) and the momentum distributions measured at specified angles (18,19) are quite sensitive to the initial vibrational population distributions of the reactant H_2^+ ions. Similar dissociative reactions of polyelectron ions have been investigated using standard techniques (20-23) of mass spectrometry. Product ions from such collision induced dissociations give rise to relatively diffuse, low intensity peaks (Aston Bands) appearing at both integral and nonintegral mass numbers. These very broad ion peaks are similar to those from metastable transitions of polyatomic ions undergoing unimolecular decomposition (24,25). In order to understand the mechanisms of high energy reactions and to gain information on the internal energy of ions formed via electron impact ionization, dissociative transitions of diatomic molecule ions have been examined.

Apparatus

The experimental arrangement used in this work is shown schematically in Figure 1. Ions are formed in an electron bombardment source with the electron beam energy in the ionization region (26) controlled from 2 to 150 eV. The absolute energy of the electrons in the ion source region was calibrated during each experiment by comparison of our experimental ionization efficiency curves with those tabulated in the literature (27). Voltages applied across a series of accelerating plates focus ions produced in the source into the collision chamber. The reactant ion beam emerges from the final accelerating slit with 2000 eV kinetic energy and passes into a collision chamber containing neutral target gas molecules.

The length of the collision chamber shown in Figure 1 is 5.0 inches and the width of the acceptance angle defining slit nearest the ion source is 0.030 inch and that of the second 0.060 inch. The distance between these two slits is 3.5 inches with the average ion-neutral molecule interaction occurring in the center of the collision region, thus defining respective acceptance angles of 0.30 and 1.75 degrees in the directions perpendicular and parallel to the longitudinal axis of the second slit. The port of the pumping system is located between the two acceptance angle defining slits and maintains a differentially pumped region between the collision chamber and the magnetic analyzer.

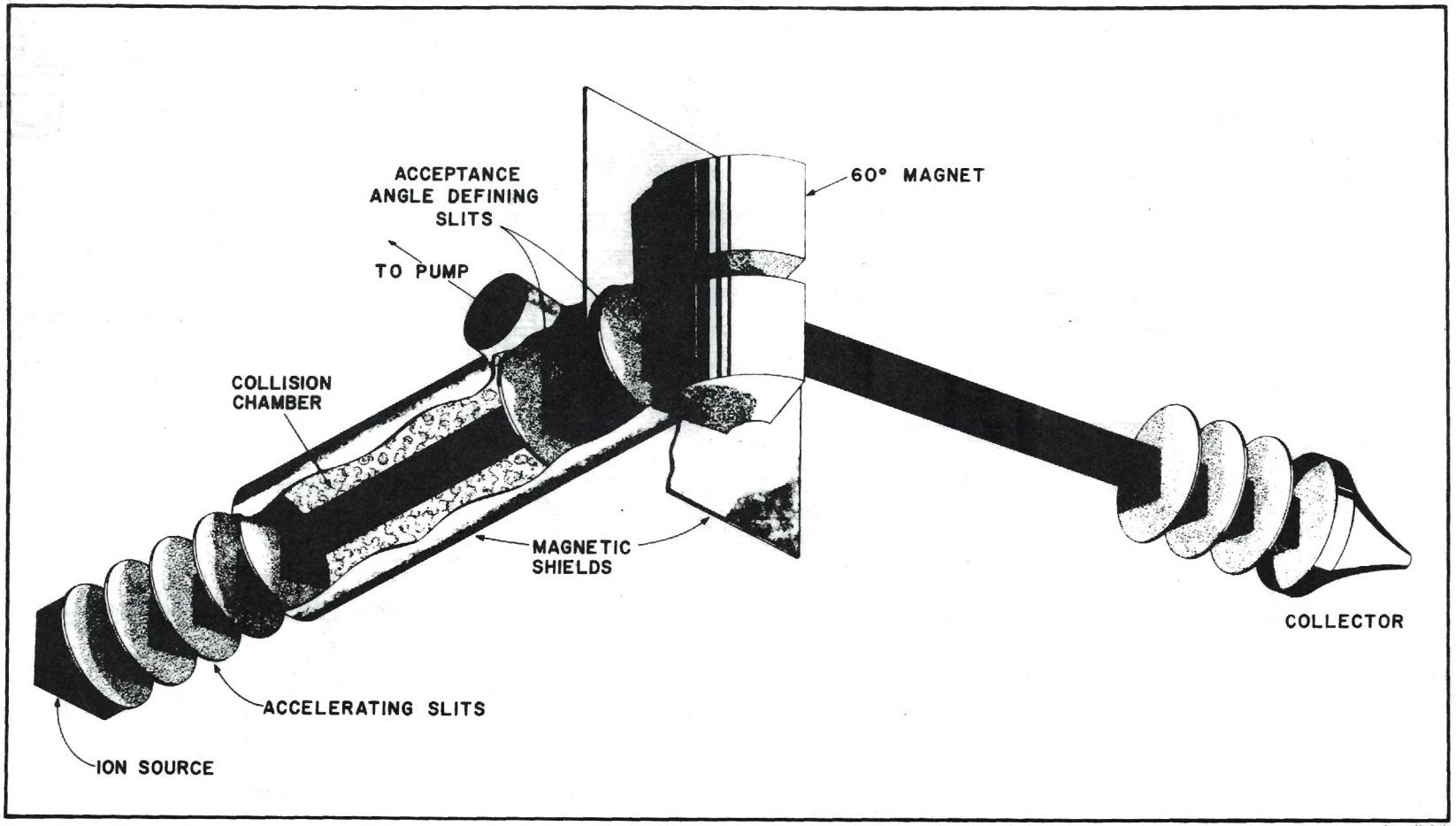

Figure 1. Schematic Diagram of the Experimental Apparatus Used to Study High Energy Collision-Induced Dissociation.

Method

Velocity dependent discrimination (21,28) by mass spectrometer slit systems has been considered in the comparison of measured and calculated product ion momentum distributions. The acceptance angle defining slits insure that product ion beams entering into the magnet are spatially defined and can be momentum analyzed in the magnet, thereby allowing the corresponding energy distributions to be determined. Atomic ions recoiling with only a few electron volts in the molecular domain can give rise to large energy spreads in the laboratory system. Purser et al. (29) have pointed out that, in the dissociative transition of H_2^+ from the bound $\sum_g$ state to the repulsive $\sum_u$ state, the potential energy of the system at the initial internuclear spacing can be transformed into translational energy of the separating products, giving them a component of velocity u in the center of mass system. When u is directed at 0 or 180 degrees with respect to the reactant ion beam direction, the product ions are formed with respective energies E^+ and E^- given by

$$E^{\pm} = \tfrac{1}{2}m(u \pm V_o)^2 \qquad (1)$$

where m is the mass of the neutral atom. V_o and u are the respective velocities in the laboratory and center of mass systems. $E_o = \tfrac{1}{2}mV_o^2$ and $E_1 = \tfrac{1}{2}mu^2$. The energy spread E of

the product ions is

$$\Delta E = E^{+} - E^{-} = 4(E_o E_1)^{\frac{1}{2}}. \qquad (2)$$

Energy spreads of several hundred volts are typical when 2000 eV reactant projectiles are used.

Ions undergoing dissociation after acceleration but prior to analysis in the magnetic field are focused at an apparent mass corresponding to

$$(m/q)^{*} = (m_f/q_f)^2/(m_i/q_i) \qquad (3)$$

where m_f/q_f is the mass to charge ratio of the final product ion and m_i/q_i is the mass to charge ratio of the initial reactant ion (21,25,30). Similar transitions giving rise to nonintegral masses have been observed (31) in the unimolecular decomposition of excited polyatomic ions. However, for all systems reported in the present work, a linear relationship between the product/reactant ion intensity ratio and the collision chamber pressure was observed. Such behavior is characteristic of bimolecular reactions and is illustrated in Figure 2 for the nitrogen reaction, a typical case.

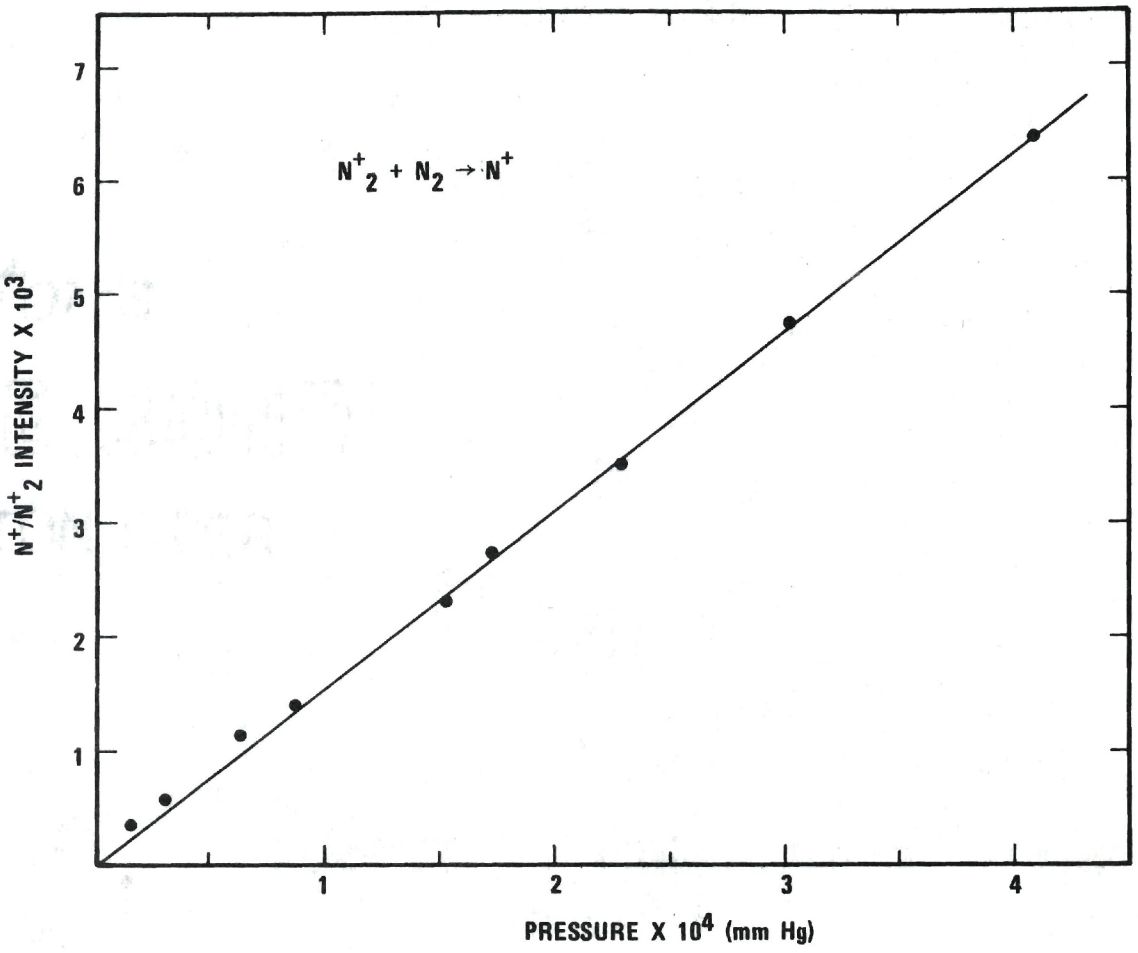

Figure 2. Ratio of N^+/N_2^+ Ion Intensities as a Function of Nitrogen Gas Pressure in the Collision Region.

Results and Discussion

N_2^+

The product N^+ ions formed by the reaction

$$N_2^+ + N_2 \rightarrow N^+ + N + N_2 \qquad (4)$$

were monitored at an apparent mass $(m/q)^*$ of 7.0. According to equation 3, the peak appearing at $(m/q)^* = 7.0$ unambiguously identifies both the ionic reactants and products in reaction 4. The momentum spread of this peak has been measured with the aid of carefully calibrated electrostatic and magnetic fields using techniques previously outlined (17, 21). The velocity distributions of the N^+ product ions have been determined from these momentum measurements and are presented as the solid lines in Figure 3 for various ionizing electron energies.

In order to elucidate the reaction mechanism of dissociative reactions, a comparison of the experimentally measured product ion velocity distributions with those predicted on the basis of collision induced electronic transitions of the reactant ions has been made. The number of product ions formed by reaction 4 per unit target gas density and unit path length in the collision region is

$$N(R,\phi)dRd\phi = 2\pi D(R)\sigma(R,\phi)\sin\phi dRd\phi \qquad (5)$$

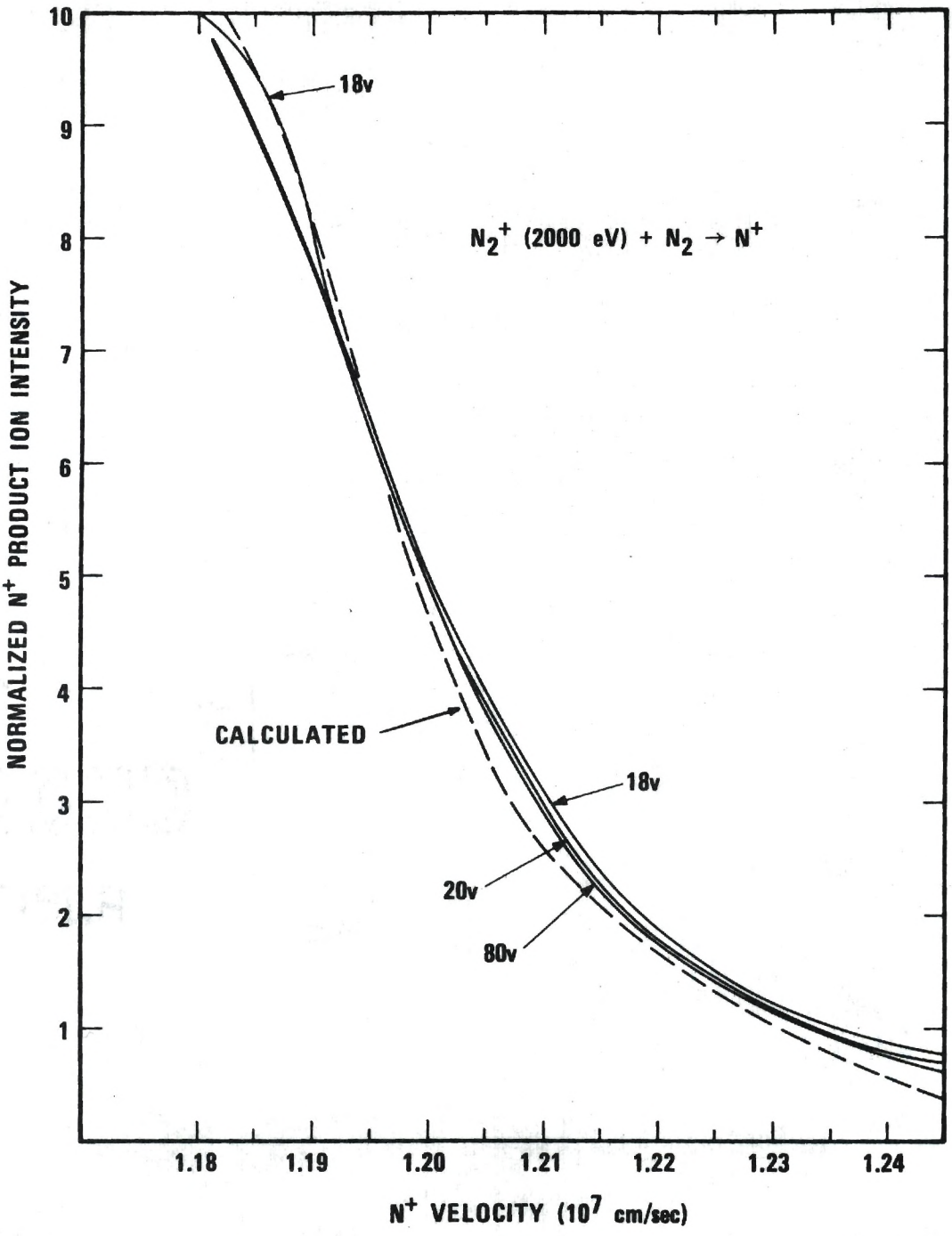

Figure 3. Experimental—— and Calculated---- N^+ Product Ion Intensities as a Function of N^+ Velocity in the Laboratory System. (The Experimental N^+ Product Ion Curves are Presented for Primary Reactant Ions Formed Via Ionization of N_2 with 18, 20, and 80 volt electrons.)

where D(R) is the distribution of reactant N_2^+ ions as a function of internuclear distance R, and ϕ is the angle between the incident velocity vector V_o of the reactant ion beam and the N_2^+ internuclear axis. $\sigma(R,\phi)$ is the cross section for dissociation at given R and ϕ. The vector relationship for this model of the dissociation process is given in Figure 4. As a result of the dissociation of N_2^+, both the N^+ and N fragments emerge from the collision with a velocity u characteristic of two-body breakup in the center of mass system. The shape of the N_2^+ repulsive potential energy curve determines the relationship between u and R and enables $N(R,\phi)$ to be expressed in terms of u and ϕ:

$$2\pi D(R,\phi)\sigma(R,\phi)\sin\phi d\phi dR = 2\pi N(u,\phi)du\sin\phi d\phi. \qquad (6)$$

From equation 6, the number distribution of product ions in the center of mass system is given by

$$N(u,\phi) = D(R,\phi)\sigma(R,\phi)\left(\frac{dR}{du}\right). \qquad (7)$$

Using the vector diagram in Figure 4, it can be shown (17) that the Jacobian of transformation between the center of mass coordinates (u,ϕ) and the laboratory coordinates (V,θ) is

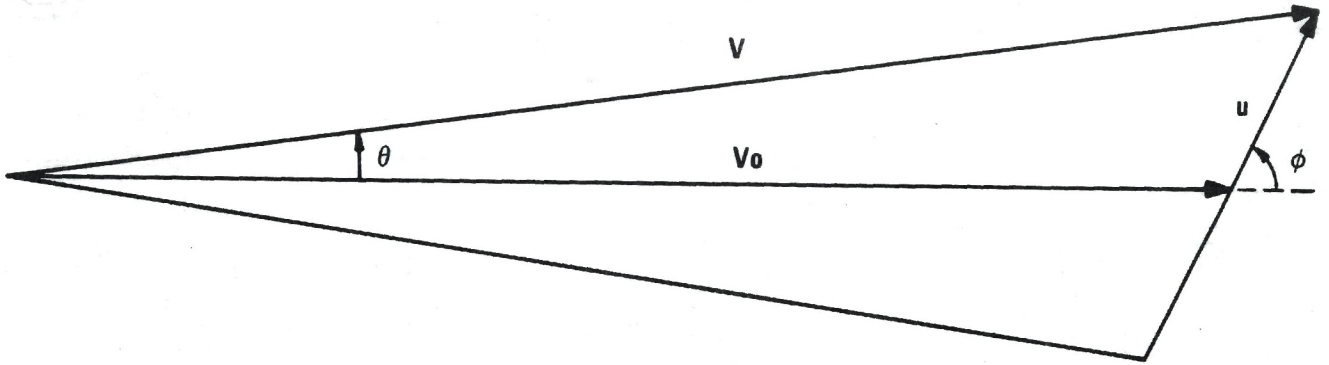

Figure 4. Vector Diagram of the Ionic Dissociation Process. (θ is the Laboratory Scattering Angle, ϕ is the Angle between the Reactant Ion Internuclear Axis and the Initial Direction of the Ion Beam, u is the Dissociation Velocity of the Atomic Ion with Respect to its Center of Mass, V_o is the Initial Velocity of the Reactant Ion Beam, and V is the Resultant Product Ion Velocity.)

$$\frac{\partial(\cos\phi,u)}{\partial(\cos\theta,V)} = \left(\frac{V}{u}\right)^2 . \qquad (8)$$

This allows $N(u,\phi)$ to be related explicitly to the number distribution $P(V,\theta)$ of product ions in the laboratory system through the expression

$$P(V,\theta) = D(R)\sigma(R,\phi)\left(\frac{dR}{du}\right)\left(\frac{V}{u}\right)^2 . \qquad (9)$$

The reactant ion internuclear distance is taken to be constant during the transitions, which are assumed to be vertical Franck-Condon type transitions to repulsive potential energy surfaces. dR/du is determined from the shape of the repulsive curves.

The statistical distribution $D(R)$ of ions as a function of R is determined by the initial population distributions of ions formed by electron impact ionization and by the spontaneous transitions that occur within 6×10^{-6} second, the time required for reactant ions to travel from the source to the collision region. The vibrational population of different electronic states initially produced in the ionization process can be estimated using the Born-Oppenheimer approximation. The probability of transition from vibrational level v' of electronic state i of a diatomic molecule to vibrational level v" of the electronic

state j is

$$P_{iv',jv''} \sim \left| \int \psi_{v'} R^{e}_{ij}(R,\underline{r}) \psi_{v''} dR \right|^2, \qquad (10)$$

where $\psi_{v'}$ and $\psi_{v''}$ are the vibrational wavefunctions corresponding to levels v' and v" respectively and $R^{e}_{ij}(R,\underline{r})$ is the electronic transition moment (32).

$R^{e}_{ij}(R,\underline{r})$ is a slowly varying function of R and its average value can be taken outside (33) the integral giving

$$P_{iv',jv''} \sim \left[R^{e}_{ij}(\bar{R}_{v',v''}) \right]^2 \left| \int \psi_{v'} \psi_{v''} dR \right|^2. \qquad (11)$$

Therefore, the probabilities $P_{iv',jv''}$ will be determined essentially by the square of the vibrational overlap integrals. These integrals have been calculated using both Morse anharmonic oscillator (34) and RKR vibrational wavefunctions (35) for the excited N_2^+ states. The RKR wavefunctions are more nearly accurate than the Morse functions, but adequate (36-38) overlap integrals can be calculated from the latter if the former are not available. Although vibrational distributions of the ions excited by electron impact ionization can thus be estimated, electronic transition moments are also needed to calculate $P_{iv',\ jv''}$. Published photoionization data have been used (34,39) to calculate the electronic transition moments and it is found

that relative populations of the $N_2^+ X^2\Sigma_g$, $A^2\Pi_u$, and $B^2\Sigma_u$ states are 0.4, 0.5, and 0.1 respectively, which values are confirmed by recent (37,40) photoelectron measurements. Relative electron impact ionization cross sections estimated (41) from optical oscillator strengths and electron scattering experiments tend to weight the $N_2^+ X^2\Sigma_g$ state more heavily than the $A^2\Pi_u$ state, but these results agree with the photoionization data in assigning minor importance to the $N_2^+ B^2\Sigma_u$ state. Spectroscopic analysis of nitrogen excitation by 1MeV protons (42) has also indicated that the probability for formation of $N_2^+ {}^2\Sigma_u$ ions is small. Furthermore, the B state undergoes spontaneous radiative decay (43,44) within 6×10^{-8} second, a shorter time than that required for the ions to reach the collision region in the apparatus. This transition populates the lower vibrational levels of the X state since the B$\rightarrow$X vibrational overlap integrals strongly weight (35) the $N_2^+ X^2\Sigma_g$ (v=0,1) levels. Analogously, the $A^2\Pi_u$ state has a lifetime of 3×10^{-6} second (39) and the A$\rightarrow$X spontaneous radiative transitions occurring prior to ion-molecule reaction populate the lower vibrational levels of the $X^2\Sigma_g$ state. Thus, the major portion of the reactant ion beam in the collision region is in the $X^2\Sigma_g$ (v=0,1) levels.

An estimate of the number distribution D(R) has been made using the above transition moments, spontaneous radiative lifetimes, and vibrational overlap integrals. D(R) is

shown as the darkened area in Figure 5 along with the relevant potential energy curves (45). The range of R over which D(R) contributes significantly to the collision induced dissociation process is shown as the shaded Franck-Condon region in this figure. These collision induced electronic transitions are assumed to occur from the $X^2\Sigma_g$ state to the repulsive portion of the $D^2\Pi$ state of the ion and equation 9 is used to calculate the velocity distribution of N^+ product ions, with the cross section σ considered to be independent of R and ϕ in this calculation. This calculated N^+ product ion velocity distribution is shown as the dashed curve in Figure 3 along with the experimentally measured curves. Only one reaction mechanism, involving electronic transitions to the $D^2\Pi$ state, need be invoked to obtain agreement between measured and calculated product ion velocity distributions, but transitions to other states (45) are not entirely excluded. Transitions to the repulsive portion of the $D^2\Pi$ states by electron impact ionization of nitrogen have been suggested (46) to rationalize the low N^+ appearance potential; however, transitions to other states occur (47) at higher electron energies. N^+ is produced with an almost isotropic distribution by electron impact dissociation and a similar angular dependence is expected (48) in these experiments because of the symmetry (18) of the states involved.

Although the experimental velocity distributions in

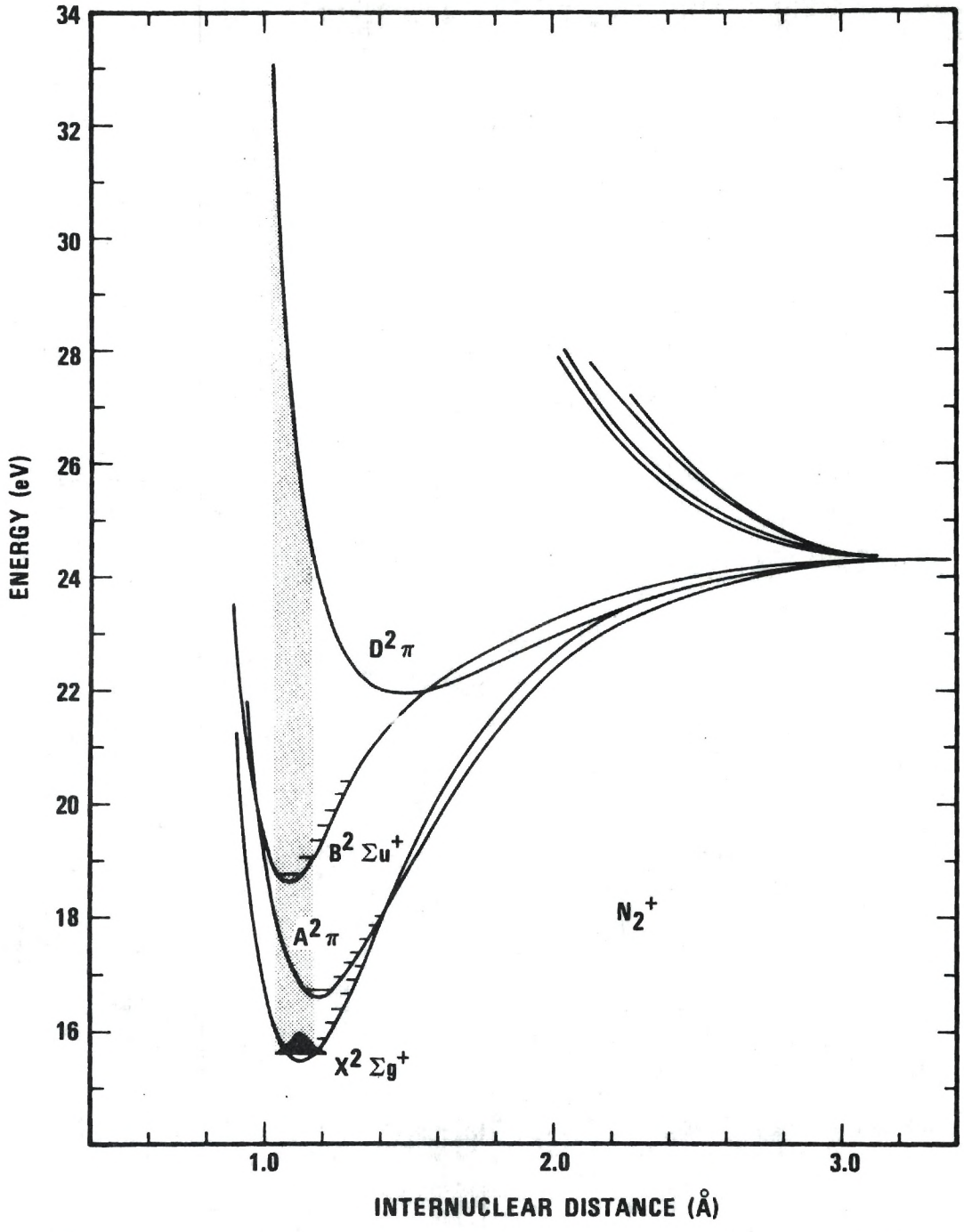

Figure 5. Potential Energy Curves of N_2^+. (See Reference 45. The Shaded Region from the X to the D State Indicates Values of Internuclear Distance Used to Calculate the N^+ Product Ion Velocity Distributions Given in Figure 3.)

Figure 3 are consistent with dissociation via X→D transitions, a critical test of the participation of long-lived excited states can be made by varying the energy of the ionizing electron beam. The results of this experiment are shown in Figure 6. The N^+(product)/N_2^+(reactant) ratios are proportional to the reaction cross section. The N_2^+ ionization efficiency curve, given by the solid circles, extrapolates to the 15.58 eV nitrogen ionization potential and provides an internal check on the energy of the electron beam. From 15.58 to 21 eV the N^+/N_2^+ ratio is constant, as expected if the A→X and B→X spontaneous radiative transitions occur prior to reaction. However, this ratio starts to increase at approximately 21 eV, which corresponds to the appearance potential of the N_2^+ quartet states (45). These states contribute to the ion-molecule reactions (49, 50) producing N_3^+ and their lifetimes (51) are longer than $3x10^{-6}$ second. The 10 percent increase in cross section can be attributed to their reactions. Since the reactant ion beam is almost entirely composed of X state ions, a very large cross section is indicated for dissociative reactions of these quartet states.

CO^+

Dissociative processes for 2000 eV CO^+ ion impact on CO molecules are illustrated in Figure 7. C^+ is observed at $(m/q)^* = 5.15$ as the major ion product, with the abundance of O^+ an order of magnitude smaller than that of C^+.

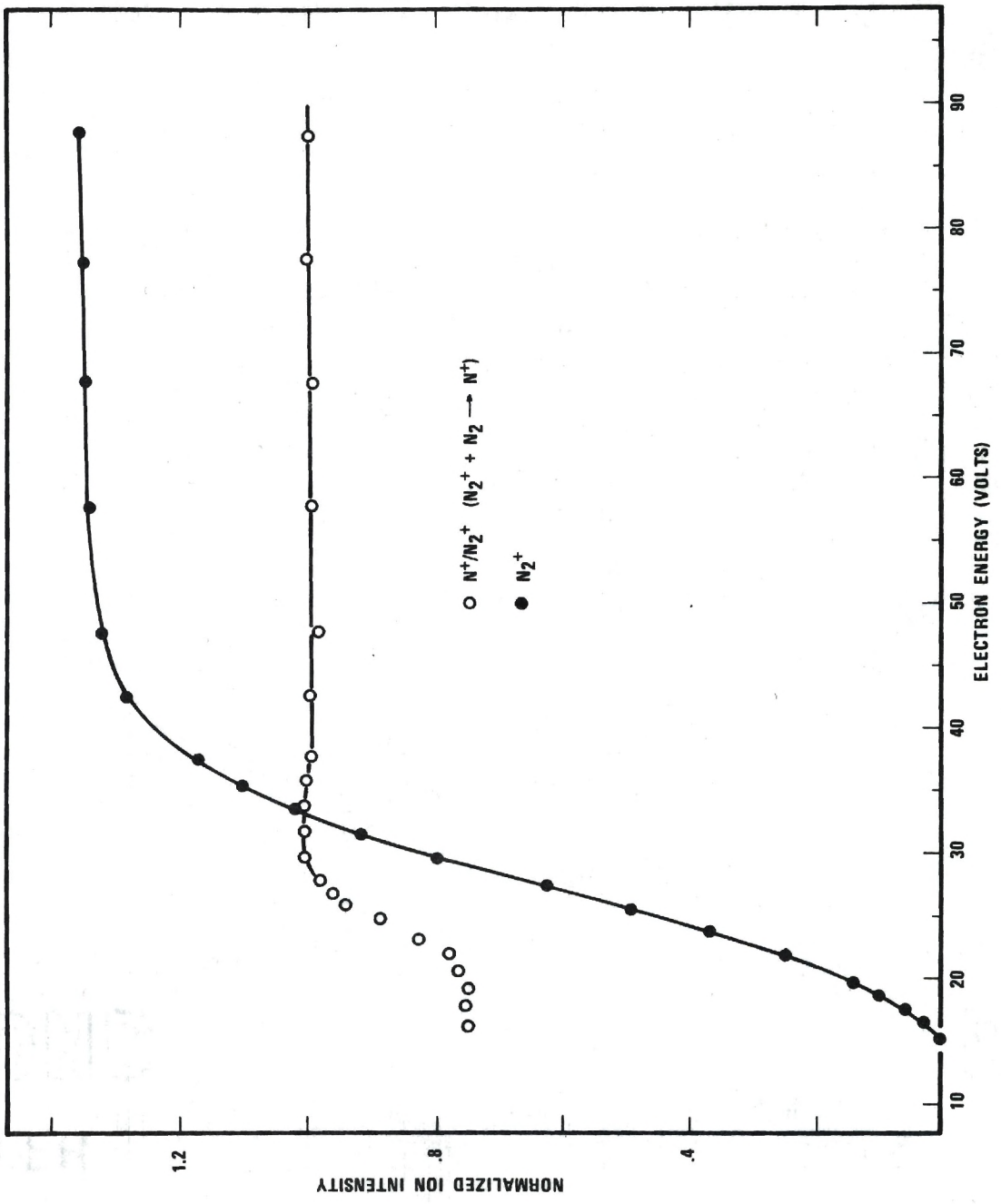

Figure 6. o - Ratio of N^+/N_2^+ Ion Intensity vs. Energy of Electrons Used to Produce the Primary Reactant Ion Beam. (The Solid Points Give the N_2^+ Primary Ionization Efficiency Curve Used to Calibrate the Electron Energy Scale.)

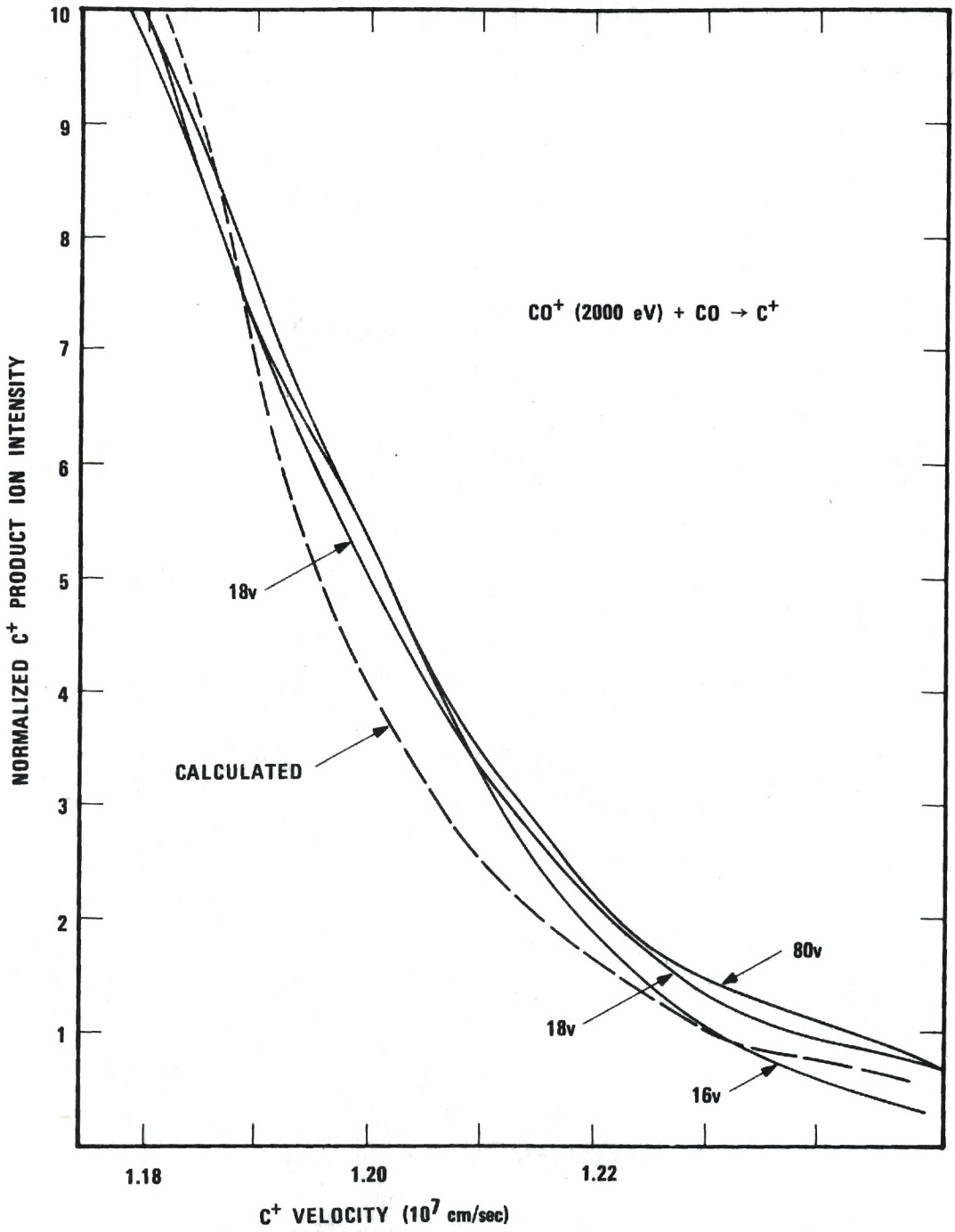

Figure 7. Experimental—— and Calculated---C^+ Product Ion Intensities as a Function of C^+ Velocity in the Laboratory System. (The Experimental Curves are Presented for Reactant CO^+ Ions Formed Via 16, 18, and 80 Volt Electron Impact Ionization of CO.)

The normalized C^+ ion intensity in this figure is given as a function of velocity for various ionizing electron energies. Approximately 25 data points have been taken throughout the velocity range for each of the experimental curves given in Figure 7, but the individual data points are not presented since the precision of each point approximates the thickness of the solid lines. As the energy of the ionizing electrons is increased from 16 to 80 v, the measured distributions are displaced to higher velocities indicating the presence of excited CO^+ levels in the reactant ion beam. Excited CO^+ states are well characterized and photoionization data (52) have been used to calculate the relative electronic transition moments $R_{ij}^{e}(R,\underline{r})$ from which the relative populations of the CO^+ $X^2\Sigma$, $A^2\Pi$, and $B^2\Sigma$ states are found to be 0.35, 0.58, and 0.07 respectively. Our reactant ion beam contains no component from the A or B states since spontaneous radiative B→X and B→A transitions occur (44, 53) 4.5×10^{-8} and 10^{-7} seconds after ion formation, and spontaneous radiative A→X transitions are reported (36) to occur with a 2.6×10^{-6} second lifetime. Thus, the majority of the CO^+ ions will be in the $X^2\Sigma$ state prior to reaction in the collision chamber. The vibrational distributions of the ions initially formed in the X, A, and B electronic states are calculated using equation 11 with the vibrational wavefunctions (34,35) for the CO and CO^+ states, and the CO^+ $X^2\Sigma$ vibrational distributions from the B→X and A→X

spontaneous transitions are estimated from the Franck-Condon factors (34,35,54) tabulated in the literature. From the resultant X state vibrational populations and the CO^+ $X^2\Sigma$ anharmonic oscillator wavefunctions, the number density of CO^+ $X^2\Sigma$ ions are then calculated as a function of R. These results are presented in Figure 8 as the dashed line through the lower part of the ground state potential energy curve which has been constructed from the data compilation of Krupenie (55). If it is assumed that the mechanism of CO^+ dissociation by 2000 eV collisions is similar to that invoked in the case of N_2^+ dissociations, then the shape of the repulsive CO^+ potential energy curve is the only additional information needed to predict the velocity distribution of the C^+ product ions. Alternatively, if the repulsive curve is not well characterized, then the measured velocity distributions can be used to establish its shape. We have used this latter approach to construct the CO^+ repulsive curve given in Figure 8, the shape and position of which is similar to the repulsive portion of the D state of the isoelectronic N_2^+ given in Figure 5. The C^+ velocity distribution obtained using this curve is given as the dashed line in Figure 7. The slight shifting of the measured velocity distributions with increasing ionizing electron energy is consistent with the formation of vibrationally excited CO^+ $X^2\Sigma$ reactant ions resulting from radiative transitions of the A and B states. Evidence for

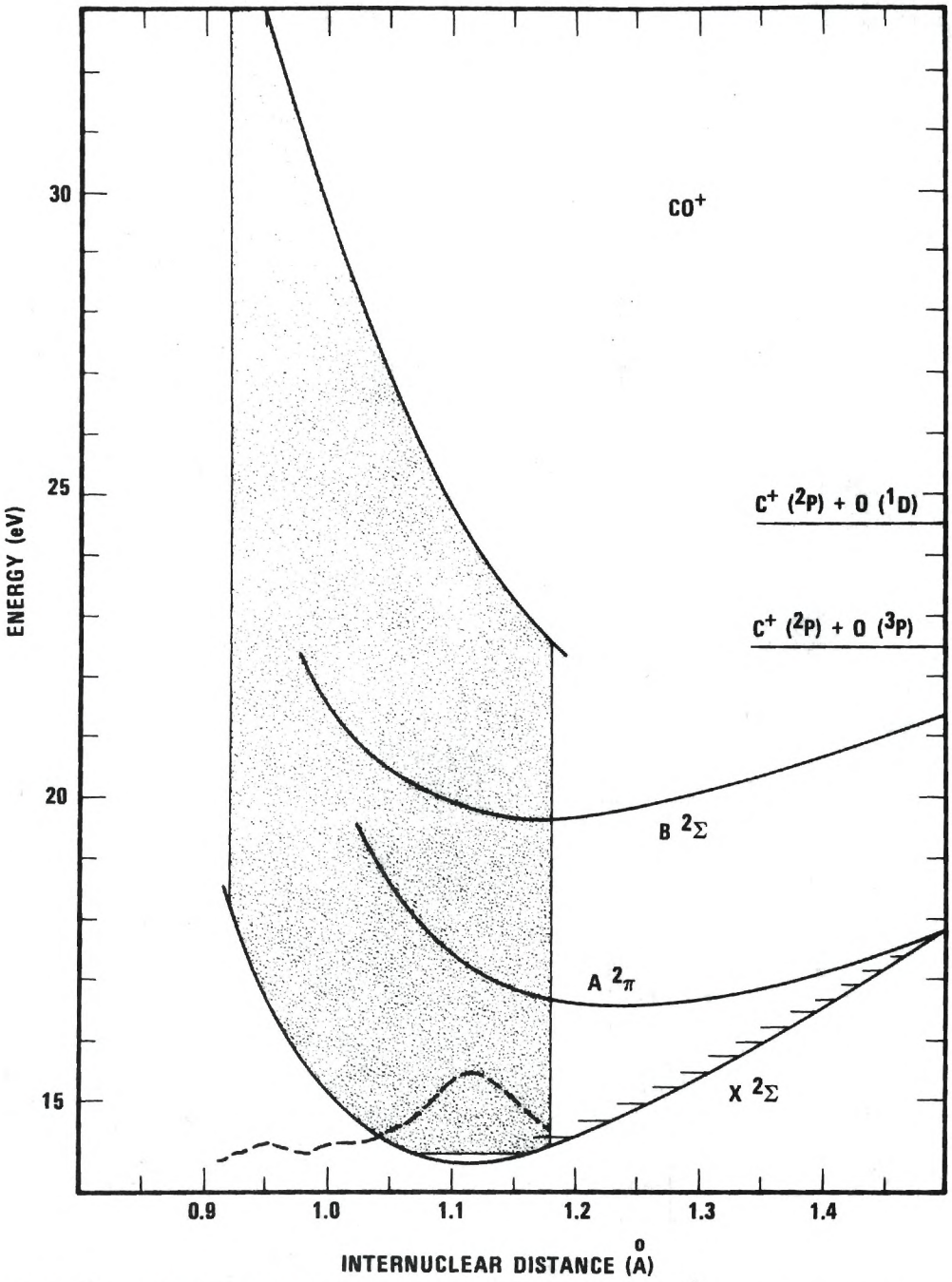

Figure 8. Potential Energy Curves of CO^+. (See Reference 55. The Shaded Region Indicates the Values of Internuclear Distance Used in the Calculation of C^+ Velocity Distributions Given in Figure 7. D(R) is Given as the Dashed Curve. The Repulsive Curve is that Predicted on the Basis of the Measured C^+ Velocity Distributions.)

long-lived electronically excited states is presented in Figure 9 where the C^+(product)/CO^+(reactant) ion intensity ratio, proportional to reaction cross section, exhibits a threshold for a 10 percent increase at 20 eV. This energetic onset is approximately the same as that observed by Cermak and Herman (49) in low kinetic energy CO^+ ion-molecule reactions. They suggest the presence of a long-lived quartet state in the reactant CO^+ ion beam which is consistent with these observations.

O_2^+

Dissociative reactions by $O_2^+ + O_2$ collisions produce O^+ ions at an apparent mass of 8.0. The measured O^+ velocity distributions are presented in Figure 10 for various ionizing electron energies. In contrast to the CO^+ reactions, the velocity distributions of the product O^+ ions from $O_2^+ + O_2$ interactions are shifted to lower velocities as the energy of the ionizing electrons increases. The population of excited O_2^+ states from electron impact ionization has been estimated from photoionization data by Vance (39), who finds that the relative weights for the states are: 0.24 - $X^2\Pi_g$, 0.07 - $a^4\Pi_u$, 0.29 - $A^2\Pi_u$, 0.26 - $b^4\Sigma_g$, and 0.14 - $^2\Sigma_g$. These populations agree with those estimated previously (34), with relative transition moments obtained from photoelectron spectroscopy (52), and with recent calculations (56) using a modified Born approxi-

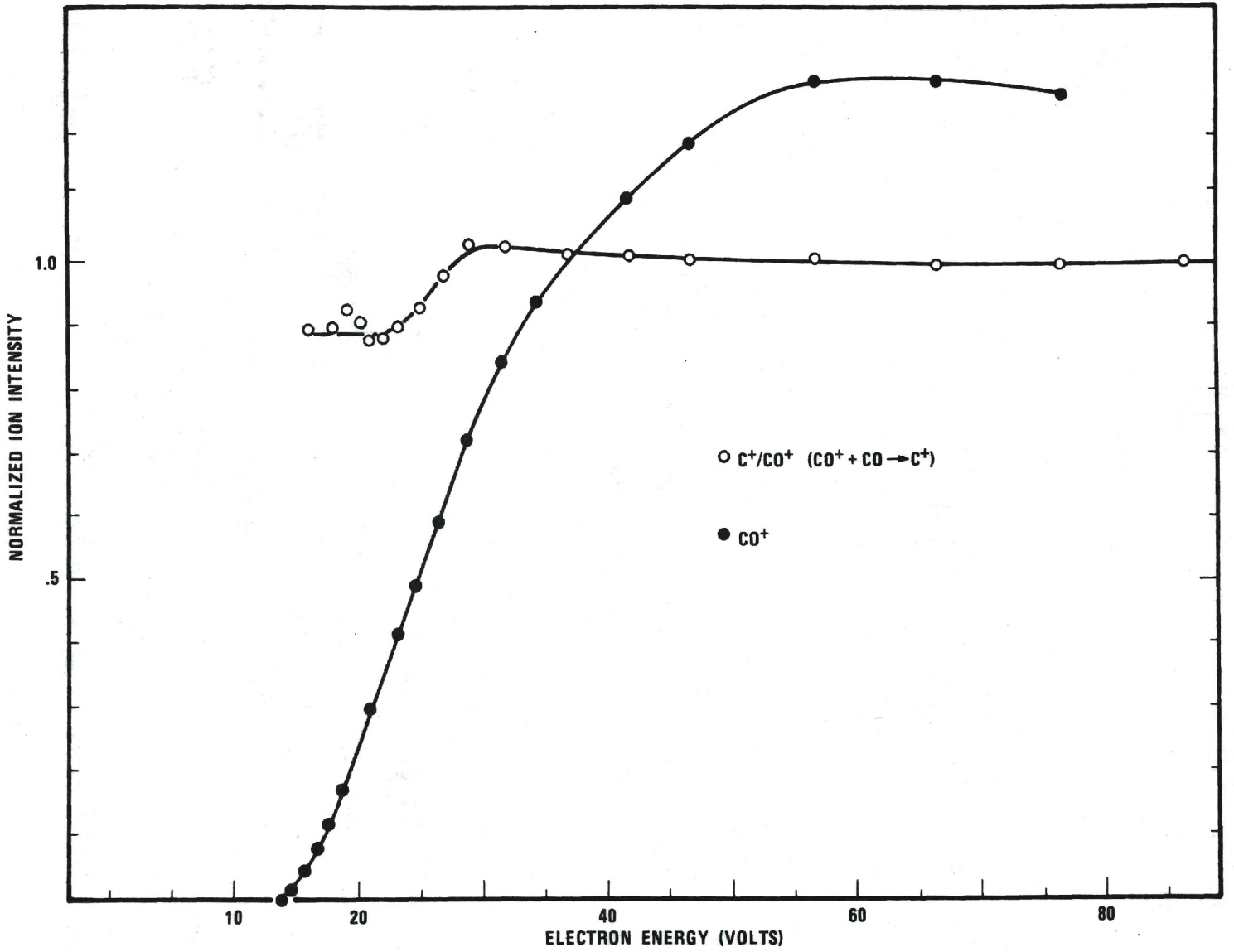

Figure 9. o is the Ratio of C^+/CO^+ Ion Intensity as a Function of Ionizing Electron Energy. (The Solid Points Give the CO^+ Primary Ionization Efficiency Curve.)

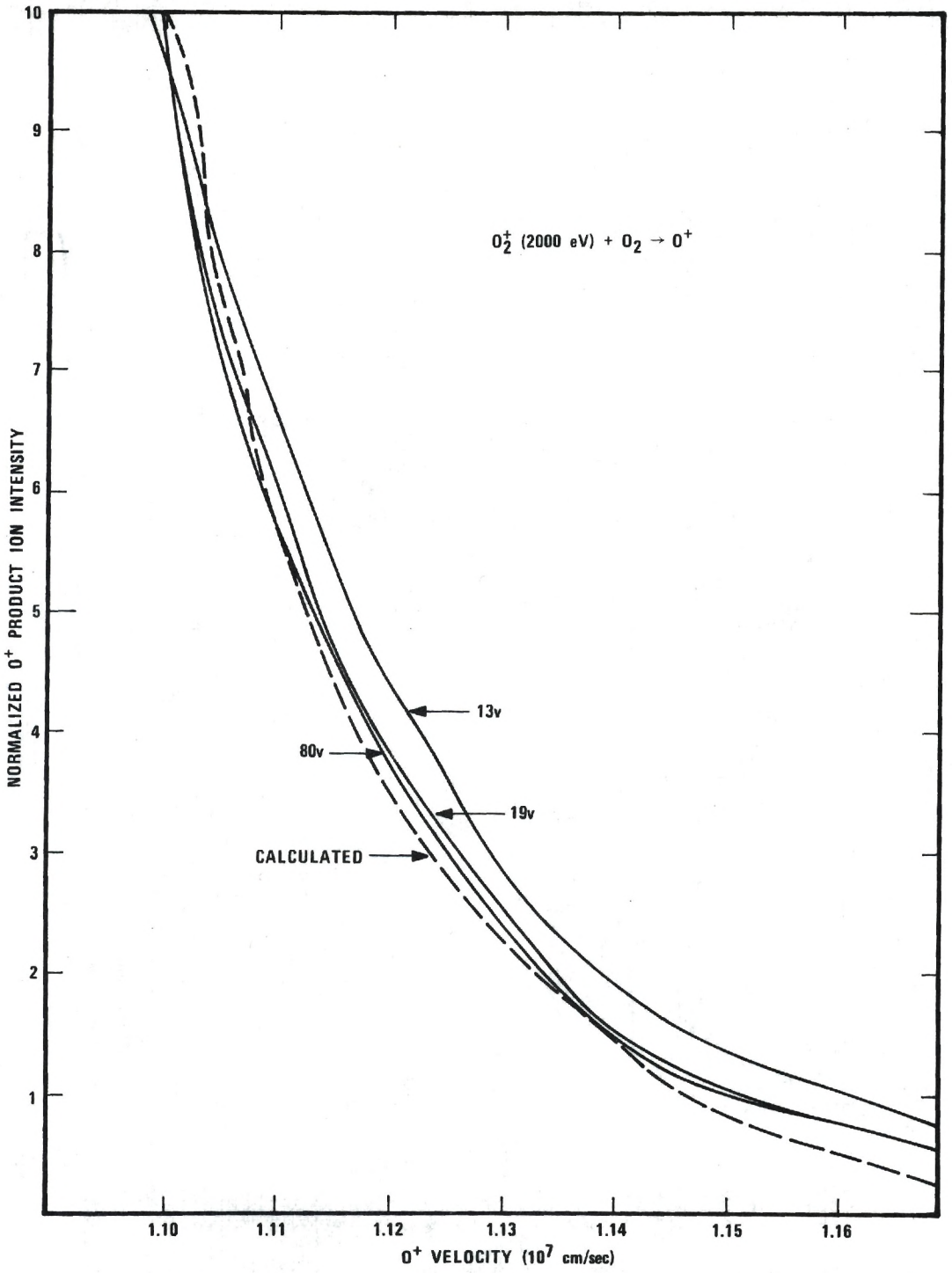

Figure 10. Experimental—— and Calculated- - - O^+ Product Ion Intensities as a Function of O^+ Velocity in the Laboratory System. (The Experimental Curves are Presented for Reactant Ions Produced in 13, 19, and 80 Volt Electron Impact Ionization of O_2.)

mation. Radiative transitions have been observed (57) to occur between the A→X and b→a levels within 1×10^{-6} second. The lifetime of the Σ state before undergoing the $^2\Sigma_g \rightarrow A^2\Pi_u$ transition is estimated (39) to be the same order of magnitude (10^{-6} second). The transitions between the $a^4\Pi_u$ and $X^2\Pi_g$ states are spin forbidden and will not occur in the time required for O_2^+ reactant ions to reach the collision region in the apparatus. Thus, from the above transition moments and radiative decay, 33 percent of the ion beam is estimated to be in the $a^4\Pi_u$ state prior to reaction. This rather high fraction of O_2^+ ions in electronically excited states agrees with the results of Turner, Rutherford, and Compton (61), who estimate from ion beam attenuation measurements that 30-33 percent of the O_2^+ ions are in this long-lived excited quartet state when the ion beam is produced by 50 to 100 eV electron impact ionization. Product O^+ ion velocity distributions are calculated by assuming that reactant ions dissociate via collision induced $X^2\Pi_g \rightarrow A^2\Pi_u$(repulsive section) and $^4\Pi_u \rightarrow {}^4\Sigma_u$ electronic transitions. The regions for these dissociative transitions are shaded in Figure 11. The potential energy curves in this figure have been taken from the compilation of Gilmore (45), except for the $^4\Sigma_g$ state which has been shown to have a slightly deeper attractive potential. The vibrational distributions of the various electronic states produced by the initial electron impact ionization are estimated from

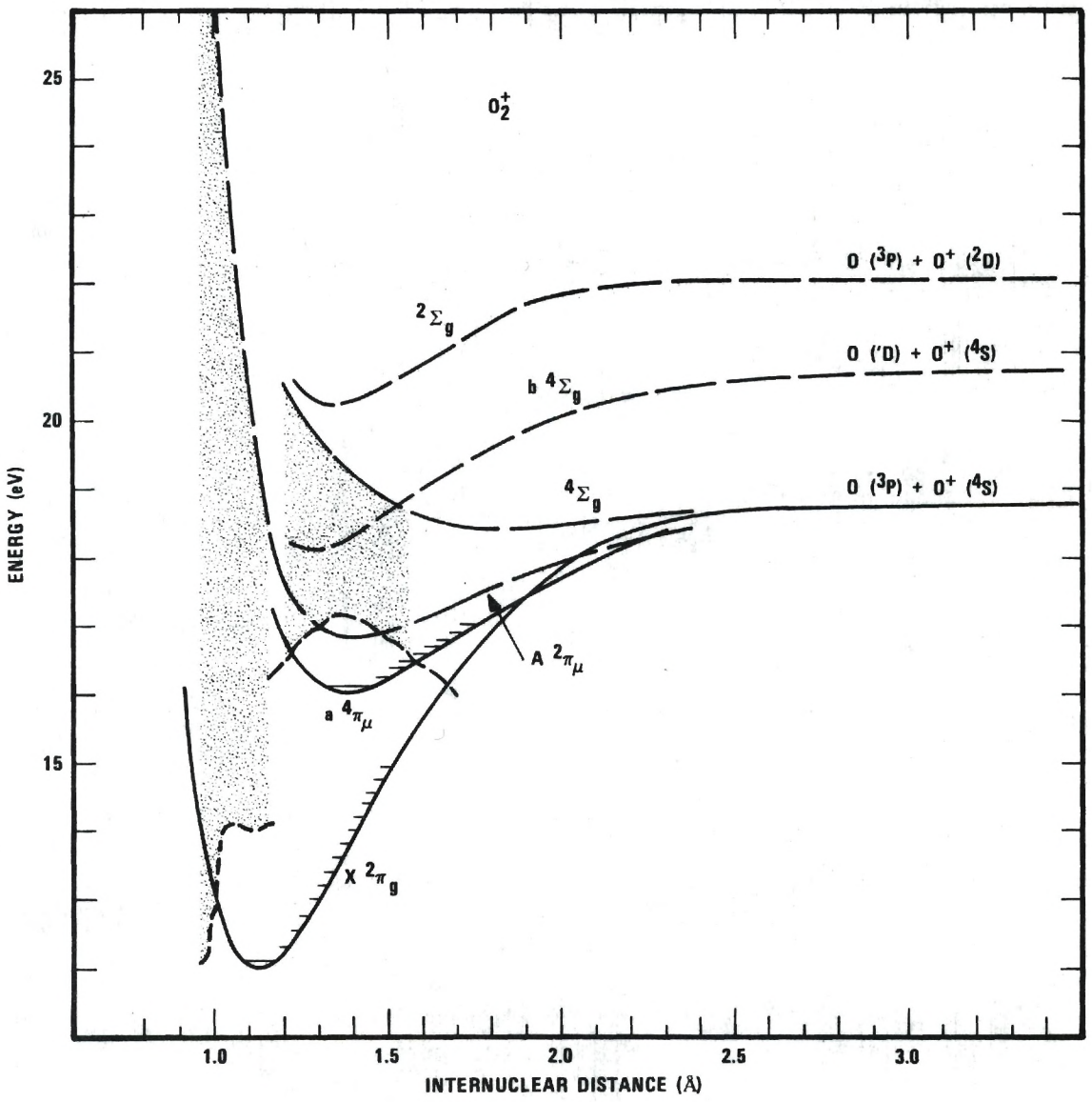

Figure 11. O_2^+ Potential Energy Curves. (The Shaded Regions Indicate the Transitions Taken for the Calculation of the O^+ Velocity Distributions Given in Figure 10.)

the respective overlap integrals (34,35) and agree with experimental data (58,59) obtained from photoelectron spectroscopy. The vibrational distributions resulting from the spontaneous A→X and b→a radiative transitions in the ion beam are estimated from the respective (34,60) overlap integrals tabulated in the literature. These vibrational distributions and the respective anharmonic oscillator wavefunctions are then used to calculate the statistical distributions D(R) of ions in the $X^2\Pi_g$ and $a^4\Pi_u$ states, which are displayed as the dashed curves in Figure 11. The O^+ velocity distributions calculated using this D(R) are given in Figure 10, and reasonably good agreement is found between the calculated and experimental curves. The product O^+ distribution at 13 v appears at higher velocities than at 80 v since the former is entirely produced by transitions from the O_2^+ $X^2\Pi_g$ state to a steeply rising, repulsive, upper potential energy curve. This is schematically shown by the Franck-Condon regions in Figure 11. A closer examination of the low velocity O^+ product ions is made in Figure 12, where the ratio O^+/O_2^+ is plotted as a function of the ionizing electron energy. The O^+ intensity is taken near V_o, so this ratio characterizes reactions producing O^+ ions with very little recoil velocity u in the center of mass system. The O^+/O_2^+ ratio is expected to increase rapidly with increasing ionizing electron energy if the conjecture concerning low O^+ ion product velocities from dissociation

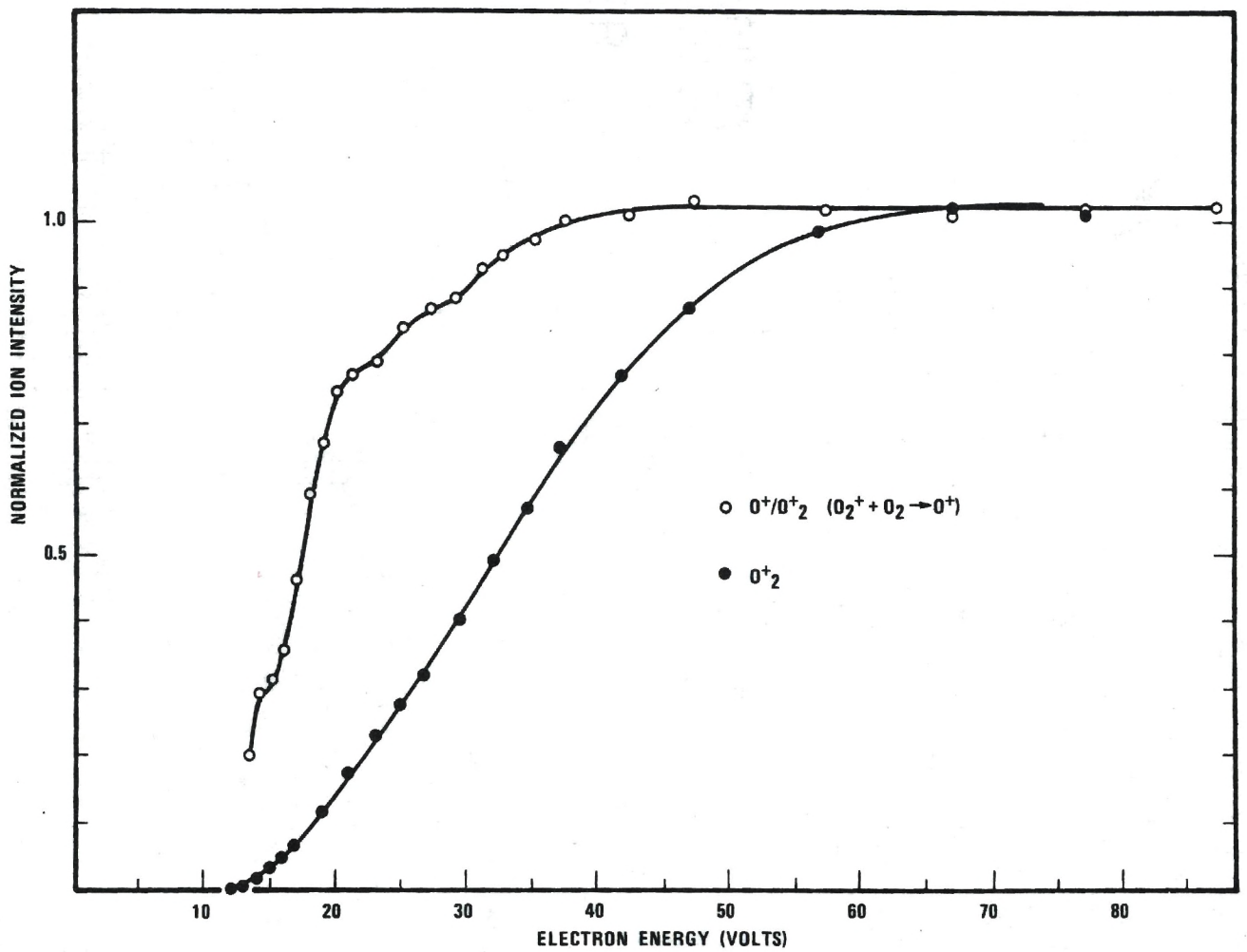

Figure 12. Ratio of O^+/O_2^+ Ion Intensity (o) as a Function of the Electron Energy Used to Produce the O_2^+ Primary Ions. (The Solid Points Give the O_2^+ Primary Ionization Efficiency Curve Used to Calibrate the Electron Energy Scale.)

of the $^4\Pi_u$ state is correct. Indeed, the experimental curve in Figure 12 shows an upward break at 16 eV, the threshold for the $a^4\Pi_u$ state, and an increase through the energetic onset of the $b^4\Sigma_g$ state which spontaneously decays into the $a^4\Pi_u$ state. The breaks in this curve above 20 eV are in approximate accord with similar observations of McGowan and Kerwin (62) who suggest that they are due to reactions of long-lived excited states that have not been observed spectroscopically. The agreement between the calculated and measured momentum distribution curves in Figure 10 would indicate that although these long-lived excited states above 20 eV are a minor constituent of the ion beam, they have a relatively large cross section for dissociative reactions producing low velocity O^+.

NO^+

The 2000 eV dissociative reactions of NO^+ yield approximately the same number of N^+ and O^+ products, and their velocity distributions are presented in Figures 13 and 14. Both the N^+ and O^+ distributions are similar functions of electron energy, which shows that both ions are produced from the same reactant ion states. These velocity distributions are sensitive functions of ionizing electron energy, suggesting the participation of excited reactant ions in the reaction mechanisms. The potential energy curves for NO^+ excited states given as the insert in Figure 14 are those presented by Collin and Natalis (63,64). The relative prob-

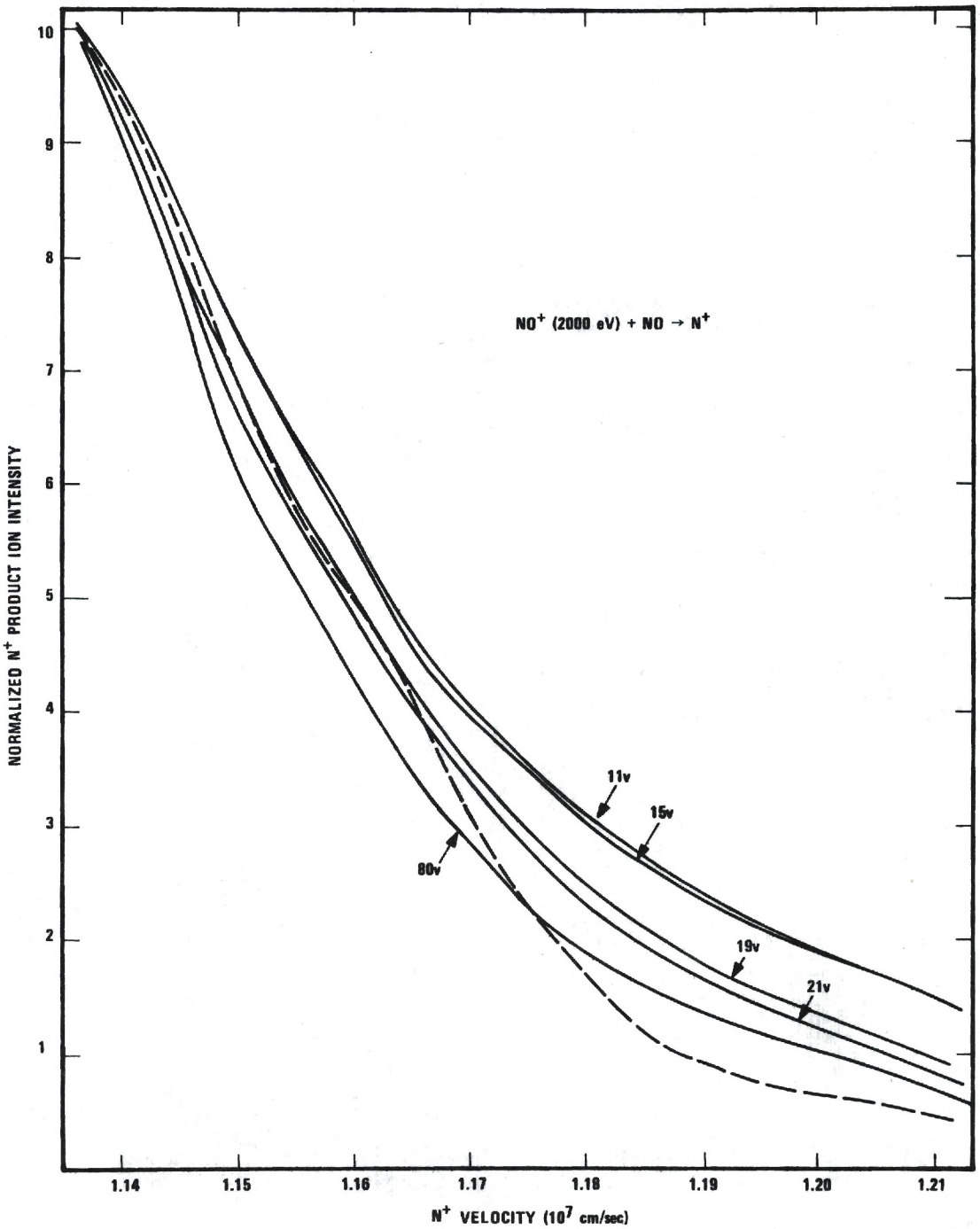

Figure 13. Experimental ——— and Calculated ----- N^+ Product Ion Intensities as a Function of N^+ Velocity in the Laboratory System. (The Experimental Curves are Presented for Reactant Ions Produced in 11, 15, 19, 21, and 80 v Electron Impact Ionization of NO.)

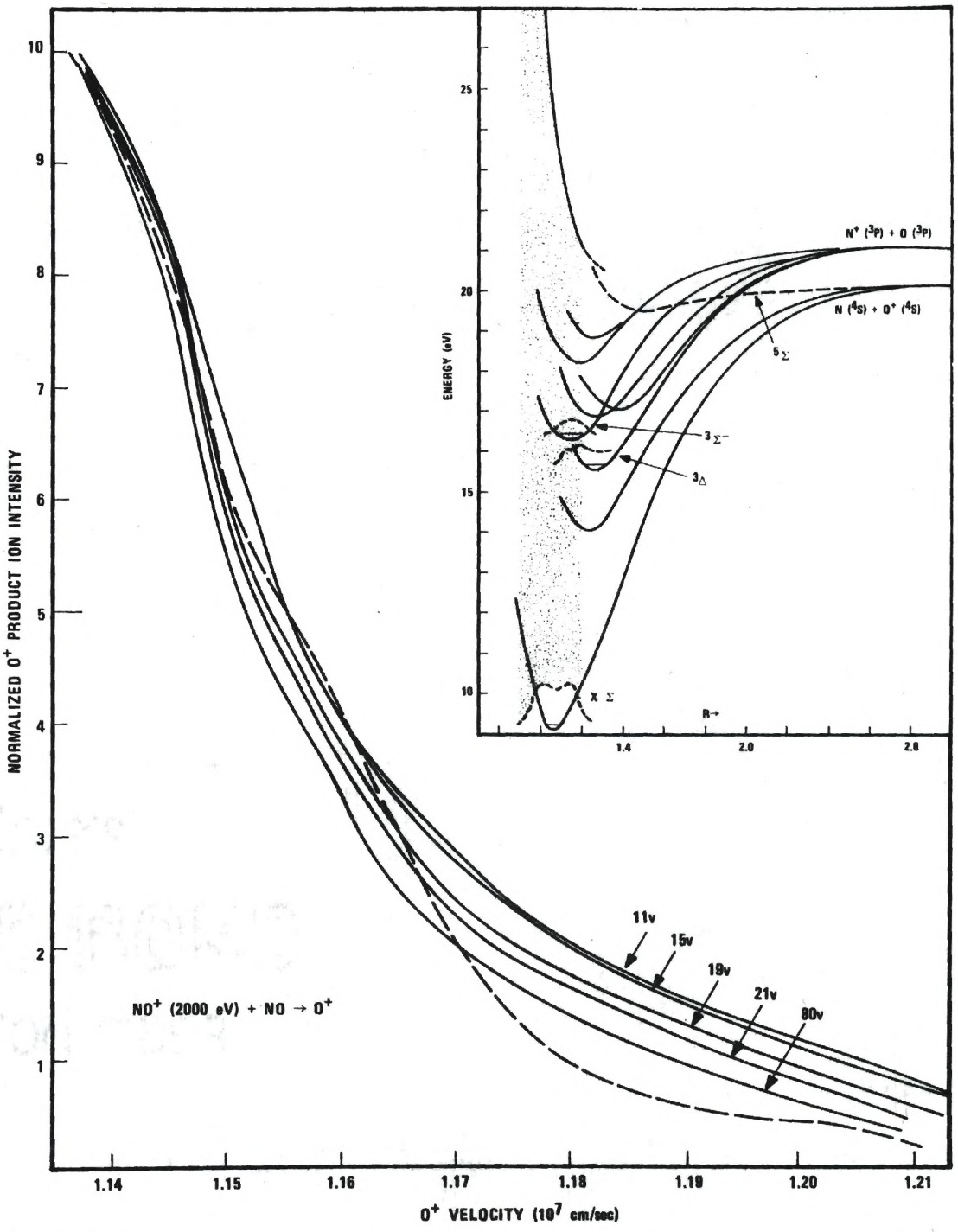

Figure 14. Experimental ——— and Calculated ----- O^+ Product Ion Intensities as a Function of O^+ Velocity in the Laboratory System. (The Experimental Curves are Presented for Reactant Ions Produced in 11, 15, 19, 21, and 80 v Electron Impact Ionization of NO. The Insert Gives the Potential Energy Curves for NO^+.)

abilities for populating these different electronically excited NO^+ states have been estimated (39) to be 0.45 - $X^1\Sigma$, 0.0 - $^3\Sigma$, 0.43 - $^3\Delta$ and $^3\Sigma$, and 0.12 - $A^1\Pi$. Although there is evidence for the existence of the $a^3\Sigma$ state, the probability for producing this state (58,63-65) by the ionization of NO molecules is very small. The spontaneously radiative $A^1\Pi \rightarrow X^1\Sigma$ transition occurs in $6x10^{-6}$ second but the triplet levels are spin forbidden to decay into the ground state within $6x10^{-6}$ second, the time interval between formation of an ion in the source region and its reaction in the collision chamber. It is assumed that about 22 percent of the reactant ion beam is in the $^3\Delta$ state and about 22 percent is in the $^3\Pi$ state. These estimates are only approximate since the population of only four states by electron impact ionization has been assumed. The $^1\Delta$ state is produced with a reasonably large cross section (64); however, the $^1\Delta - A^1\Pi$ transition enables an $A^1\Pi \rightarrow X^1\Sigma$ cascade to take place, which populates the ground state. Therefore, the inclusion of the $^1\Delta$ state in the consideration of the relative transition probabilities will not change the estimate that 43 percent of the reacting ions are in electronically excited triplet states. Mathis, Turner, and Rutherford (66) have concluded from ion beam attenuation measurements that 42 percent of an NO^+ ion beam formed by 50 eV electron impact ionization is in long-lived excited states.

Collision induced transitions producing N^+ ions are assumed to take place to repulsive portions of the potential energy curves (45) from both ground and triplet states of the reactant ions as indicated in Figure 14. The N^+ velocity distributions are calculated from equation 9 and are compared with the experimental data as shown in Figure 13. The measured O^+ velocity distributions from NO^+ dissociations are presented in Figure 14. Reactions that produce O^+ are assumed to be a consequence of collision induced electronic transitions to the $^5\Sigma$ state from the ground $X^1\Sigma$ and long-lived $^3\Delta$ and $^3\Sigma$ states in calculating the dashed curve. The Franck-Condon region for this reaction extends to approximately 1.3 Å where the $^5\Sigma$ curve crosses the O^+ dissociation asymptote at 20.1 eV. Further evidence that both the ground $X^1\Sigma$ and excited $^3\Delta$ and $^3\Sigma$ states participate in the production of O^+ is given in Figure 15, where the O^+(product)/NO^+(reactant) ion intensity ratio is presented as a function of electron energy. As seen in this figure, O^+ ions are initially formed at the ionization potential of nitric oxide, indicating dissociative transitions from the ground $X^1\Sigma$ state. As the ionizing electron energy increases, the O^+/NO^+ curve exhibits a break near the energetic threshold of the NO^+ $^3\Delta$ and $^3\Sigma$ states, which is to be expected if reactions producing O^+ proceed via these long-lived states. The fact that the cross section for N^+ formation as a function of electron energy has the

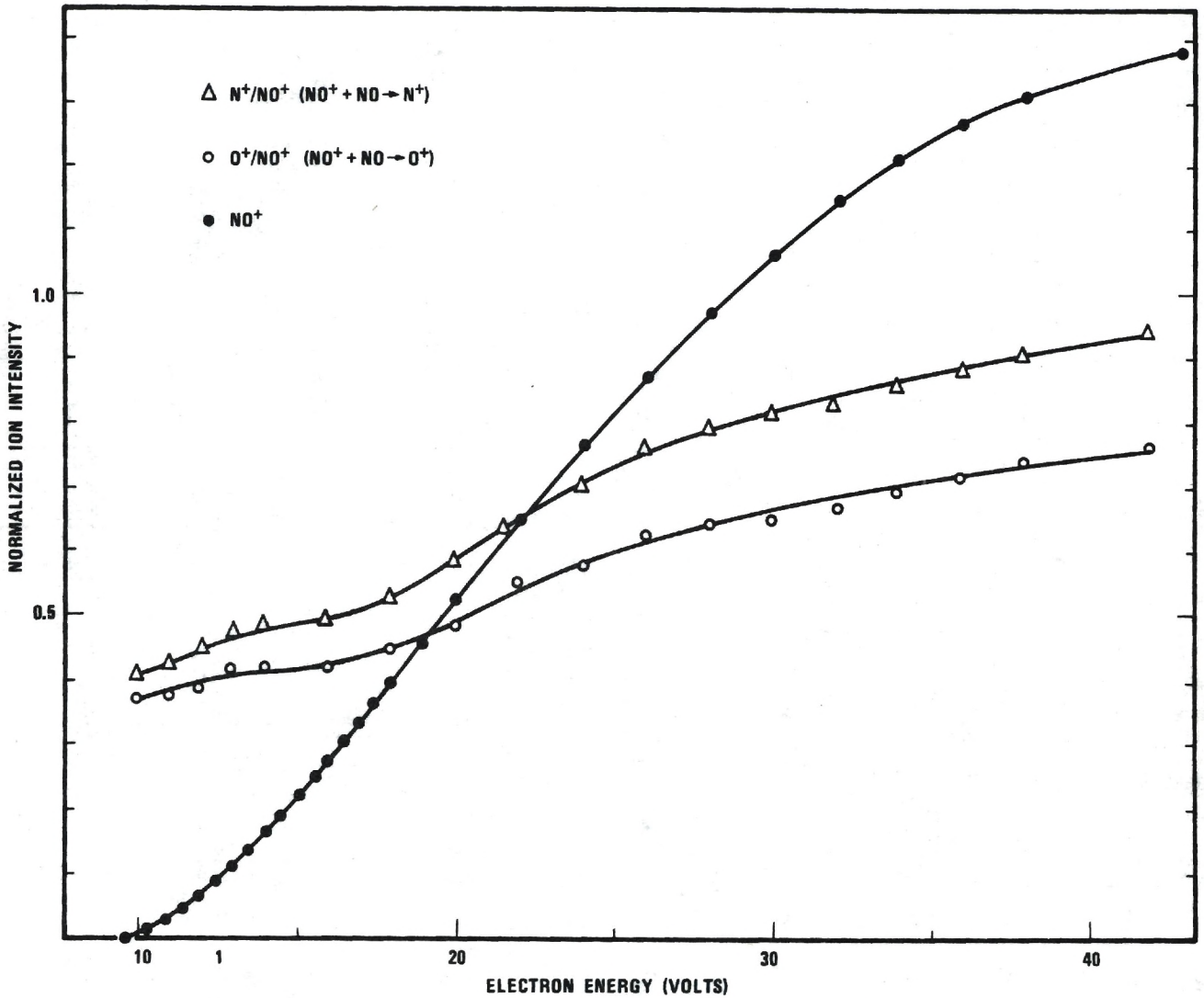

Figure 15. Ratio of N^+/NO^+ (Δ) and Ratio of O^+/NO^+ (o) as a Function of Electron Energy Used to Produce the NO^+ Primary Ions. (The Solid Points Give the NO^+ Primary Ionization Efficiency Curve.)

same shape as the O^+ curve indicates similar mechanisms in which both product ions are produced from the $X^1\Sigma$, $^3\Delta$, and $^3\Sigma$ NO^+ states.

$NO^+(NO_2)$

Diatomic reactant ions may also be produced by electron impact ionization of triatomic species. It is of interest to compare the internal energy of diatomic ions produced in this manner with that of those produced directly from ionization of diatomic molecules as discussed above. Analogous studies of the dissociation of neutral NO_2 by ultraviolet photons (67,68) and low energy electrons (69) have shown that electronically excited NO molecules are formed from NO_2; however, detecting excited NO^+ ions from NO_2 is somewhat difficult. Collision induced dissociative reactions may be used to probe the internal energy of diatomic ions since such reactions are very sensitive to the internal energy of the reactant ions. Ionization of NO_2 results in the formation of NO^+ ions that dissociate in 2000 eV collisions, with both N^+ and O^+ observed as reaction products. The measured velocity distributions of the product O^+ ions are given in Figure 16 as a function of ionizing electron energy. NO^+ ions formed by 80 v electron impact ionization of both NO and NO_2 result in similar O^+ velocity distributions as seen by comparing Figures 14 and 16. A quantitative fit to the 80 v data in Figure 16 (anal-

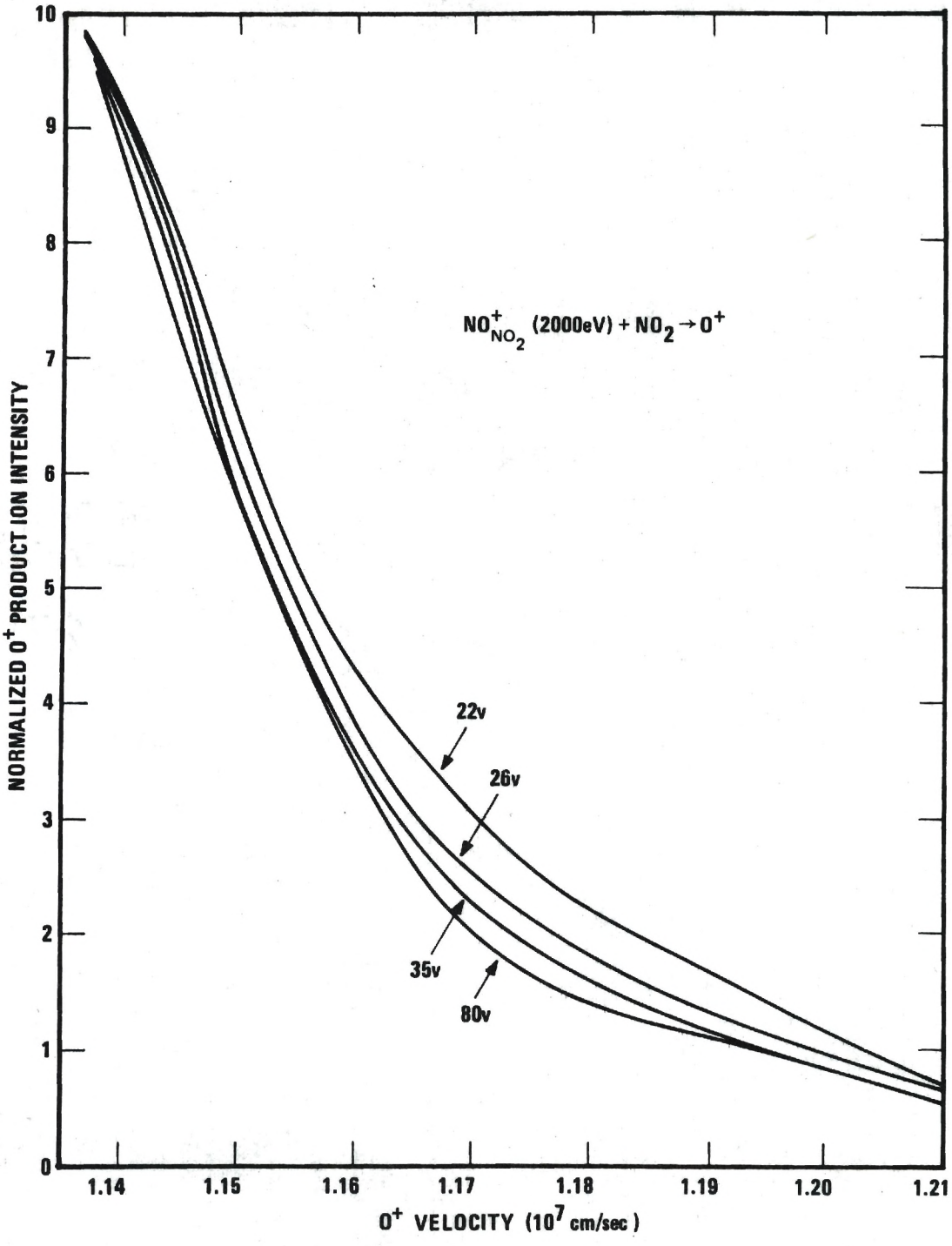

Figure 16. Experimental O^+ Product Ion Intensities from the Collision Induced Dissociation of NO^+ Ions. (The Primary NO^+ is Formed in 22, 26, 35, and 80 v Electron Impact Ionization of NO_2.)

ogous to the dashed line in Figure 14) may be obtained by assuming that 50 percent of the reactant NO^+ ions are in the ground $X^1\Sigma$ state and the remainder equally populate the $^3\Delta$ and $^3\Sigma$ states, with vibrational distributions approximating those of NO^+ ions formed by ionization of NO. The shape of the N^+ velocity distributions observed to result from the dissociation of NO^+ from NO_2 is identical to that of the curves in Figure 13. Further indication that long-lived, excited states are present in the reactant NO^+ ions from NO_2 is given in Figure 17, where the N^+/NO^+ ratios exhibit a dependence on electron energy similar to that in Figure 15.

All reactions discussed in this chapter require transfer of reactant ion kinetic energy into electronic excitation during collision. The apparent mass $(m/q)^*$ of the product ions is observed to be displaced toward a slightly lower value than that predicted by equation 3 and this small shift in apparent mass $(m/q)^*$ can be related, using standard techniques (21), to a kinetic energy loss in the collision. Table 1 presents this data for the various reactions, corrected for the initial kinetic energy distributions of the reactant ions, i.e. Maxwellian for those produced by ionization of diatomic molecules, but finite for diatomic ions produced by ionization of triatomic molecules (27,46). The precision of the energy loss data in Table 1 is ±1.5 eV. Reactions 4 and 6 were further studied by substituting ar-

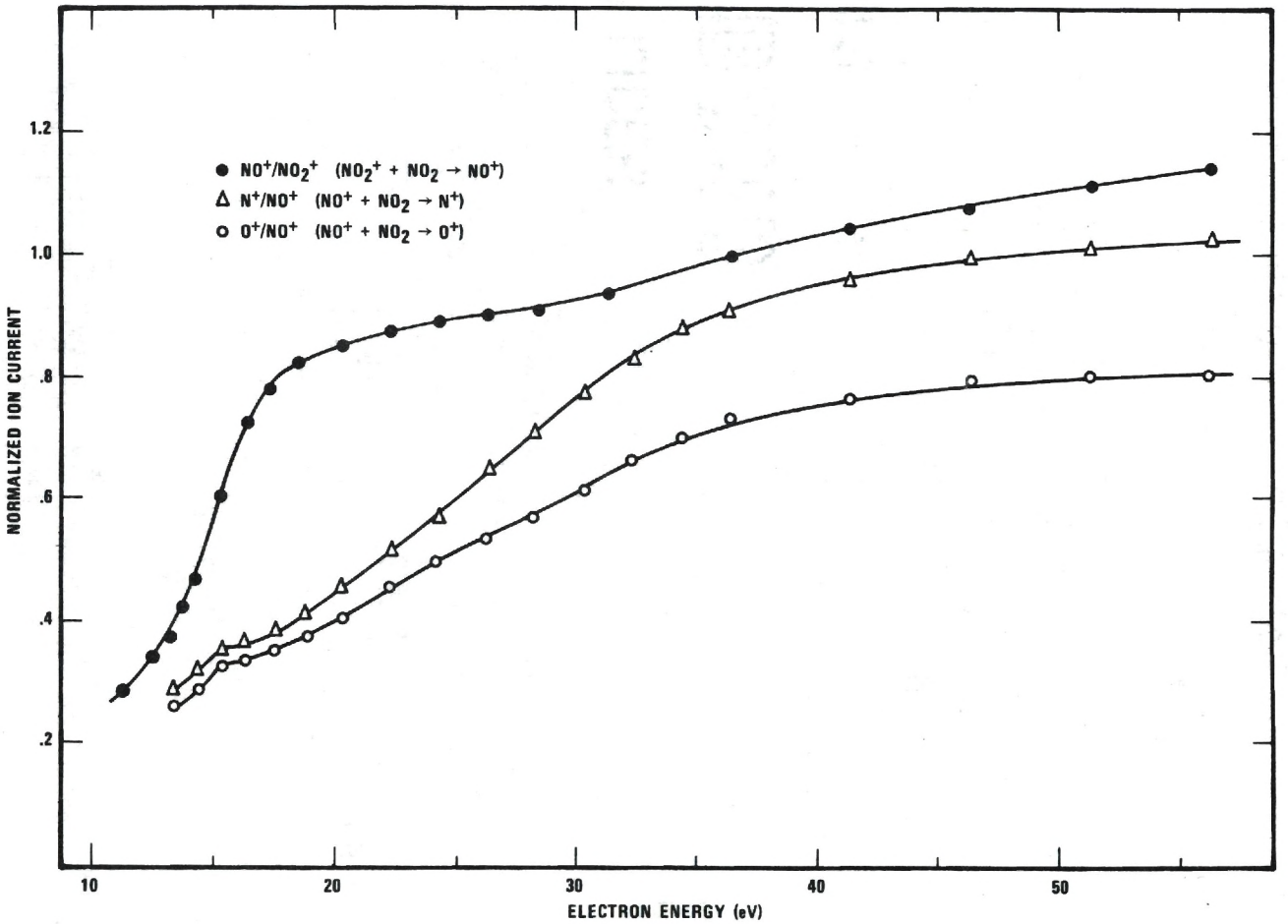

Figure 17. Ratio of N^+/NO^+ (Δ) and Ratio of O^+/NO^+ (o) Ions as a Function of Electron Energy to Produce the Primary NO^+ Beam from the Electron Impact Ionization of NO_2. (The Solid Points give the Relative Cross Section for the Collision Induced Dissociation of 2000 eV NO_2^+ Ions.)

Table 1. Energy Loss in Dissociative Reactions of 2000 eV Diatomic Ions. (Precision of these Values is ±1.5 eV.)

Reaction	Energy Loss (eV)
(1) $N_2^+ + N_2 \rightarrow N^+$	10.3
(2) $CO^+ + CO \rightarrow C^+$	14.8
(3) $O_2^+ O_2 \rightarrow O^+$	8.7
(4) $NO^+ + NO \rightarrow \begin{cases} O^+ \\ N^+ \end{cases}$	8.4 10.9
(5) $CO(CO_2) + CO_2 \rightarrow C^+$	11.0
(6) $NO^+(NO_2) + NO_2 \rightarrow \begin{cases} O^+ \\ N^+ \end{cases}$	7.0 10.0

gon for the neutral target species and no change in energy loss was observed. This suggests that simultaneous internal excitation of target molecules by collision is not dominant, but that the energy required for dissociative electronic transitions of the reactant ions accounts for their loss of kinetic energy. The comparable energy loss for reactions 4 and 6 of Table 1 provides additional evidence that the population distribution of reactant NO^+ among the various long-lived excited electronic states is similar whether the NO^+ is formed by ionization of NO or of NO_2.

$CO^+(CO_2)$

Collision induced dissociation of CO^+ formed by electron impact ionization of CO_2 yields C^+ as the major reaction product. The O^+ product ion intensity is less than 0.1 that of the C^+ product, a fraction similar to that observed for the $CO^+(CO)$ reactions. $C^+(CO_2)$ velocity distributions, presented in Figure 18 for various ionizing electron energies, are distinctly different from those in Figure 7 for the reactions of CO^+ from CO which would indicate that internal energies of CO^+ ions depend on their manner of formation. Normalized C^+ velocity distributions given in Figure 18 decrease as the ionizing electron energy is increased from 22 to 80 v. The CO^+ ions produced at 22 v have a maximum internal energy of 1 eV, since the energetic threshold for CO^+ formation by electron impact ionization

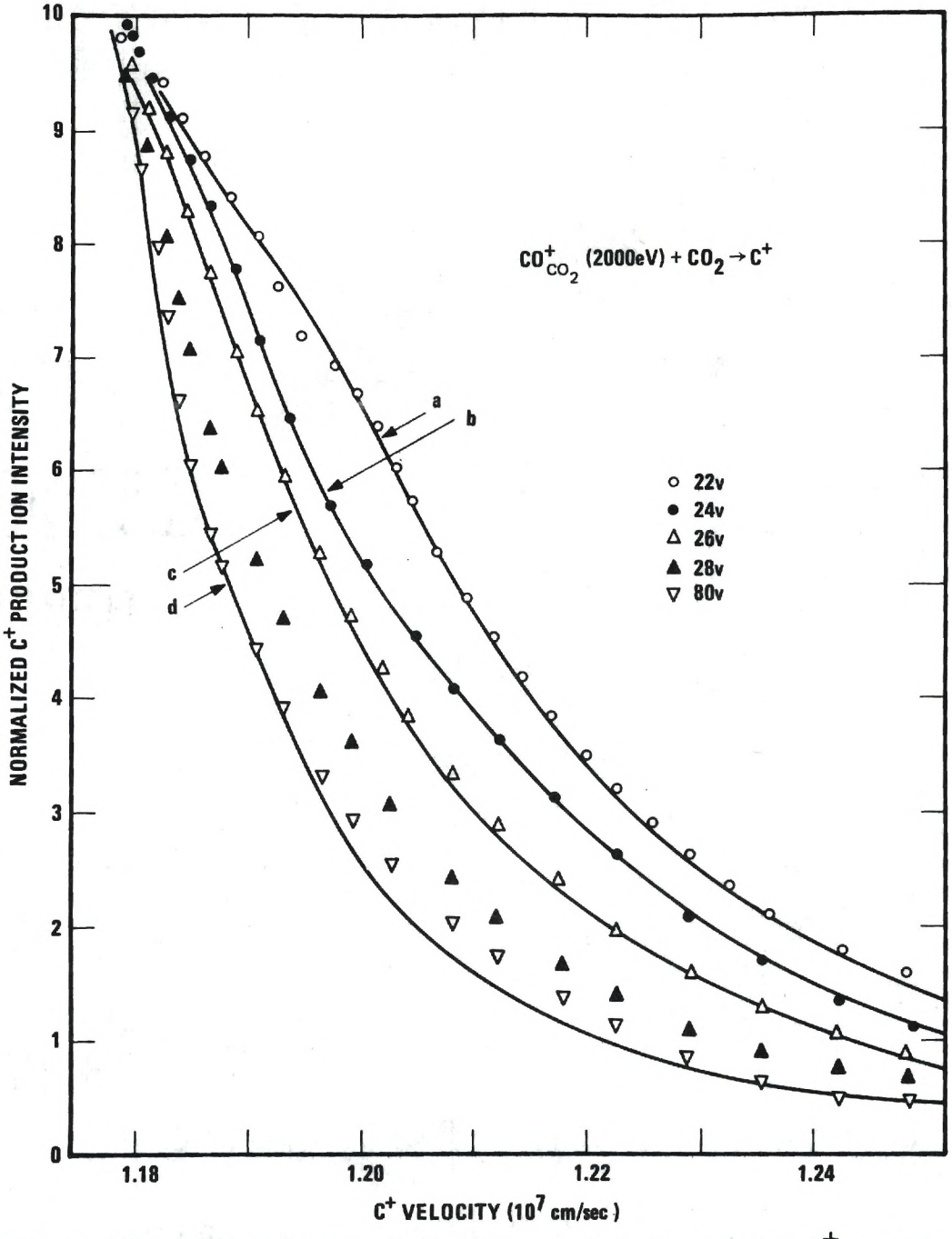

Figure 18. Experimental Points and Calculated C^+ Product Ion Curves as a Function of C^+ Velocity in the Laboratory System. (The CO^+ Primary Ion Beam is Produced in the Electron Impact Ionization of CO_2. The Experimental Points are Given for Different Values of Ionizing Electron Energy and the Curves are Calculated Using CO^+ Vibrational Population Distributions Given in the Text.)

of CO_2 is approximately 21 eV (25,70). As the electron energy is increased, the reactant CO^+ may be formed with more internal energy (71) and/or recoil kinetic energy (70) from the unimolecular fragmentation of CO_2^+ in the ion source. The lowered velocity distributions are ascribed to a change in CO^+ internal energy since these distributions have been corrected for the small initial CO^+ recoil energy. Since electron impact ionization of CO_2 does not produce (72) electronically excited CO^+, vibrational excitation in the reactant CO^+ ions is suggested to explain the shift in the measured C^+ velocity distributions. A quantitative fit to the experimental points in Figure 18 is obtained using equation 9 with D(R) computed from CO^+ anharmonic oscillator wavefunctions and the electron energy dependent weights assigned to the CO^+ vibrational level populations. The curves are calculated by weighting vibrational populations of levels v=0,1,2 respectively: curve a - .58, .32, and .10; curve b - .42, .34, and .24; curve c - .33, .33, and .34. For curve d the population of each of the first 10 vibrational levels is weighted equally. Supplementary evidence that electron impact ionization of CO_2 produces CO^+ in high vibrational levels is presented in Figure 19 where the C^+/CO^+ ratio (with C^+ measured near V_o) shows a fivefold increase with increasing electron energy. According to the model presented above, reactant CO^+ in high vibrational levels would yield a greater proportion of slow product

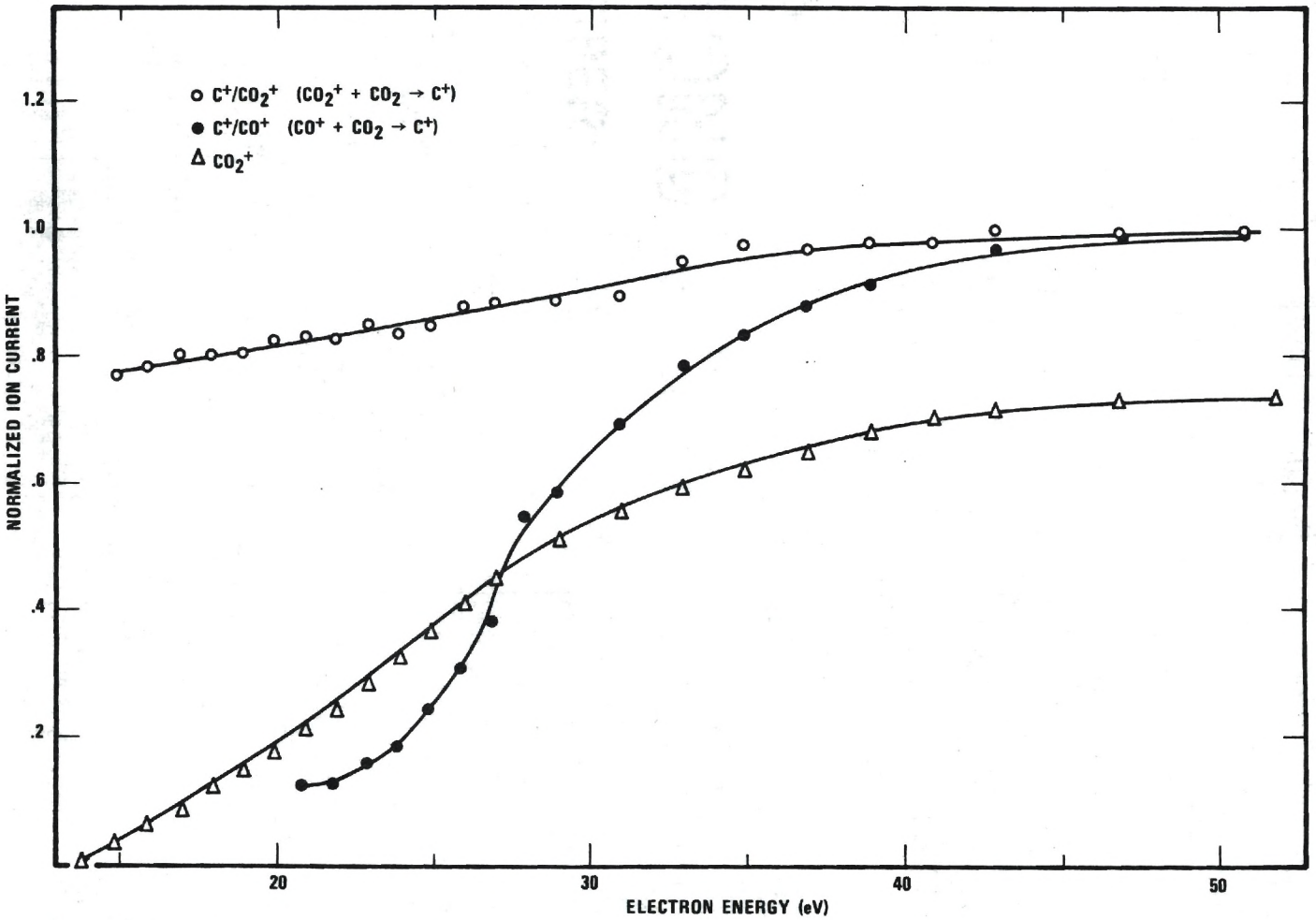

Figure 19. C^+/CO^+ Ratio (●) as a Function of Electron Energy Used to Produce the Primary CO^+ Ion Beam via the Ionization of CO_2 Molecules. (The Ionization Efficiency Curve of CO_2^+ is Given by the Δ Points. The Open Circles Give the Relative Cross Section for the Collision Induced Dissociation of 2000 eV CO_2^+ Ions.)

ions. These excited CO^+ ions are expected to require less incident beam kinetic energy for dissociation and, therefore, exhibit a smaller observed energy loss than corresponding ions in low vibrational levels. Comparison of the energy losses in reactions 5 and 2 of Table 1 further suggests that highly excited CO^+ ions are produced by the electron impact ionization of CO_2.

Conclusions

Collision induced dissociations of 2000 eV N_2^+, O_2^+, CO^+, and NO^+ proceed via Franck-Condon transitions to the repulsive portions of the potential energy curves. Product ion velocity distributions measured with a mass spectrometric apparatus show the effect of internal ionic excitation on the dissociation process.

The velocity distributions of N^+ from N_2^+ collision induced dissociation do not vary significantly as the energy of the ionizing electrons increases from 18 to 80 v, indicating that electronically excited A and B states formed by ionization decay spontaneously to the ground X state before collision. Hence dissociation of N_2^+ in 2000 eV collisions occurs by a vertical transition from the lower vibrational levels of the ground X state to the repulsive portion of the D state.

The C^+ velocity distributions from CO^+ collision induced dissociation are displaced to slightly higher veloci-

ties as the ionization energy is increased from 16 to 80 v, indicating the presence of vibrationally excited CO^+ in the reactant ion beam. Spontaneous decay of A and B states initially formed by ionization populate excited vibrational levels of the CO^+ ground X state, and dissociation proceeds via a vertical transition from this state to the repulsive potential energy curve.

Collision induced dissociation of O_2^+ produces O^+ ions whose velocity distributions shift to lower velocities as the electron ionization energy increases from 13 to 80 v, because the long-lived $a^4\Pi_u$ state of O_2^+ is formed along with the ground $X^2\Pi_g$ state by ionization and O^+ from the dissociation of the excited electronic state emerges with relatively less translational energy than from the ground state.

The N^+ and O^+ velocity distributions from NO^+ collision induced dissociation are similar functions of electron energy, therefore both product ions are produced from the same reactant ion states. The velocity distributions shift to lower velocities as ionization energy is increased from 11 to 80 v, since excited long-lived triplet NO^+ states are formed by ionization at higher energies and participate in the collision process.

Unimolecular decomposition of NO_2^+ produces NO^+ in electronically excited triplet states, while CO^+ is formed from CO_2^+ decomposition with vibrational excitation only.

Kinetic energy loss of diatomic molecule ions undergoing dissociation corresponds to the energy required for dissociative electronic transitions of the reactant ions.

CHAPTER III

LOW ENERGY INELASTIC ENERGY LOSS

Introduction

While at 2000 eV ion-neutral collisions lead to electronic excitation and subsequent molecular dissociation, at lower kinetic energies nondissociative channels of reaction predominate. Thus, at incident energies on the order of 10 eV, a molecule ion may be inelastically scattered by a neutral target while undergoing a kinetic to internal energy transfer. Such scattered molecules will be in higher vibrational-rotational states after collision and their degree of excitation may be elucidated by experimental observation of the kinetic energy of the charged particle before and after it undergoes collision.

Kinematics of Collision

The relationship between collisional kinetic energy loss by inelastic collision and internal energy excitation of the colliding molecule may be derived in a straightforward manner from considerations of momentum and energy conservation and the law of cosines. A schematic representation of in-plane scattering is shown in Figure 20, in which P_o is the momentum of the incident ion, P is the momentum of the scattered ion, F is the momentum of the center of

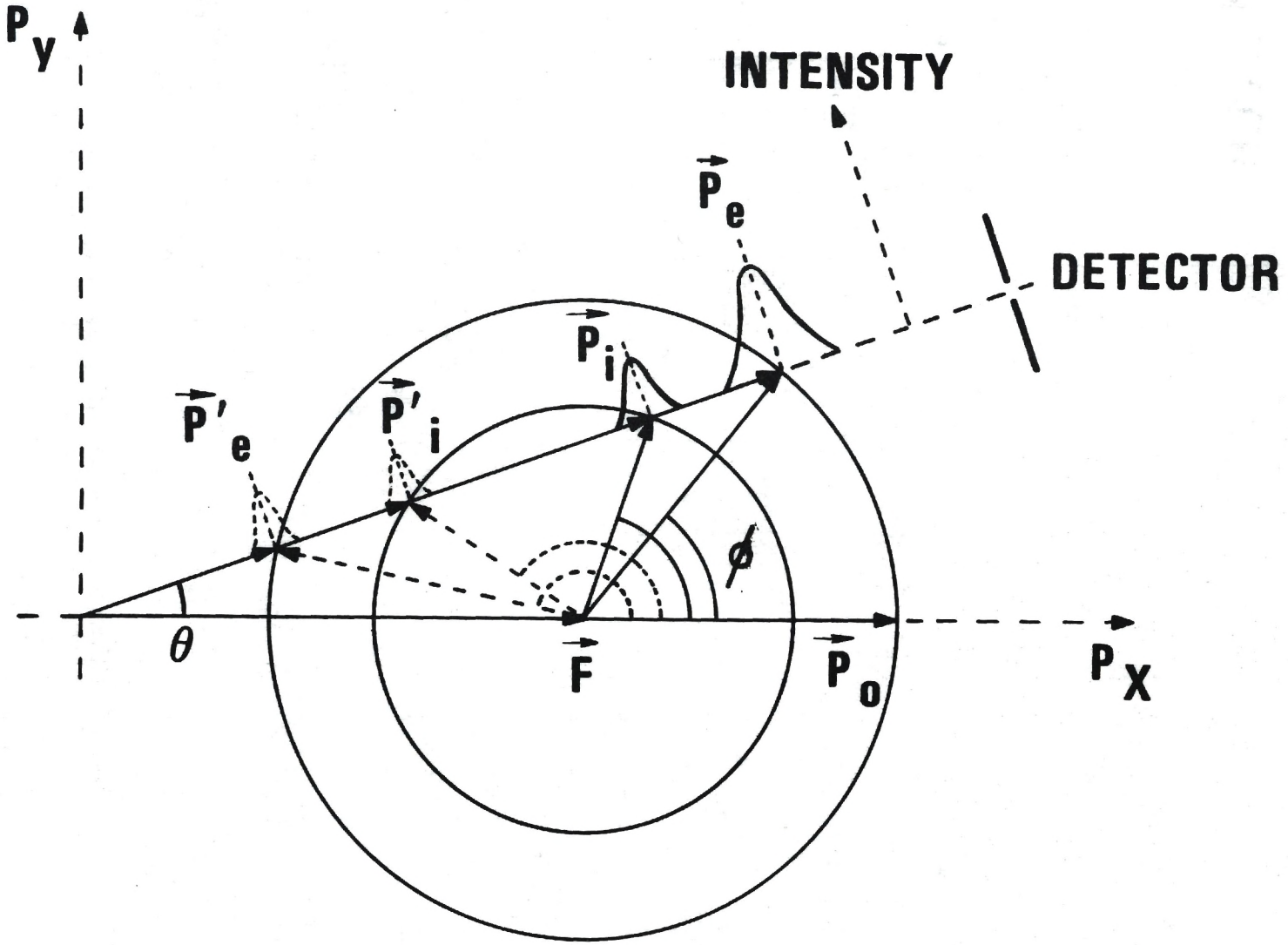

Figure 20. Schematic Momentum Vector Diagram for Elastic and Inelastic Scattering Processes.

mass, R is the momentum of the scattered ion with respect to the center of mass, θ is the laboratory scattering angle, and ϕ is the center of mass scattering angle. Subscripts e and i refer to elastic and inelastic parameters respectively. The larger circle is the locus of terminii of all possible momentum vectors for elastic scattering (translational energy transfer only), while the smaller circle is that for inelastic scattering (translational to internal energy conversion). The momentum of scattered ions may be shown to be

$$P = F\cos\theta + (R^2 - F^2\sin^2\theta)^{\frac{1}{2}}. \tag{12}$$

Making use of equation 12 and the equalities

$$\begin{aligned} F^2 &= 2M^3E_o/(M+m)^2, \\ E_s &= mE_o/(M+m), \\ R_e &= mF/M, \\ R_i &= mF(1 - \Delta E/E_s)^{\frac{1}{2}}/M, \text{ and} \\ E &= P^2/2M, \end{aligned} \tag{13}$$

the difference in kinetic energy of elastically and inelastically forward scattered ions at a given laboratory scattering angle θ is given by

$$E_e - E_i = \frac{m\Delta E}{M+m} + \frac{2ME_o\cos\theta}{(M+m)^2} \times \left((m^2 - M^2\sin^2\theta)^{\frac{1}{2}} - \left[1 - \frac{(M+m)\Delta E}{mE_o} \right]^{\frac{1}{2}} \times \left[m^2 - \frac{M^2\sin^2\theta}{1 - \{(M+m)\Delta E/mE_o\}} \right]^{\frac{1}{2}} \right), \quad (14)$$

where E_o is the energy of the incident ion mass M, m is the mass of the target molecule or ion, and ΔE is the internal excitation of the inelastically scattered ion.

If the incident ion is diatomic and inelastic collisions proceed via translational to vibrational energy transfer, ΔE is calculated from (73)

$$\Delta E = hc\omega_e(v'-v) - hc\omega_e x_e\left[(v'+\tfrac{1}{2})^2 - (v+\tfrac{1}{2})^2\right], \quad (15)$$

in which h is Planck's constant, c is the speed of light, ω_e and $\omega_e x_e$ are spectroscopic constants, and v and v' are vibrational quantum numbers of the diatomic species in its initial and final states respectively. Rotational excitation may be included in equation 15 by addition of the appropriate terms.

Previous Investigations

Most experimental studies of collision induced vibrational excitation have examined the bulk properties of

gases, from which it is difficult to extract information about individual collisions. Beam experiments are a more attractive alternative for such studies since the energy, mass, position, and scattering angle of the interacting ions may be very precisely defined.

Collisions of Li^+ with H_2 were analyzed by Schoettler and Toennies (74) from the velocity spectrum of back-scattered ions using a time-of-flight technique. Inelastic processes corresponding to vibrational excitation of H_2 were identified and, while individual vibrational transitions could not be completely resolved, the probabilities of multiquantum transitions were found to increase as the kinetic energy of incident Li^+ increased from 10 to 50 eV. Improved resolving power in a later experiment of Held, Schoettler, and Toennies (75) enabled them to obtain relative excitation probabilities and absolute differential cross sections for the $v=0 \rightarrow v'=1 \cdots 9$ vibrational transitions of H_2 struck by Li^+.

Vibrational excitation of H_2 and D_2 from K^+ collisions was reported by Dittner and Datz (76), who also used time-of-flight techniques. No cross sections were reported, but inelastic energy loss was found, in general, to increase with increasing relative collision energy.

Moore and Doering (77) observed unusually large cross sections for pure vibrational excitation in collisions of 100-600 eV H^+ and H_2^+ with H_2, D_2, and N_2. They also (78)

reported electronic transitions of the target molecule to occur upon bombardment of N_2, CO, C_2H_2, and C_2H_4 with 150-500 eV H^+ and H_2^+.

Relative transition probabilities were found by Moran and Cosby (79) to be relatively constant for nonreactive inelastic Ar^+ and D_2 interactions. Competition between channels of reaction was observed for this system in the 11-17 eV range, as kinetic energy may be transferred into D_2 vibrational excitation or Ar^+ electronic excitation or both.

In a subsequent paper (80), Cosby and Moran reported vibrational excitation in collisions involving oxygen ion beams. Inelastic energy loss in $O^+ + O_2$ and $O_2 + Ar$ collisions was studied with a beam apparatus which scanned the mass, angle, and energy of the forward-scattered ions. Energy losses calculated from equation 14 for vibrational excitation of the diatomic species agreed with observed maxima in the scattered ion intensities, and higher vibrational transitions were found to predominate as the laboratory scattering angle was increased from 0 to 25 degrees and incident ion kinetic energy was increased from 10 to 20 eV. The experimentally measured transition probabilities were used to test the validity of theoretical models of collisional energy transfer.

CHAPTER IV

H_3^+ VIBRATIONAL FREQUENCIES FROM ION IMPACT SPECTROSCOPY

Introduction

Previous experiments mentioned in the preceding chapter generally involved attempts to secure cross sections, impact parameters, and transition probabilities for collision phenomena of molecules whose spectroscopic parameters are well known. Examination of equation 14 reveals an intriguing possibility: Can inelastic energy loss (E_e-E_i) be used to determine spectroscopic excitation energy (ΔE) and thence vibration frequency? H_3^+ has been observed in mass spectrometers for many years (81) and the mechanism of its formation by $H_2^+ + H_2$ reactions is well understood (82). Optical measurements of the H_3^+ spectroscopic constants have proved difficult, however.

Experimental

For reactants of known mass and velocity at a given laboratory scattering angle, the only unknown in equation 14 is ΔE; hence, experimental measurement of the inelastic energy loss in the collision

$$H_3^+ + Ne \rightarrow H_3^{+*} + Ne \qquad (16)$$

allows determination of the internal energy states of H_3^+. E_e-E_i was measured with the tandem mass spectrometric apparatus shown in Figure 21 and exhaustively described by Cosby (83). The apparatus directs mass analyzed low energy ion beams onto target molecules and scans the energy, mass, and angular distribution of charged interaction products. The reactant H_3^+ is produced via $H_2^+ + H_2$ ion-molecule reactions in the high pressure ion source. H_3^+ so formed has been shown to equilibrate with neutral H_2 background gas by relatively few collisions (84); hence, H_3^+ emerging from the ion source is essentially in the ground vibrational state under these experimental conditions.

This H_3^+ is then accelerated, mass separated from H^+ and H_2^+ by a 60° Nier mass spectrometer, decelerated to 16 eV, and focused into the interaction region containing Ne. The angular, mass, and velocity distributions of scattered H_3^+ are then measured with a 127° electrostatic sector, mass filter, and associated counting equipment. The forward-scattered ion current consists primarily of elastically scattered H_3^+ with the inelastically scattered ions appearing as humps on the low energy side of the elastic peak. The inelastic processes are resolved by numerical subtraction of elastically scattered ion intensity from total scattered ion intensity and the resulting energy loss spectra for laboratory scattering angles $\theta=0^\circ$ and 10° are shown in Figure 22.

Since the inelastically scattered ions reach the de-

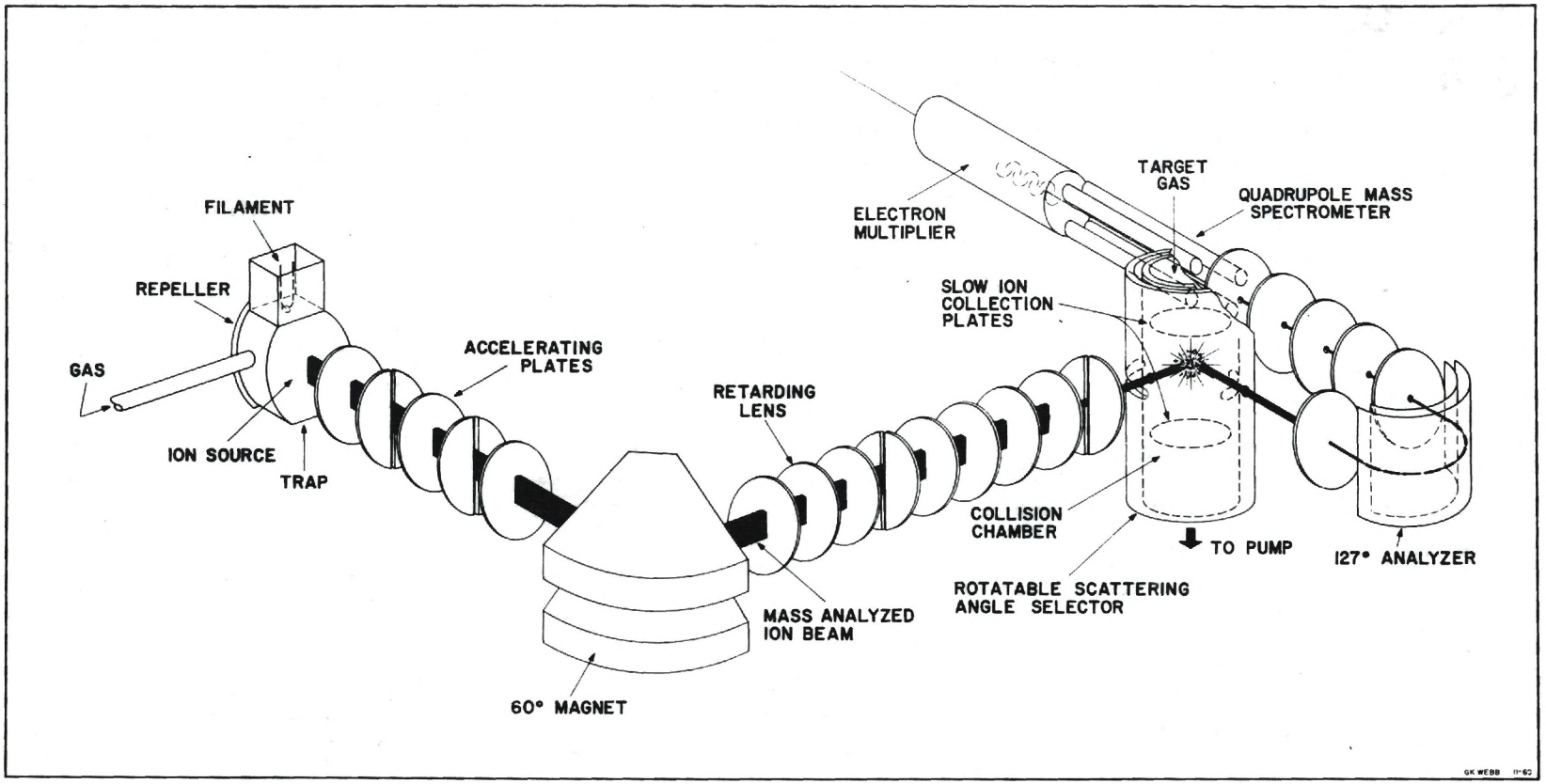

Figure 21. Tandem Mass Spectrometer Used to Obtain Ion Impact Spectra of H_3^+.

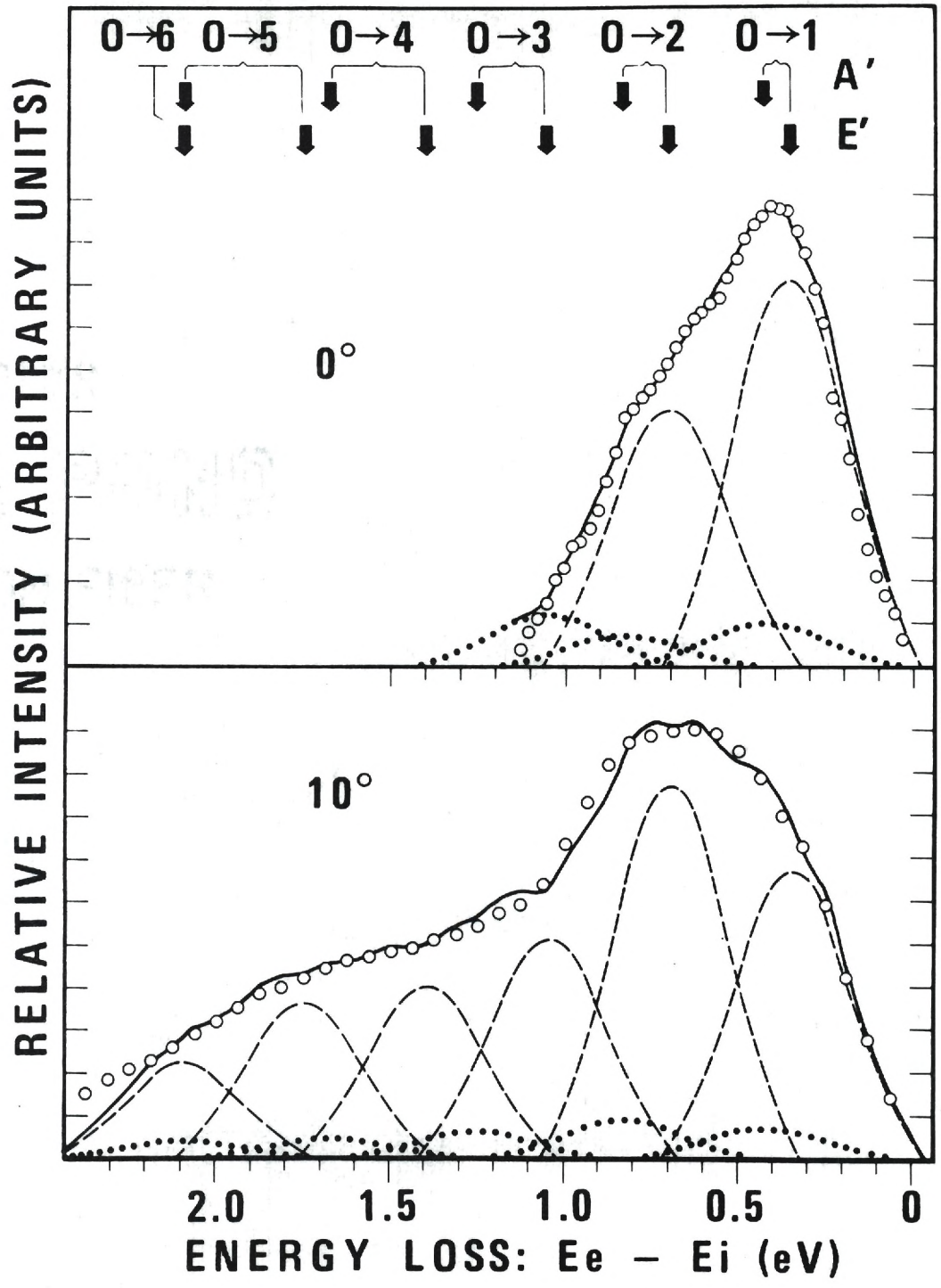

Figure 22. H_3^+ Energy Loss Spectra from H_3^+ + Ne — H_3^{+*} + Ne Interactions at LAB Angles of 0 and 10 degrees.

tector with less kinetic energy than those that are elastically scattered, translational-to-internal energy transfer must occur by collision, and vibrational-rotational excitation of H_3^+ is the only process which can account for the inelastic energy loss. The observed energy loss corresponds to that expected for vibrational transitions. Peak broadening suggests simultaneous rotational excitation, but this could not be resolved.

Results and Discussion

Theoretically calculated H_3^+ vibration frequencies are listed in Table 2. If these frequencies are used to calculate inelastic energy losses by equation 14, a direct comparison with experiment can be made. The predicted positions of the energy loss peaks associated with excitation of H_3^+ symmetric stretching A' and doubly degenerate bending modes E', given by the arrows in Figure 22, have been calculated using Christoffersen's frequencies and a harmonic oscillator approximation. The solid lines are obtained by summing the individual transition curves, which are the dotted and dashed lines.

Specific excitations appear as rather broad peaks due to thermal movement of Ne target gas and the energy spread of the incident H_3^+ beam, since energy resolution must be experimentally sacrificed for sufficient beam intensity. Experimental energy loss spectra presented as the open cir-

Table 2. Spectroscopic Data for H_3^+.

Investigator and Method	E(a.u.)	R(bohr)	ω(cm^{-1}) A'(stretch)	ω(cm^{-1}) E'(bend)
Borkman (85) SCCI, 85 terms Slater orbitals	-1.3392	1.639	3294 3450*	2850*
Christoffersen (86) MCCI, 12 terms Slater orbitals	-1.3326	1.658	3354 3400*	2790 2850*
Schwartz and Schaad (87) CI, Gaussian orbitals	-1.3376	1.650	3301	
Ellison et al. (88) Diatomics-in-molecules	-1.357	1.76	3450	2330
Pearson et al. (89) CI, 18 terms Gaussian orbitals	-1.319	1.66	3610	4440
Hirschfelder (90) CI, MO	-1.293	1.79	1550	1100
This Work Experimental			3350±200	2800±150

*Corrected for anharmonicity.

cles in Figure 22 for $\theta=0^{\circ}$ and 10° are to be compared with the solid lines calculated from theoretical H_3^+ frequencies.

Attempts to fit the experimental energy loss data have ruled out all sets of frequencies other than those of Borkman and of Christoffersen, since the other calculations predict maxima and minima inconsistent with the experimental data. Although they only calculated one frequency, Schwartz and Schaad's value is also confirmed by experiment. Higher vibrational transitions predominate when H_3^+ is scattered to larger laboratory angles, giving indication of more violent encounters at smaller impact parameters, as shown by comparison of the 0° and 10° data.

The area under an individual curve is proportional to the probability of the corresponding transition. The best fit to the experimental data at 0° is obtained with the ratio of curve areas corresponding to the approximate relative transition probabilities - E': $P_{0\rightarrow 1}=0.50$, $P_{0\rightarrow 2}=0.33$, $P_{0\rightarrow 3}=0.07$; A': $P_{0\rightarrow 1}=0.06$, $P_{0\rightarrow 2}=0.04$.

Conclusions

Ion impact spectroscopy is a useful technique for estimating vibrational frequencies of molecules such as H_3^+ whose optical measurement is difficult. Experimental energy loss spectra for vibrational excitation of H_3^+ confirm vibrational frequencies calculated by Borkman and Christoffersen within $\pm$ 200 cm^{-1}. Transitions involving doubly degenerate

H_3^+ bending modes are dominant under the conditions of these experiments.

CHAPTER V

THEORY OF VIBRATIONAL EXCITATION BY COLLISION

Introduction

Theoretical calculations on simple collision systems such as the archetypal A + BC encounter have received considerable attention in recent years (91-93). Approaches to the problem of estimating transition probabilities and interaction potentials have ranged from the exact quantum mechanical calculations of Secrest and Johnson (94) to the exact classical calculations of Kelley and Wolfsberg (95).

Semiclassical Treatment

Between these extremes is the semiclassical treatment developed by Treanor (96) in which the collision is described in terms of a quantum mechanical harmonic oscillator perturbed by a linear forcing potential

$$V(r,d) = \tfrac{1}{2}kY^2 - YF(t), \qquad (17)$$

where d is the internuclear distance of molecule BC, r is the distance from atom A to the center of mass of BC, k is the harmonic oscillator force constant of BC, F(t) is the force on the oscillator due to collision A+BC, $Y=d-d_o$, and d_o is the BC equilibrium internuclear distance. The time-

dependent Schroedinger equation for this system may be written as

$$-\frac{\hbar^2}{2\mu}\frac{\partial^2\psi}{\partial Y^2}+\left[\tfrac{1}{2}kY^2-YF(t)\right]=i\hbar\frac{\partial\psi}{\partial t} \tag{18}$$

in which μ is the reduced mass of BC.

Kerner (97) has obtained a solution to equation 18 by using the transformations

$$\psi(Y,t)=\varphi\left[Y-u(t),t\right]\exp\left[Yg(t)\right] \tag{19}$$
$$\zeta(Y,t)=Y-u(t)$$

where $g(t)$ and $\varphi(\zeta,t)$ are undetermined functions. g and u are chosen such that equation B is separable in the variables ζ and t with the solution

$$\psi_m(Y,t)=N_m\exp(\tfrac{i}{\hbar}\mu Y\dot{u})\exp(-\tfrac{i}{\hbar}\int_o^t(\delta+E_n)dt) \tag{20}$$
$$\times\exp(\tfrac{1}{2}\alpha^2(Y-u)^2\,H_m\left[\alpha(Y-u)\right],$$

where $\delta=\frac{1}{2}\mu\dot{u}^2-\frac{1}{2}ku^2$, N_m is a normalization factor $(\alpha/\pi^{\frac{1}{2}}2^n n!)^{\frac{1}{2}}$, $\alpha^2=(\mu k)^{\frac{1}{2}}/\hbar$, H_m is the mth Hermite polynomial, and $E_m=(m+\frac{1}{2})\hbar\omega$ is the energy of the mth vibrational state of the harmonic oscillator. This solution may be interpreted as describing an oscillating wave packet whose center moves under the

equations of motion of the classical forced oscillator

$$\mu\ddot{u} + ku = F(t). \tag{21}$$

Following the procedure of Treanor (96), the wave function for the forced oscillator in the vibrational state m, $\psi_m(Y,t)$, may be expanded in terms of the complete set of normalized harmonic oscillator wave functions

$$\chi_n(Y,t) = N_n \exp(\tfrac{1}{2}\alpha^2 Y^2) H_n(\alpha Y) \exp(-iE_n t/\hbar) \tag{22}$$

such that

$$\psi_m(Y,t) = \sum_o^\infty b_{mn}(t)\chi_n(Y,t). \tag{23}$$

Hence

$$b_{mn} = \int_{-\infty}^{t} \chi_n \psi_m dt, \tag{24}$$

where the course of the collision occurs in the interval $t=-\infty$, $r=\infty \rightarrow t=\infty$, $r=\infty$. Using equations 20 and 22, Treanor has integrated equation 24 to obtain

$$b_{mn} = (-1)^m (m!n!)^{\frac{1}{2}} \exp(-\tfrac{1}{2}\epsilon_o) S_{mn} \epsilon_o^{(m+n)/2} \tag{25}$$

$$\times \exp\left[-i(m-n)(\omega t+\Theta_t) - \frac{i}{\hbar}\left(\int_{-\infty}^{t} \delta dt - \mu \frac{\dot{u}u}{2}\right)\right]$$

where

$$S_{mn} = \sum_{j=0}^{z} \frac{(-1)^j \epsilon_o^{-j}}{(n-j)!\, j!\, (m-j)!}, \tag{26}$$

$$\Theta_t = \tan^{-1}(\dot{u}/\omega u), \tag{27}$$

z is the lesser of m and n, $\omega = 2\pi\nu$ is the angular frequency of the oscillator and

$$\epsilon_o(t) = (\tfrac{1}{2}\mu\dot{u}^2 + \tfrac{1}{2}ku^2)/\hbar\omega. \tag{28}$$

It can be seen that ϵ_o is simply the energy a classical oscillator would absorb if acted on by the forcing potential divided by $\hbar\omega$, and will be written

$$\epsilon_o = \frac{\Delta E_c}{\hbar\omega}. \tag{29}$$

If the oscillator is in state m at $t=-\infty$, the probability of finding it in state n at time t is the square of the magnitude of the expansion coefficient b_{mn},

$$P_{mn} = \left| b_{mn} \right|^2 = m!n!e^{-\epsilon_o}\epsilon_o^{(m+n)}S_{mn}^2. \qquad (30)$$

For the particular case in which the oscillator is originally in its lowest vibrational level (m=0),

$$P_{o,n} = (\frac{1}{n!})e^{-\epsilon_o}\epsilon_o^{n}. \qquad (31)$$

Shin (98) has also derived equation 17 with a time-independent Schroedinger equation using Green's functions.

The problem, then, revolves around choice of a suitable interaction potential to give F(t), and thence the transition probabilities. The above mentioned studies assume the model of a diatomic molecule interacting with an atom which is approaching along the molecular line of oscillation, i.e. linear encounters with zero impact parameter. Considering the obviously primitive nature of such models, what success they have enjoyed in predicting experimental results (80,83) may be fortuitous.

Oriented Nonlinear Encounters

A more physically realistic model is one which includes consideration of impact parameter b, defined as the distance separating asymptotes to the trajectories of the colliding partners, and the rotational orientation of the diatomic molecule. H. K. Shin (99) has formulated a proce-

dure for evaluating the vibrational energy transfer ϵ_o with such a model in order to show how non-zero impact parameters and oriented encounters affect the collision process.

The collision model for the oriented nonlinear encounter of AB+C is shown in Figure 23. The Lennard-Jones potential used to describe the interaction in terms of the coordinates defined in Figure 23 is

$$U(r_1,r_2) = 2D \sum_{i=1}^{2} \left(\frac{\sigma}{r_i}\right)^{12} - \left(\frac{\sigma}{r_i}\right)^{6} ; \qquad (32)$$

where

$$r_{1,2}^2 = r^2 \mp 2D(d+x)rS_{2,1}\cos\chi + (d+x)^2S_{2,1}^2 ; \qquad (33)$$

$S_{1,2}=m_{B,C}/(m_B+m_C)$; D, σ are the L-J potential parameters; d is the equilibrium bond distance of BC; and x is the vibrational amplitude. Neglecting terms in (d+x)/r of third or higher order (i.e. $r \gg d/2$) leads to an overall interaction energy

$$U(r,x,\chi) = 4D\left[\left(\frac{\sigma}{r}\right)^{12} - \left(\frac{\sigma}{r}\right)^{6}\right] \qquad (34)$$

$$+ 24D\left[\left(\frac{\sigma}{r}\right)^{12} - \tfrac{1}{2}\left(\frac{\sigma}{r}\right)^{6}\right](S_2-S_1)\left(\frac{d+x}{r}\right)\cos\chi$$

$$+ 4D\left[(42\cos^2\chi-3)\left(\frac{\sigma}{r}\right)^{12} - (12\cos^2\chi-\tfrac{3}{2})\left(\frac{\sigma}{r}\right)^{6}\right](S_1^2+S_2^2)\left(\frac{d+x}{r}\right)^2 .$$

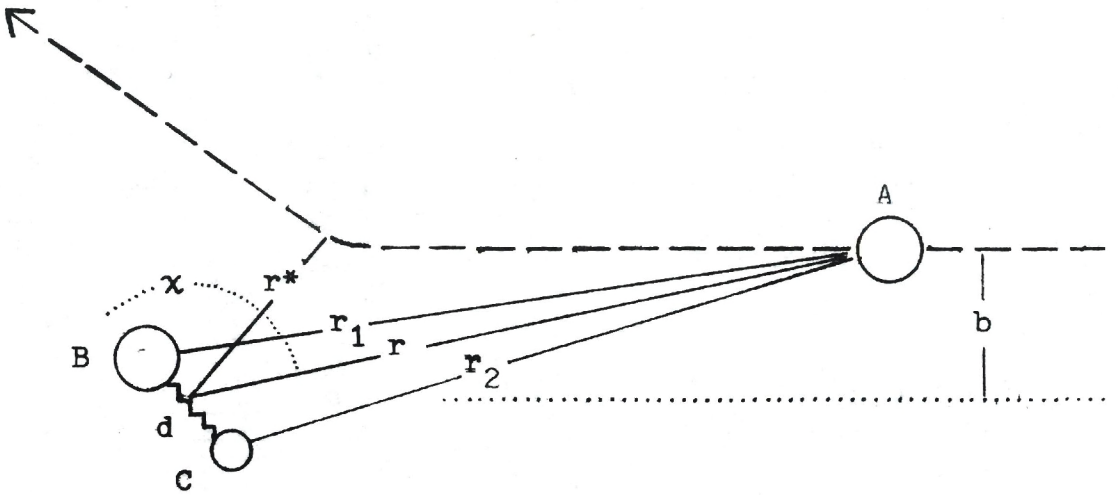

Figure 23. Collision Model for Oriented Nonlinear Encounter of BC+A.

The force acting on the molecule in the collision is calculated from equation 21 by establishing the dependence of r on time from the equation of motion

$$t = (\tilde{\mu}/2)^{\frac{1}{2}} \int_{r^*}^{r} \frac{dr}{E_o - E_o(\frac{b}{r})^2 - U(r,0,\chi)^{\frac{1}{2}}}, \qquad (35)$$

where $\tilde{\mu}$ is the reduced mass of the collision system, E_o is the initial relative kinetic energy, r^* is the largest root of the radical in the denominator, and $U(r,0,\chi)$ is obtained from equation 21 by choosing a particular molecular orientation χ.

From the time-dependent driving force

$$F[r(t)] = 24\,(\tfrac{D}{\sigma})(S_2-S_1)\cos\chi\left[(\tfrac{\sigma}{r})^{13} - \tfrac{1}{2}(\tfrac{\sigma}{r})^{7}\right] \qquad (36)$$

$$+ 8(Dd/\sigma^2)(S_1^2+S_2^2)\,(42\cos^2\chi-3)(\tfrac{\sigma}{r})^{14} - (12\cos^2\chi-\tfrac{3}{2})(\tfrac{\sigma}{r})^{8},$$

an approximate analytic solution for ϵ_o may be found

$$\epsilon_o = (2/\mu h\omega)\left[(6d\pi\mu\omega/7)(S_1^2 + S_2^2)(\cos^2\chi - \tfrac{1}{14})\right]^2 \qquad (37)$$

$$\times\left[1 - (\frac{4\cos^2\chi - \frac{1}{2}}{14\cos^2\chi - 1})(\frac{1}{\Gamma(8/7)\gamma^{6/7}}) + (\frac{14D\gamma}{d\sigma\mu\omega^2})\right.$$

$$\chi\left(\frac{S_1 - S_2}{S_1^2 + S_2^2}\right)\left(\frac{\cos\chi}{\cos^2\chi - 1/14}\right)\left(1 - \frac{2\gamma^{6/7}}{\Gamma(13/7)}\right)\Bigg]^2 \exp(-2\omega\tau),$$

where

$$\gamma = (\omega a/14)(\tilde{\mu}/2D)^{\frac{1}{2}}, \tag{38}$$

$$a = \frac{\sigma}{\pi^{\frac{1}{2}}}\frac{\Gamma(7/12)}{\Gamma(\frac{1}{2})}\left(\frac{4D}{E_o}\right)^{\frac{1}{12}}\left[1 - \frac{1}{72}\left(\frac{\Gamma(\frac{1}{2})}{\Gamma(7/12)}\right)^2\left(\frac{D}{E_o}\right)^{\frac{1}{2}}\right]\left[1 - \frac{2}{\pi}\left(\frac{D}{E_o}\right)^{\frac{1}{2}}\right]^{-1},$$

$$\tau = \frac{\Gamma(7/12)}{\Gamma(1/12)}\left(\frac{\pi\tilde{\mu}}{2}\right)^{\frac{1}{2}}\frac{\sigma(4D\rho_1)^{1/12}}{E_o^{7/2}}\left[1 - \frac{1}{72}\left(\frac{\Gamma(1/12)}{\Gamma(7/12)}\right)^2\left(\frac{D}{E_o}\right)^{\frac{1}{2}}\frac{\rho_2}{\rho_1^{\frac{1}{2}}}\right]$$

$$+ \frac{5}{144}\frac{\Gamma(5/12)}{\Gamma(11/12)}\left(\frac{\pi\tilde{\mu}}{2}\right)^{\frac{1}{2}}\frac{b^2}{\sigma(4D)^{1/12}\rho_1^{1/6}E_o^{5/12}},$$

$$\rho_1 = 1 + 6(S_2 - S_2)\left(\frac{d}{r_*}\right)\cos\chi + (42\cos^2\chi - 3)(S_1^2 + S_2^2)\left(\frac{d}{r_*}\right)^2, \text{ and}$$

$$\rho_2 = 1 + 3(S_2 - S_1)\left(\frac{d}{r_*}\right)\cos\chi + (12\cos^2\chi - \tfrac{3}{2})(S_1^2 + S_2^2)\left(\frac{d}{r_*}\right)^2.$$

Thus the Shin oriented nonlinear encounter method enables one to calculate; for a given incident energy E_o, reduced impact parameter b^*, and molecular orientation χ; the energy transferred by collision ϵ_o. This ϵ_o is then used in equation 31 to calculate the probability that a diatomic molecule in its ground vibrational level will be excited to a final level n on collision with a target atom.

Since molecules in ion-impact experiments will be randomly oriented, $U(r,\chi)$ and $P_{0,n}$ are calculated for many χ to give probabilities of excitation averaged over all molecular orientations.

CHAPTER VI

CO^+ VIBRATIONAL AND ROTATIONAL EXCITATION IN LOW ENERGY COLLISIONS WITH Ar

Introduction

In order to test the applicability of the Shin model to real molecules, excitation of CO^+ on collision with Ar was studied at incident energies between 1.56 and 24.50 eV and laboratory scattering angles between 0 and 20 degrees.

Apparatus

The ion impact mass spectrometer (Figure 24) used to measure the CO^+ energy loss spectra was designed by George Turner and consists essentially of two 127^o electrostatic sectors, an ion source, a collision chamber, a quadrupole mass filter, a channel electron multiplier, focusing and defining slits, and associated electronics.

Description

Ions are generated by gas phase electron impact ionization in a source (not shown) similar to that described by Cosby (83) and are removed from the source by a drawout potential, accelerated through a split-plate focusing slit, then decelerated into the primary ion energy defining sector (sector I). The cylindrical plates of this sector are fine mesh wire screens, to reduce space charge caused by out-of-

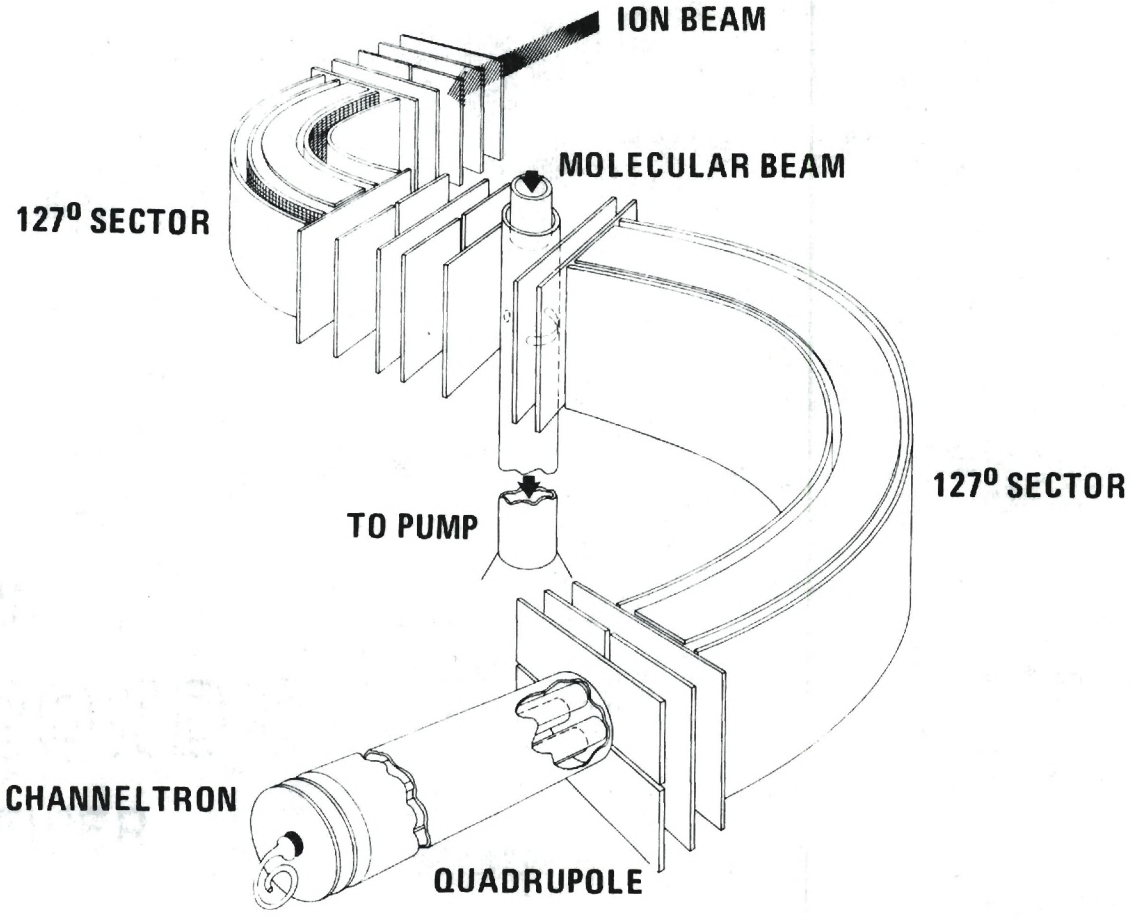

Figure 24. Schematic Diagram of Ion Impact Spectrometer Used to Measure Energy Loss Spectra of CO^+ Inelastically Scattered from Ar.

focus ions and provide non-sputtering surfaces. Space charge is further reduced by applying a voltage attractive to the ions on the two outer plates paralleling the sector. Ion transmission by the sector is improved with a repulsive positive voltage on the vertical focus plates.

Ions exiting sector I are accelerated and focused through another series of slits into the collision chamber, comprised of a stainless steel cylinder on which the entire primary ion generating train is mounted. The entire scattered ion detection system may be rotated about the collision chamber from -15° to $+90^{\circ}$ with respect to the incident ion beam. Neutral target atoms enter the collision chamber through a sintered glass capillary array which effectively removes two translational degrees of freedom from the target atoms while aiming them into a well defined collision region of about 1/8" diameter.

After collision, the scattered ion acceptance angle is defined by the two entrance slits of sector II, where energy analysis of the scattered beam occurs. Sector II plates are solid, and vertical focusing similar to that of sector I is provided. Ions exit sector II and are focused into the mass filter through a vertical-horizontal split plate assembly. Mass analysis of the scattered ion beam is provided by an Ultek EAI QUAD 150 mass filter. A channel electron multiplier (100) detects the energy-angle-mass analyzed ions. Pulses from the channeltron are amplified,

shaped, and displayed by an ORTEC 400 series instrument package.

Voltages to all the ion optics are furnished by BATPAK and are stable to less than a millivolt per hour.

The entire apparatus is mounted on an optical bench inside a stainless steel cylindrical vacuum chamber pumped to 10^{-7} torr background by a six inch oil diffusion pump.

A glass system with 24 liter ballast and needle valve flow rate regulation provides gas for both primary and target beams.

The kinetic energy of charged particles passing through parallel cylindrical electrostatic plates is given by $\Delta V=E[2\ln(r_2/r_1)]$, where ΔV is the difference in potential between inner and outer sector plates, E is the kinetic energy of ions passed by the sector, and r_1 and r_2 are radii of the inner and outer plates respectively (101). The quantity $2\ln(r_2/r_1)$ is the sector constant and may be experimentally determined from the slope of a ΔV vs. E plot. For sector I the calculated and experimental constants are 0.8366 and 0.824, while for sector II they are 0.6544 and 0.645.

Energy resolution, $E/\Delta E$, of an electrostatic sector is determined by its aperture width (0.010 inch entrance and exit slits on both sectors) and mean radius. ΔE is the energy spread of the beam passed by the sector FWHM. For sectors I and II, the resolution is calculated to be 221 and

231, corresponding to FWHM of 0.045 eV and 0.044 eV respectively, for a 10 eV ion beam. Experimentally, a CO^+ beam at this energy, passed by sector I and measured by sector II, has a FWHM of 0.05 eV.

Angular resolution of the apparatus is defined by the two 0.010 inch slits separated by 0.360 inch at the entrance of sector II, and is 1.5^o FWHM.

Thus, the parameters sufficient for plotting an energy loss spectrum are evaluated as follows:

a. Primary ion intensity: Read directly from an ORTEC 430 scaler in counts/second with target gas off,

b. Scattered ion intensity: Read directly from the scaler in counts/second with target gas on,

c. Laboratory scattering angle: Read directly (83) in degrees,

d. Ion mass: Selected by quadrupole mass filter,

e. Gas pressure: Measured with CVC GPH-100A discharge vacuum gauge,

f. Incident ion kinetic energy: Derived from the potential difference between the source and the collision chamber, and

g. Scattered ion kinetic energy: Determined from the ΔV of sector II and its sector constant.

Method

Energy loss spectra for low energy CO^+ + Ar collisions

are presented in Figures 25-32. In these figures, θ is the laboratory scattering angle, the energy given is that of incident CO^+, and the arrows are the expected energy loss for vibrational excitation from v=0 to v=1,2,3,··· calculated from equation 14.

Data points (dots) in these figures were obtained by first recording the total scattered ion beam intensity, which is the sum of elastically plus inelastically scattered ions and, therefore, broadened on the low energy side. The maximum intensity of the total scattered beam corresponds to the centroid of elastically scattered CO^+, and was found to occur at the energy predicted by the relation

$$E_e = \frac{M^2 E_o}{(M+m)^2}\left[2\cos^2\theta - 1 + \frac{m^2}{M^2} + \frac{2\cos\theta}{M}(m^2 - M^2\sin^2\theta)^{\frac{1}{2}}\right] \qquad (39)$$

obtained from equation 14 with M=28 and m=40.

The intensity of inelastically scattered ions as a function of $E_e - E_i$, the energy displacement from the elastic centroid, was then obtained by subtraction of elastic intensity (symmetric about elastic centroid) from total scattered ion intensity. Since the elastic peak is quite narrow (less than the vibrational spacing of CO^+), inelastic scattering with energy loss corresponding to vibrational excitation of incident CO^+ may be unambiguously resolved.

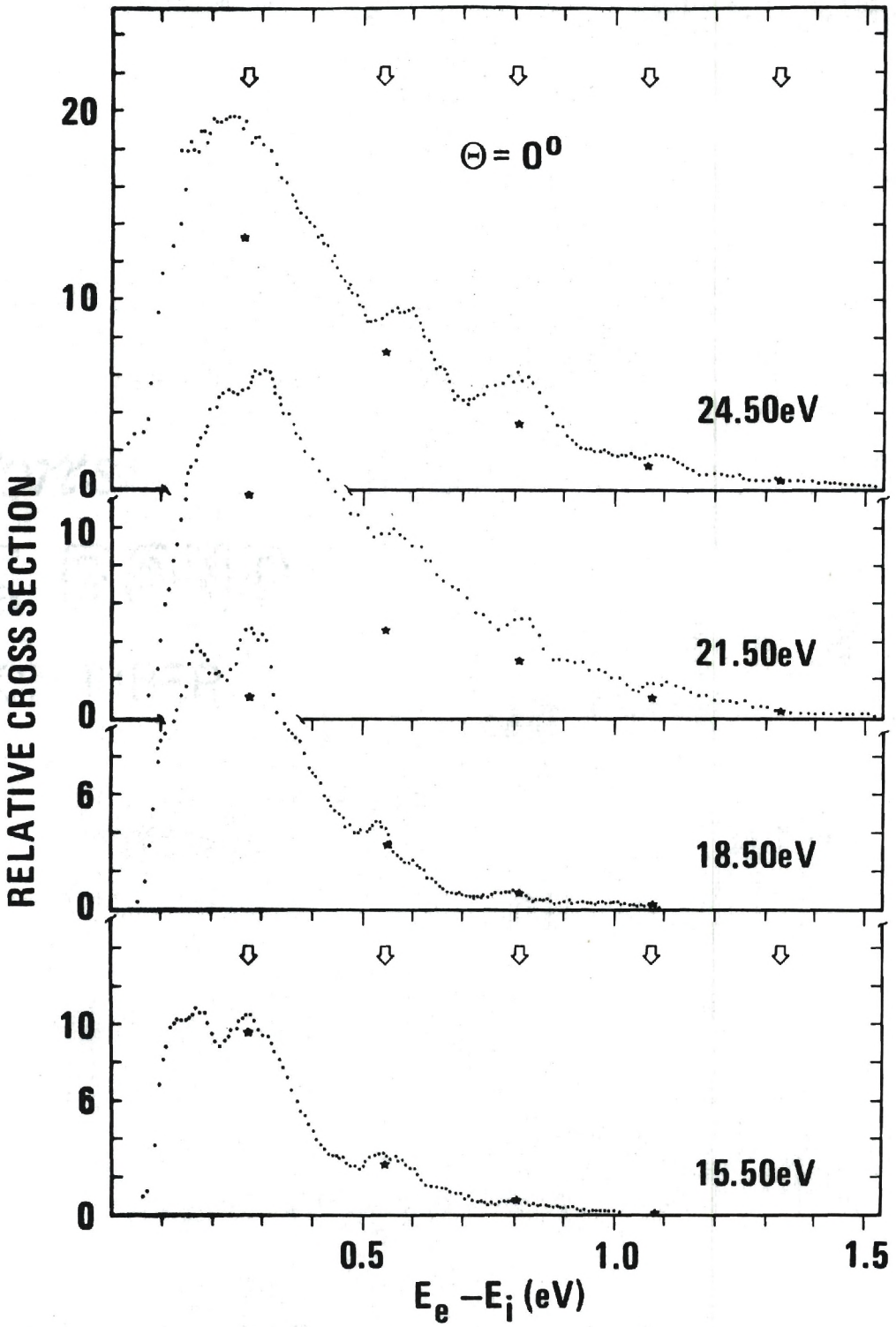

Figure 25. Energy Loss Spectra of CO^+. (Symbols are Explained in Text.)

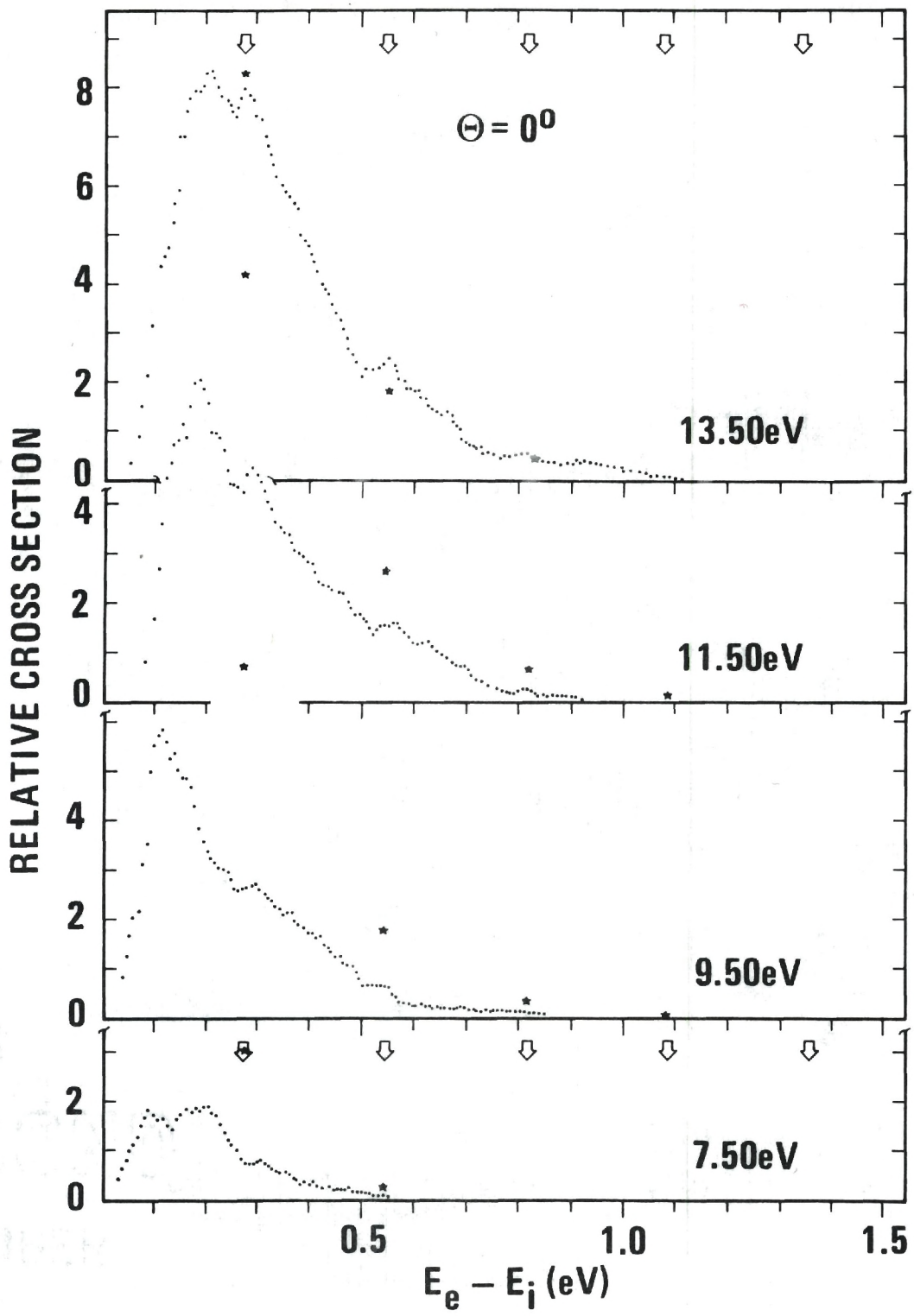

Figure 26. Energy Loss Spectra of CO^+. (Symbols are Explained in Text.)

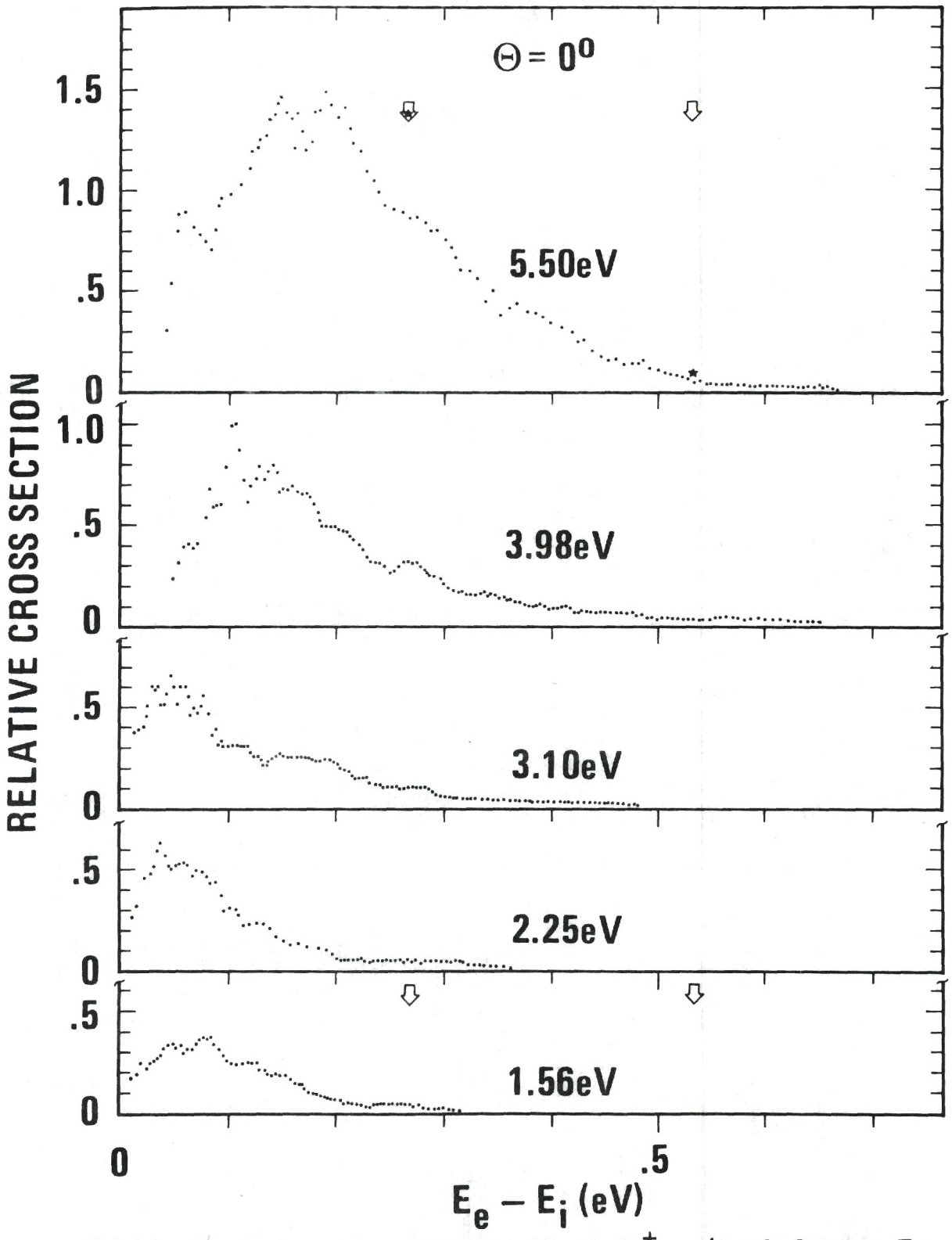

Figure 27. Energy Loss Spectra of CO^+. (Symbols are Explained in Text.)

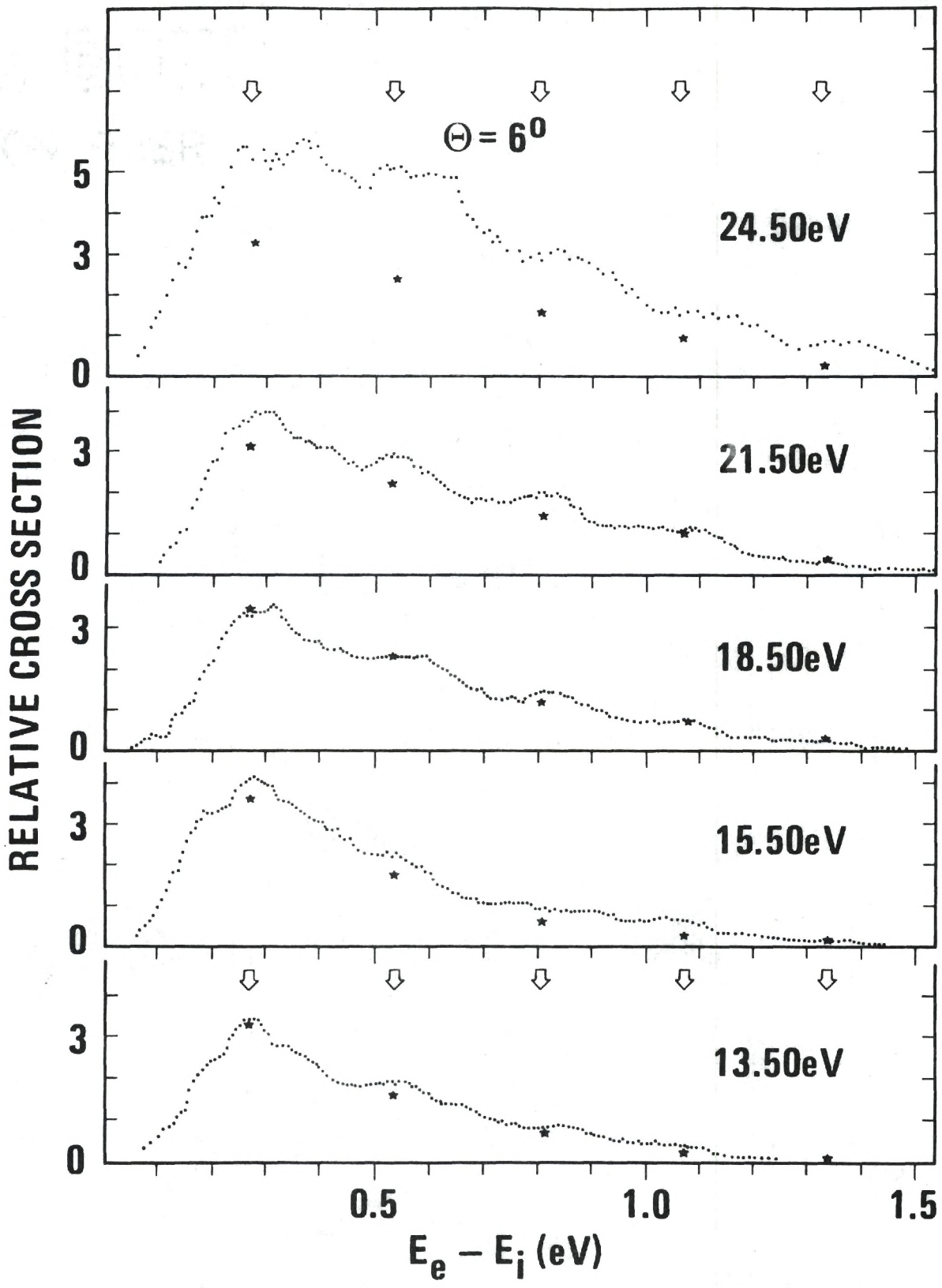

Figure 28. Energy Loss Spectra of CO^+. (Symbols are Explained in Text.)

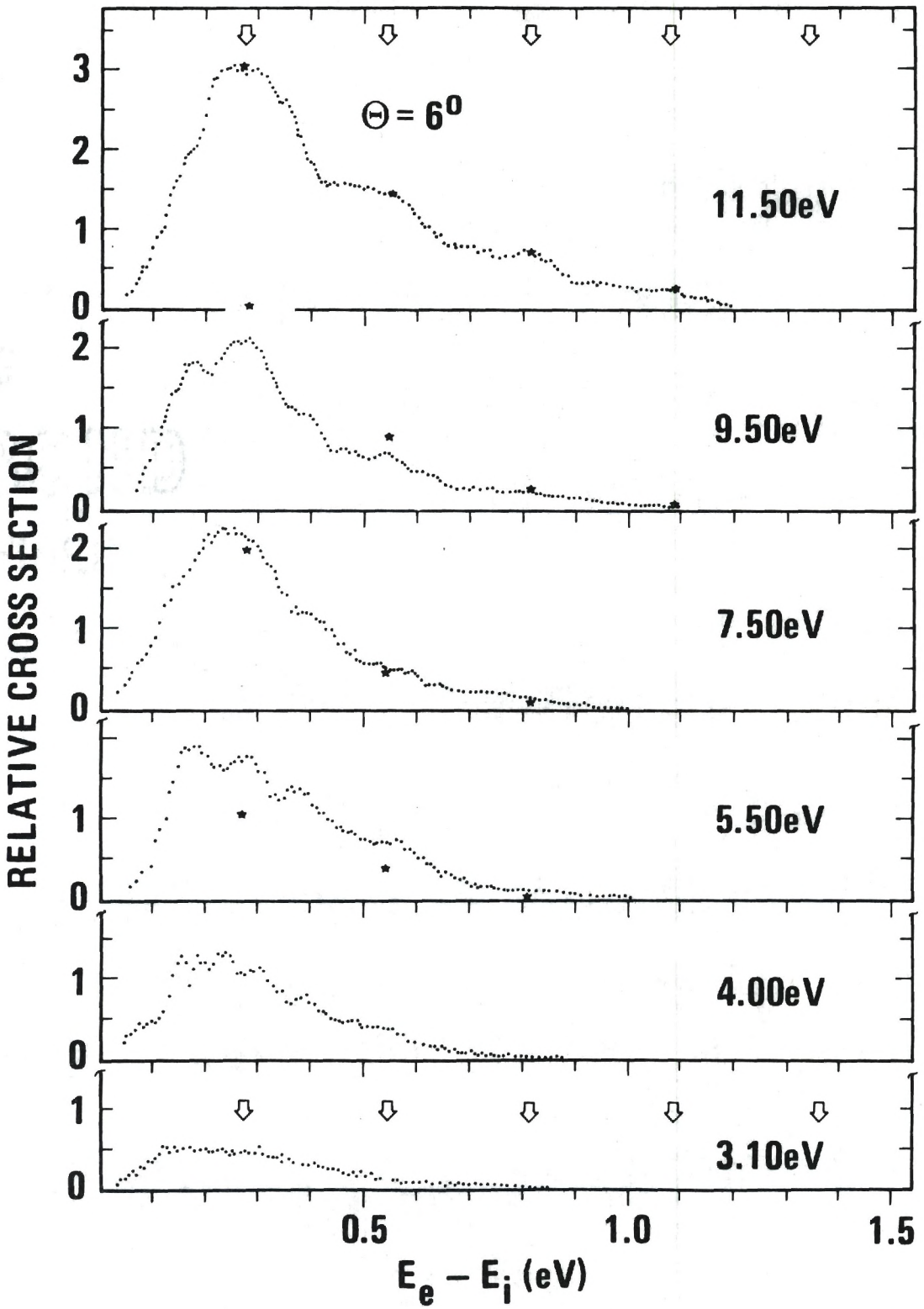

Figure 29. Energy Loss Spectra of CO^+. (Symbols are Explained in Text.)

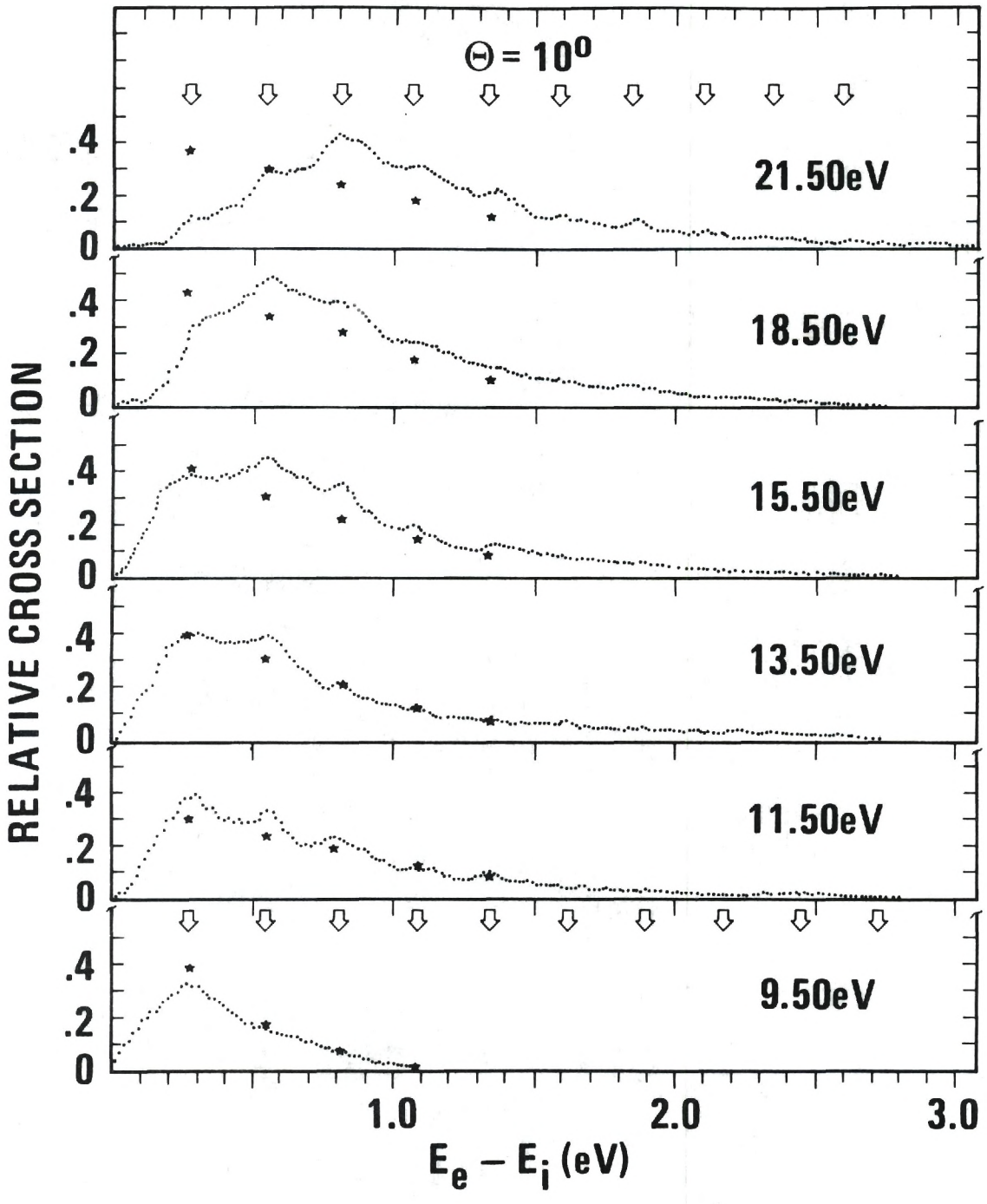

Figure 30. Energy Loss Spectra of CO^+. (Symbols are Explained in Text.)

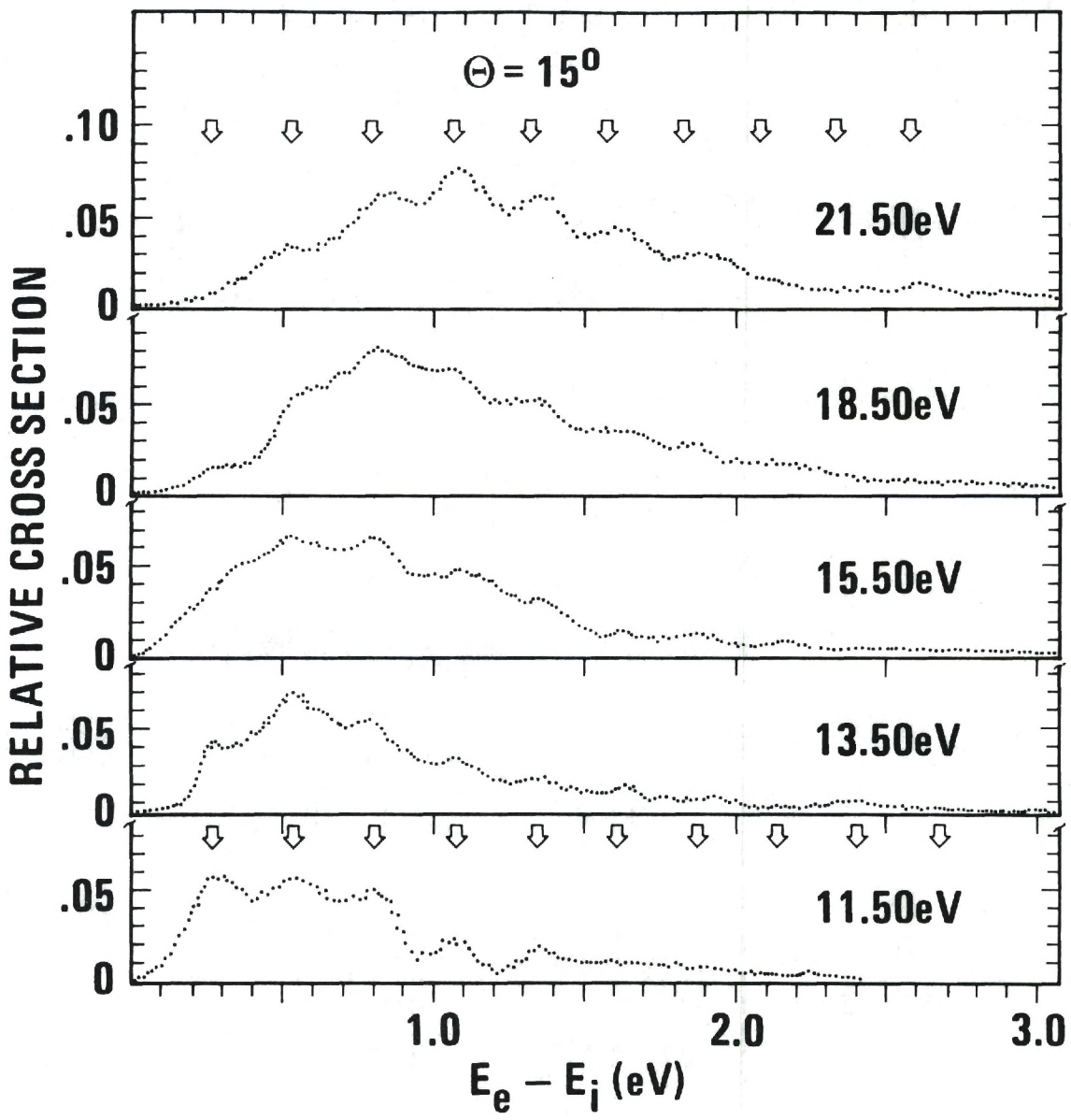

Figure 31. Energy Loss Spectra of CO^+. (Symbols are Explained in Text.)

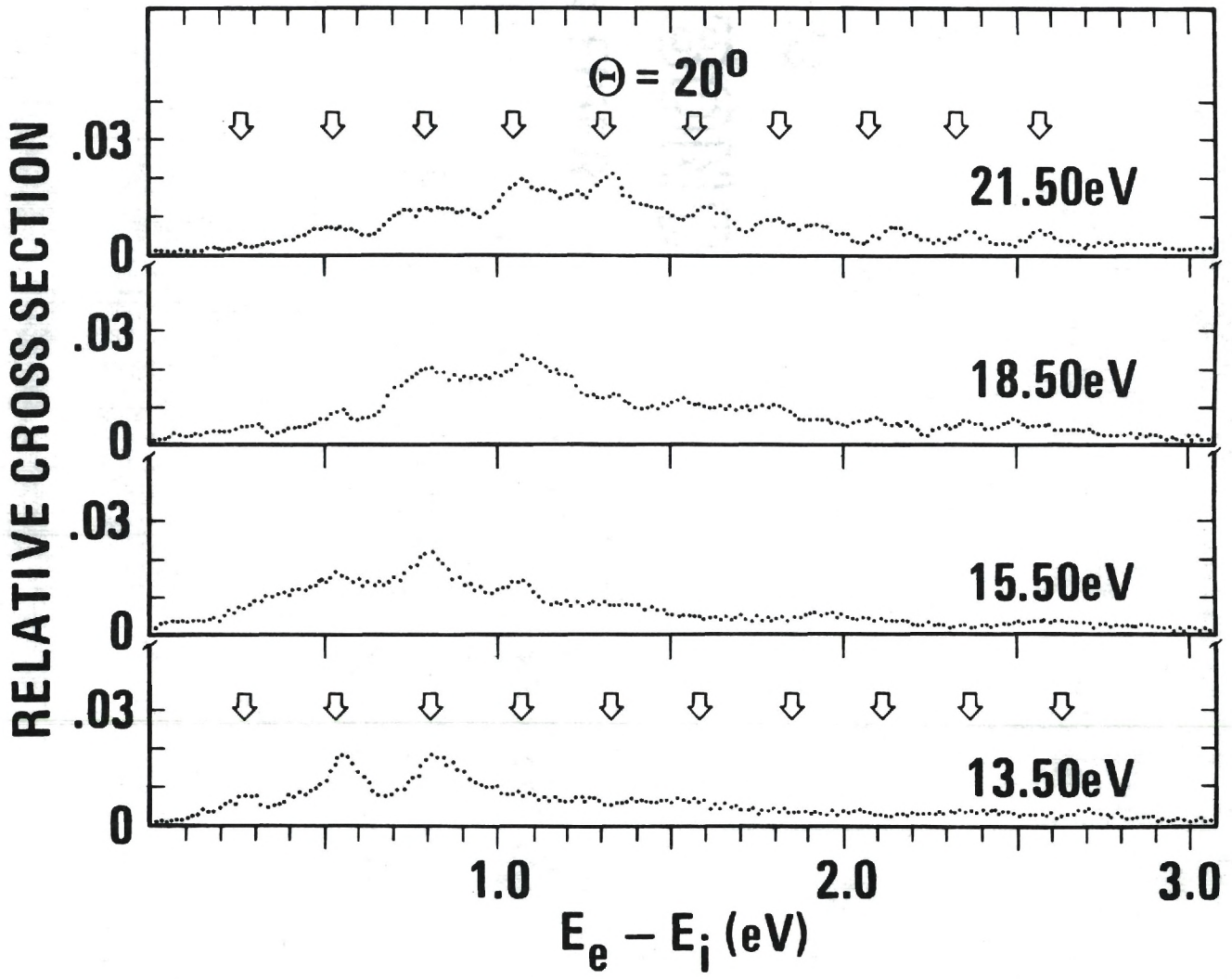

Figure 32. Energy Loss Spectra of CO^+. (Symbols are Explained in Text.)

Relative differential cross sections are obtained from scattered ion intensities by use of the equation

$$\bar{I}(\theta) = k' i_s / i_o g(\theta) \qquad (40)$$

in which i_s and i_o are intensities of the scattered and incident beam, $g(\theta)$ is the fraction of the scattering volume subtended by the detector at the laboratory scattering angle θ, and k' includes pressure dependence and a small correction term to account for the energy dependence of sector transmissivity.

Discussion of Results

General

A cursory examination of the energy loss spectra reveals several intuitively gratifying trends. First, at a given θ, higher incident energies appear to correlate with larger energy loss. Second, at a given energy, larger scattering angles correlate with larger energy loss. Third, relative cross section decreases as θ increases from 0 to 20 degrees. None of these observations are surprising, of course, since one would expect more energetic encounters to lead to greater energy loss, larger scattering angles to result from the more energetic encounters, and the likelihood of scattering to large angles to be smaller than that for small.

Comparison of Experiment with Shin's Theory

The CO^+ + Ar system furnishes a convenient test for the validity of Shin's model. Lennard-Jones parameters, $D=1.612\times10^{-14}$ erg and $\sigma=3.504$ Å, were calculated using the combining rules for the Ar-Ar and CO-CO systems (104). Spectroscopic parameters for CO^+ are (73): $\omega=2214.24$ cm^{-1}, $\omega_e x_e=15.16$ cm^{-1}, and $d=1.1150$ Å.

The ion beam used in this work was generated by 60 v electron bombardment and before collision is primarily in the v=0 vibrational level. The apparatus used does not have the resolution to distinguish between different transitions with the same Δv, i.e. $v=2\rightarrow3$, $v=3\rightarrow4$, etc., will show up as $v=0\rightarrow1$. Using Shin's method as outlined in the previous chapter, $P_{0,n}$ (averaged over all χ) was calculated and plotted as a function of E_o for n=1,2,3,4,5 and various b^* ($b^*=b/\sigma$, the reduced impact parameter).

A careful comparison of the observed experimental relative cross sections ($\propto P$) for $v=0\rightarrow1,2,3,4,5$ with the calculated $P_{0,n}$ for n=1,2,3,4,5 provided identification of the b^* which best describes the interaction at a given E_o and θ of experiment. Table 3 lists the b^* so obtained, with $U(r,\chi)$ calculated from the above parameters.

The stars in Figures 25-32 represent relative cross sections calculated from the relation (105)

Table 3. b* Characteristic of Given Interaction.*

	$\theta = 0^{o}$	6^{o}	10^{o}
E_{o}(eV) =			
24.5	1.10	1.05	
21.5	1.05	1.00	0.95
18.5	1.05	0.95	0.90
15.5	1.00	0.925	0.825
13.5	0.95	0.85	0.75
11.5	0.825	0.75	0.65
9.5	0.75	0.70	0.65
7.5	0.75	0.70	
5.5	0.65	0.30	

Error in b due to uncertainty in fitting the experimental data is ± 0.05.

$$\frac{\bar{I}_1}{\bar{I}_2} = \frac{P_1 b_1^*/\sin\phi_1}{P_2 b_2^*/\sin\phi_2} \frac{(db^*/d\phi)_1}{(db^*/d\phi)_2} \qquad (41)$$

(in which ϕ is the center of mass scattering angle) normalized to the $\theta=0^\circ$, $E_o=15.50$ eV curve, and are seen to be in reasonably good agreement with experimental relative differential cross sections for $\theta-0^\circ$ and $\theta=6^\circ$.

Limitations of Shin's Theory

Comparison of theory and experiment at $\theta=10^\circ$, on the other hand, is disconcerting in two respects. First, the numerical value of the stars has been multiplied by one-fourth in order to place them on the graph. Second, and worse, above 15.50 eV, theory predicts $v=0\rightarrow1$ to be the most likely transition, whereas multiquantum transitions are experimentally observed to predominate at higher energies. Indeed, this 10°, 15.50 eV spectrum is where Shin's theory breaks down, as applied to the present work, because it is at this energy and angle that multiquantum transitions are observed to have a higher cross section than that for $v=0\rightarrow1$; whereas Shin's theory, as a consequence of averaging P over all χ, always predicts, for all E_o and all b^*, $P_{0,1}$ to have the greatest value.

Oriented nonlinear encounters may have a preferred orientation for exciting a given series of transitions, as shown in Figure 33, where $P_{0,n}$ (n=1,2,3,4,5) are plotted as

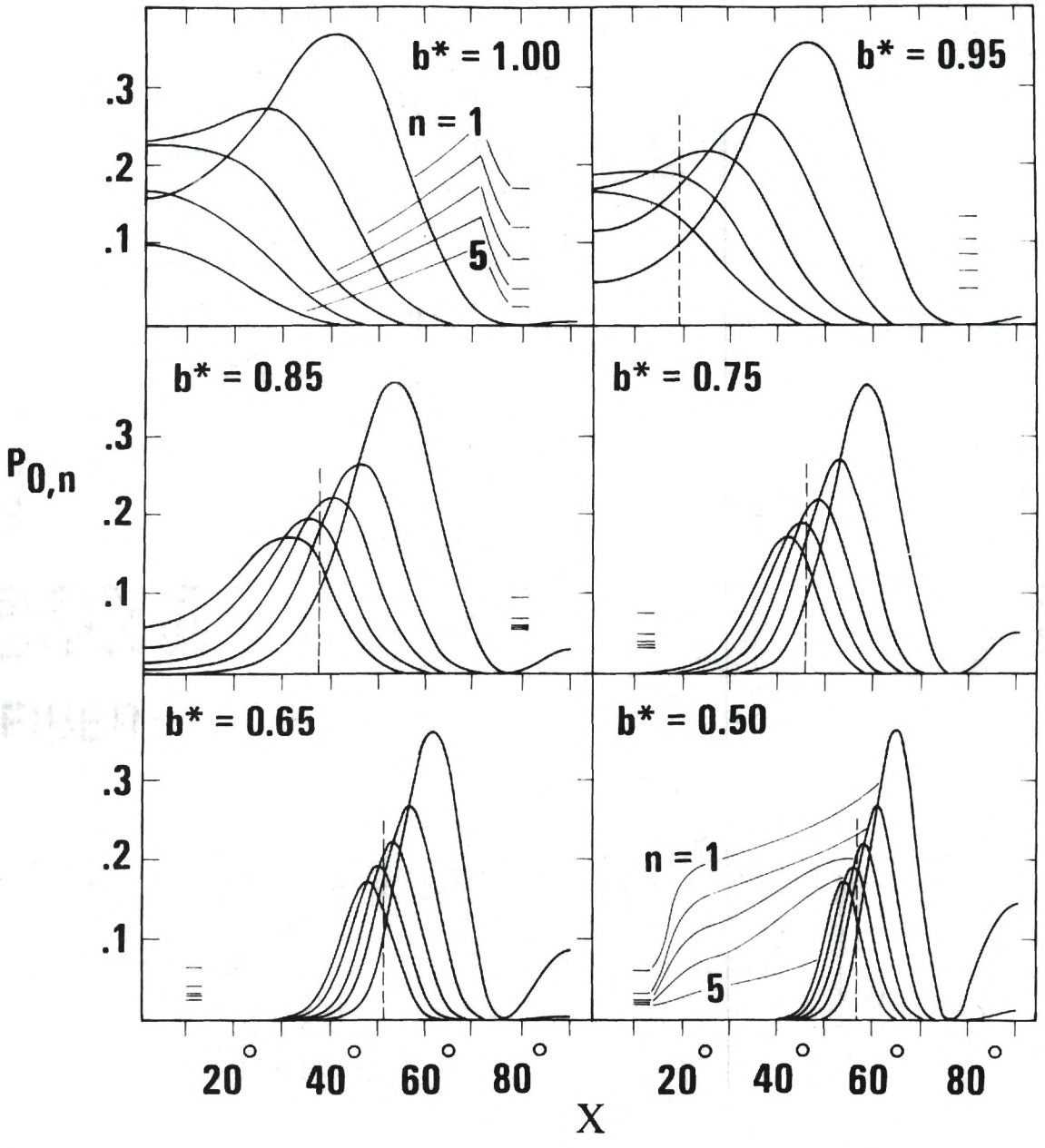

Figure 33. Preferred Orientation for Vibrational Excitation in 21.50 eV Collisions of CO^+ with Ar.

functions of molecular orientation for several b^*. E_o is 21.50 eV and the dashed vertical line indicates preferred molecular orientations which would give probabilities in agreement with observed cross sections at 10^o and 21.50 eV. Thus, for example, CO^+ colliding with Ar at 21.50 eV, $b^*=0.85$ and $\chi=37^o$, would have a transition probability greatest for $v=0\rightarrow3$ and least for $v=0\rightarrow1$.

The incident CO^+ is, however, randomly oriented prior to collision; hence, P must be averaged over all χ. These χ averaged probabilities are shown as the horizontal bars on Figure 33, and $P_{0,1}>P_{0,2}>P_{0,4}>P_{0,5}$ in all cases.

There are several shortcomings of the Shin theory, which probably account for its poor fit to high angle experimental results. Classical calculations (106) have indicated that χ is not necessarily constant during a collision, as assumed by Shin. Also, the potential does not include an r^{-4} polarization term. While inclusion of r^{-4} terms would significantly alter the shape of the potential in the region of the minimum, their effect is less pronounced in the strongly repulsive regions of the curve which are typical of most of the repulsive scattering interactions studied here.

Total Inelastic Cross Section

A series of careful angular scans were executed at several CO^+ incident energies to measure total inelastic intensity from CO^+ + Ar collisions as a function of scattering

angle; from which total inelastic cross sections as a function of θ, normalized at 0^{o}, were obtained (Figure 34). The curves in Figure 34 are qualitatively similar to elastic differential cross section curves for similar systems (107), and out to 10^{o} are fit reasonably well by equation 40.

Comparison with Amdur's Potential

Jordan et al. (108) have used high energy scattering of neutral particles to obtain an empirical potential of interaction for the CO-Ar system given by

$$V(r) = \frac{551}{r^{6.99}} \qquad (42)$$

for $2.09<r<2.68$. As shown in Figure 35, Shin's $U(r,\chi)$ lies at a considerably higher energy in this region. $U(r,\chi)$ may, of course, be fitted to $V(r)$ by proper choice of Lennard-Jones parameters, and this has been done at $r=2.43$ Å with two different sets of D and σ, to investigate the effect on b^{*} of such a "fitted Shin potential."

Results are shown in Table 4, where the b^{*}'s on each line result in similar predicted probabilities of vibrational excitation on collision.

Pure Rotational Excitation

The energy loss spectra of Figures 25-32 are strikingly indistinct in terms of resolving vibrational structure, considering the very narrow energy spread of incident

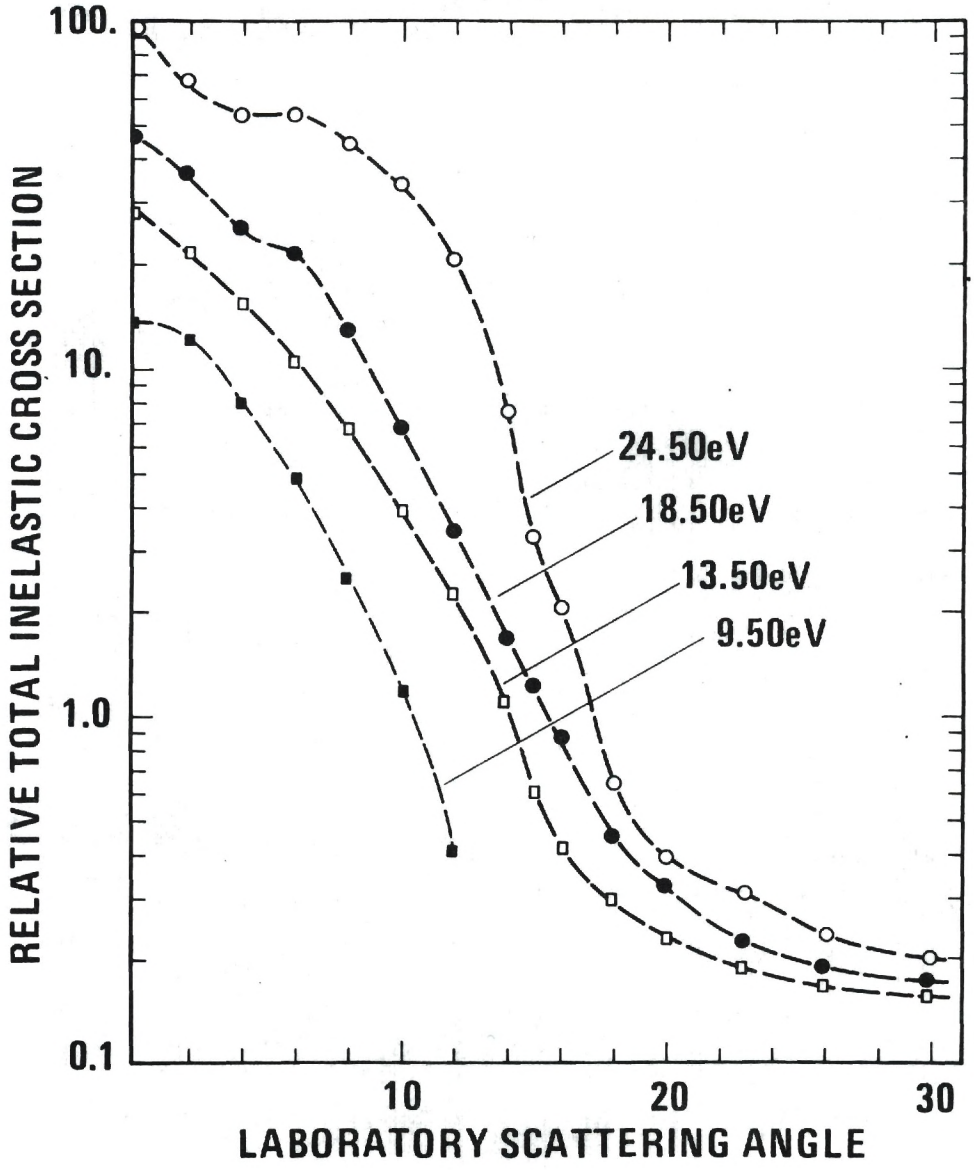

Figure 34. Relative Total Inelastic Cross Section for Inelastic Scattering of CO^+ by Ar *vs.* LAB Scattering Angle for Several Incident Ion Kinetic Energies.

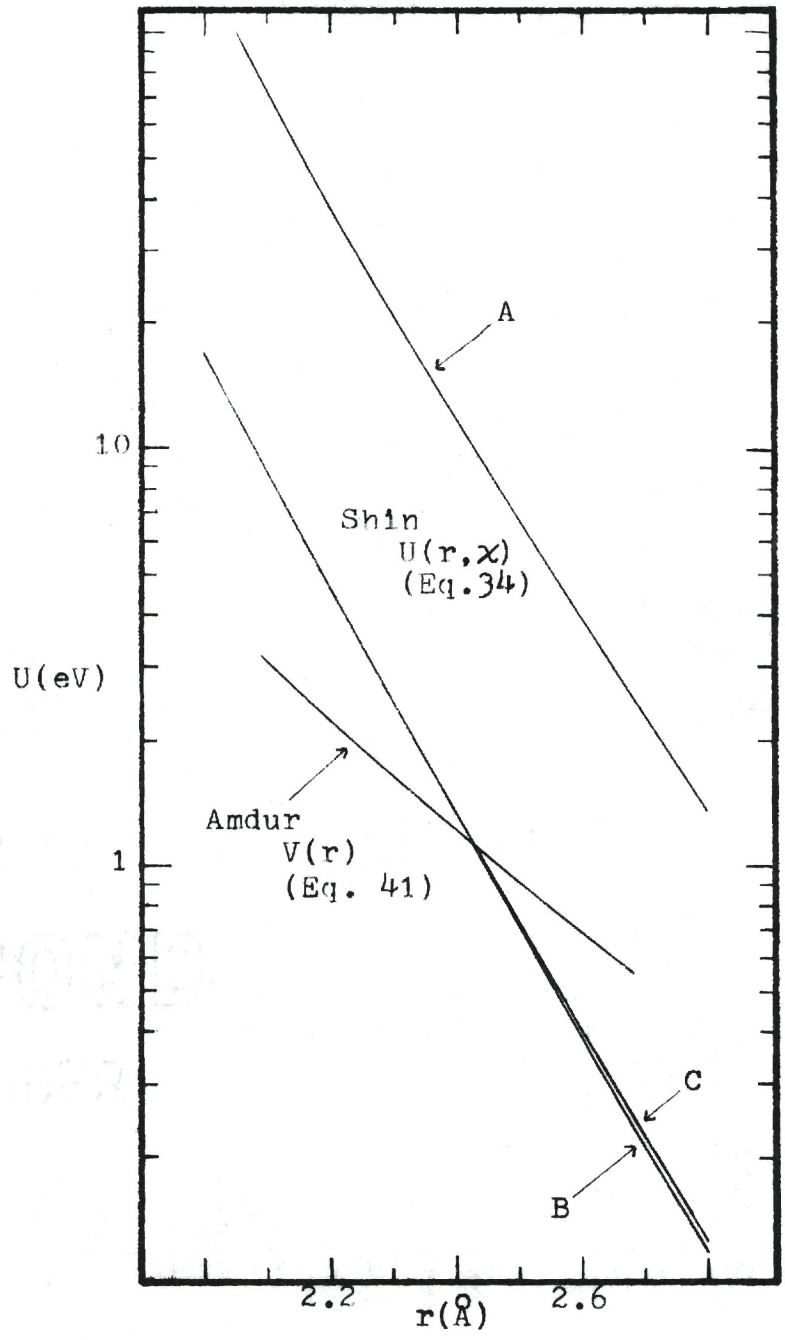

Figure 35. Comparison of Shin and Amdur Potentials.
(A: $D=1.612\times10^{-14}$erg, $\sigma=3.504$Å;
B: $D=2.000\times10^{-14}$erg, $\sigma=2.900$Å;
C: $D=1.612\times10^{-14}$erg, $\sigma=2.950$Å.)

Table 4. b* from "Fitted" Shin's U(r).*

Curve A	Curve B	Curve C
b*=0.50	b*=0.70	b*=0.70
0.55	0.75	0.75
0.60	0.80	0.80
0.65	0.85	0.85
0.70	0.90	0.90
0.75	0.95	0.95
0.80	1.00	1.00
0.85	1.05	1.05
0.90	1.05	1.10
0.95	1.10	1.15
1.00	1.15	1.20
1.05	1.20	1.25
1.10	1.25	1.30

See figure 35. Error in b due to fitting experimental data is ±0.05.

CO^+ and the removal of most out-of-plane kinetic energy components from target Ar. This "band" structure clearly indicates simultaneous rotational-vibrational excitation to be occurring on collision.

A closer look at the energy loss spectrum below the $v=0\rightarrow1$ transition (Figure 36) reveals structure corresponding to pure rotational transitions of CO^+ on collision with Ar. This is the first reported observation of pure rotational transitions induced by collision performed by an ion beam experiment.

The solid curve, centered on the E_e-E_i zero of energy, represents a typical primary CO^+ kinetic energy distribution. The rotational population of CO^+ at 473^o K, the temperature of the ion source, is sketched in the upper part of Figure 36, with the most highly populated level (J=9) directly above $E_e-E_i=0$. Error bars in Figure 36 give an indication of difficulties arising from subtraction of a large elastic intensity from a large total scattered ion intensity to get a small inelastic intensity. This uncertainty is only a problem for very small energy loss, as the elastic peak is quite narrow.

Since most ($\sim$51%) of the incident CO^+ is in rotational levels J=5-13 and most ($\sim$51%) of the pure rotational excitation on collision produces CO^+ in $J\simeq25-31$, the approximate average change in rotational state of CO^+ by collision with Ar at 5.5 eV and 0^o is $J\simeq19$. Table 5 lists the ap-

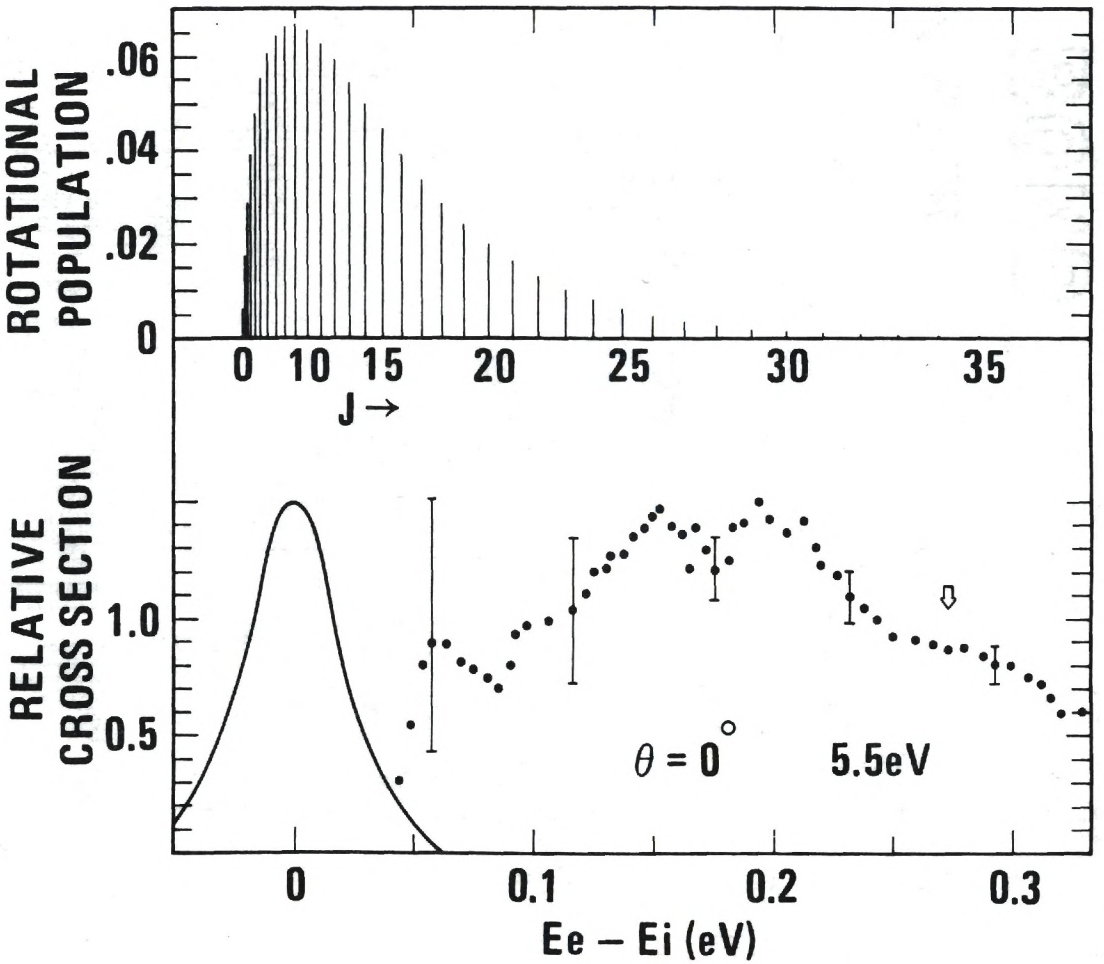

Figure 36. Relative Cross Section for Inelastic CO^+ - Ar Collisions as a Function of Inelastic Energy Loss for 5.5 eV CO^+ Ions at 0^o LAB Angle. (The Solid Curve on the Bottom of this Figure is the Reactant CO^+ Ion Kinetic Energy Distribution. The Points are Experimental Inelastic Energy Loss Data with the Bars through Several Points Giving Typical Error Limits throughout the Energy Range. The Top Portion of this Figure Gives the Incident CO^+ Rotational Distribution.)

Table 5. Approximate Average Rotational Excitation in CO^+ + Ar Collisions. (Incident CO^+ Assumed to be in J=9 Rotational Energy Level; Error in ΔJ is Approximately ±10.)

	$\theta=0^o$	$\theta=6^o$
E_o(eV) =	ΔJ=	ΔJ=
24.50	19	19
21.50	19	20
18.50	16	20
15.50	16	18
13.50	20	19
11.50	18	20
9.50	15	19
7.50	18	20
5.50	18	18
4.00		18
3.98	14	
3.10	7	18
2.25	7	
1.56	7	

proximate average change in rotational quantum number for pure rotational excitation induced by collision. At $\theta=0^{o}$ a general trend of greater excitation with increasing incident energy is observed, qualitatively similar to that noted for vibrational excitation. Also, scattering to $\theta=6^{o}$ appears to involve greater rotational excitation than to $\theta=0^{o}$ for a given incident CO^{+} kinetic energy.

Conclusions

An oriented nonlinear encounter model for vibrational excitation of CO^{+} on collision with Ar adequately describes experimental energy loss spectra at small laboratory scattering angles, while multiquantum transitions at large angles contradict such a model. The impact parameters characteristic of the collisions decrease with increasing angle and increase with increasing energy. Pure rotational excitation with a large change in rotational quantum number is observed at small scattering angles.

CHAPTER VII

CONCLUSIONS

Collision-induced dissociations of 2000 eV diatomic molecule ions were found to result in product ion velocity distributions consistent with a mechanism that involves Franck-Condon type transitions between electronic states in the excitation of the reactant species. Unimolecular decomposition of triatomic ions was found to product CO^+ and NO^+ with considerable internal excitation.

Low energy collisions of H_3^+ with Ne result in vibrational excitation, and the inelastic kinetic energy losses furnish an estimate of the vibrational frequencies of H_3^+.

Inelastic low energy collisions of CO^+ with Ar yield energy loss spectra which confirm predictions of an oriented nonlinear encounter model for vibrational excitation by collision at small scattering angles, while multiquantum vibrational excitation observed at larger angles contradicts such a model. Simultaneous rotational excitation of CO^+ is observed in the energy loss spectra, with the relative importance of rotational transitions increasing at smaller scattering angles.

LITERATURE CITED*

1. F. W. Aston, Cambridge Phil. Soc. 19, 317 (1920); also Mass Spectra and Isotopes (E. Arnold and Co., London, 1933), 2nd ed.

2. H. D. Smyth, Rev. Mod. Phys. 3, 347 (1931).

3. N. V. Fedorenko, V. V. Aforsimov, R. N. Il'in, and D. M. Kaminker, Soviet Phys.-JETP 9, 267 (1959).

4. A. C. Riviere and D. R. Sweetman, Proc. Phys. Soc. (London) 78, 1215 (1961).

5. A. P. Irsa and L. Friedman, J. Chem. Phys. 34, 330 (1961).

6. J. Guidini, Comp. Rend. 253, 829 (1961).

7. R. Caudano, J. M. Delfosse, and J. Steyaert, Ann. Soc. Sci. Bruxelles 76, 127 (1963).

8. C. F. Barnett, M. Rankin, and J. A. Ray, Proc. Intern. Conf. Ionization Phenomena Gases 6th (Paris) 1, 63 (1963).

9. D. R. Bates, K. Ledsham, and A. L. Stewart, Phil. Trans. Roy. Soc. London A246, 215 (1953).

10. S. Cohen, J. R. Hiskes, and R. J. Riddell, Jr., Phys. Rev. 119, 1025 (1960); also University of California Rad. Lab. Rept. No. UCRL-8871 (1959).

11. G. Dunn, J. Chem. Phys. 44, 2592 (1966).

12. J. M. Peek, Phys. Rev. 134, A877 (1964); 140, A11 (1965).

13. J. E. G. Farina, Proc. Phys. Soc. (London) 90, 323 (1967).

---

*The abbreviations used herein conform to those adopted by the IUPAC and AIP as described in the List of Periodicals, Chem. Abstr. 55, 1J (1961) and later supplements.

14. J. M. Peek, T. A. Green, and W. H. Weihofen, Phys. Rev. 160, 117 (1967).

15. "Plasma Physics" selected reprints published for the American Institute of Physics, New York, 1965. In particular R. F. Post, Rev. Mod. Phys. 28, 338 (1956); C. F. Barnett, P. R. Bell, J. S. Luce, E. D. Shipley, and A. Simon, Progress in Nuclear Energy-Plasma Physics and Thermonuclear Research (Pergamon Press, Inc., New York, 1959), Ser. XI, Vol. 1.

16. G. W. McClure, Phys. Rev. 140, A769 (1965).

17. D. K. Gibson and J. Los, Physica 35, 258 (1967).

18. D. K. Gibson, J. Los, and J. Schopman, Phys. Letters 25A, 634 (1967).

19. M. Vogler and W. Seibt, Z. Phys. 210, 337 (1968).

20. J. Wm. McGowan and L. Kerwin, Can. J. Phys. 42, 972 (1964).

21. Wm. McGowan and L. Kerwin, Can. J. Phys. 41, 316 (1963).

22. F. M. Rourke, J. C. Sheffield, W. D. Davis, and F. A. White, J. Chem. Phys. 31, 193 (1959).

23. C. E. Melton and G. F. Wells, J. Chem. Phys. 27, 1132 (1957).

24. V. H. Dibeler and H. M. Rosenstock, J. Chem. Phys. 39, 3106 (1963).

25. F. H. Field and J. L. Franklin, Electron Impact Phenomena and the Properties of Gaseous Ions (Academic Press, New York, 1957).

26. T. F. Moran and J. R. Roberts, J. Chem. Phys. 49, 3411 (1968).

27. D. Rapp and P. Englander-Golden, J. Chem. Phys. 43, 1464 (1965); L. J. Kieffer and G. H. Dunn, Rev. Mod. Phys. 38, 1 (1966); and reference 25.

28. C. E. Berry, Phys. Rev. 78, 597 (1950).

29. K. H. Purser, P. H. Rose, N. B. Brooks, R. P. Bastide, and A. B. Wittkower, Phys. Lett. 6, 176 (1963).

30. H. H. Harris and M. E. Russell, J. Chem. Phys. 47, 2267 (1967); 47, 2270 (1967).

31. V. H. Dibeler and H. M. Rosenstock, J. Chem. Phys. 39, 1326 (1963); H. M. Rosenstock, V. H. Dibeler, and F. N. Harllee, ibid. 40, 591 (1964); N. D. Coggeshall, ibid. 37 2167 (1962); F. W. McLafferty, Interpretation of Mass Spectra (W. A. Benjamin, Inc., New York, 1966).

32. R. W. Nicholls and A. L. Stewart in Atomic and Molecular Processes, D. R. Bates, Ed. (Academic Press Inc., New York, 1962).

33. P. A. Fraser, Can. J. Phys. 32, 515 (1954).

34. T. F. Moran and L. Friedman, J. Chem. Phys. 42, 2391 (1965); R. W. Nicholls, J. Res. Natl. Bur. Std. 65A, 451 (1961).

35. D. C. Jain and R. C. Sahni, Intern. J. Quantum Chem. 2, 325 (1968).

36. J. E. Hesser, J. Chem. Phys. 48, 2518 (1968).

37. D. L. Judge and G. L. Weissler, J. Chem. Phys. 48, 4590 (1968).

38. V. D. Meyer, A. Skerbele, and E. N. Lassettre, J. Chem. Phys. 43, 3769 (1965); S. M. Silverman and E. N. Lassettre, J. Chem. Phys. 41, 3727 (1964).

39. D. W. Vance, Phys. Rev. 169, 263 (1968).

40. A. J. Blake and J. H. Carver, J. Chem. Phys. 47, 1038 (1967).

41. R. S. Stolarski, V. A. Dulock, Jr., C. E. Watson, and A. E. S. Green, J. Geophys. Res. 72, 3953 (1967).

42. E. W. Thomas, G. D. Bent, and J. L. Edwards, Phys. Rev. 165, 32 (1968).

43. R. G. Bennett and F. W. Dalby, J. Chem. Phys. 31, 434 (1959).

44. J. Desesquelles, M. Dufay, and M. C. Poulizac, Phys. Let. 27A, 96 (1968).

45. F. R. Gilmore, J. Quant. Spectry. Radiative Transfer 5, 369 (1965).

46. P. M. Hierl and J. L. Franklin, J. Chem. Phys. 47, 3154 (1967).

47. L. J. Kieffer and R. J. Van Brunt, J. Chem. Phys. 46, 2728 (1967).

48. G. H. Dunn, Phys. Rev. Letters 8, 62 (1962); G. H. Dunn and L. J. Kieffer, Phys. Rev. 132, 2109 (1963).

49. V. Čermák and Z. Herman, Collection Czech. Chem. Commun. 30, 1343 (1965).

50. R. K. Asundi, G. J. Schulz, and P. J. Chantry, J. Chem. Phys. 47, 1584 (1967).

51. J. W. McGowan, DASA Reaction Rate Handbook (Defense Atomic Support Agency, Washington, D. C., 1967), Chap. 15.

52. R. I. Schoen, J. Chem. Phys. 40, 1830 (1964).

53. G. M. Lawrence, J. Quant. Spectry. Radiative Transfer 5, 359 (1965).

54. R. W. Nicholls, Can. J. Phys. 40, 1772 (1962).

55. P. H. Krupenie, The Band Spectrum of Carbon Monoxide, National Standard Reference Data System NSRDS-NBS5 (U. S. Government Printing Office, Washington, D. C., 1966).

56. C. E. Watson, V. A. Dulock, Jr., R. S. Stolarski, and A. E. S. Green, J. Geophys. Res. 72, 3961 (1967).

57. E. H. Fink and K. H. Welge, Z. Naturforsch. 23a, 358 (1968).

58. B. R. Turner, J. A. Rutherford, and D. M. J. Compton, J. Chem. Phys. 48, 1602 (1968).

59. D. W. Turner and D. P. May, J. Chem. Phys. 45, 471 (1966).

60. P. Natalis and J. E. Collin, Chem. Phys. Letters 2, 414 (1968).

61. R. W. Nicholls, Can. J. Phys. 43, 1390 (1965).

62. W. McGowan and L. Kerwin, Can. J. Phys. 42, 2086 (1964).

63. J. E. Collin and P. Natalis, Chem. Phys. Letters 2, 194 (1968).

64. J. E. Collin and P. Natalis, Int. J. Mass Spectry. Ion Phys. 1, 483 (1968).

65. V. Cermak, J. Chem. Phys. 44, 3781 (1966); V. Cermak, Collection Czech. Chem. Commun. 33, 2739 (1968).

66. R. F. Mathis, B. R. Turner, and J. A. Rutherford, J. Chem. Phys. 49, 2051 (1968).

67. K. H. Welge, J. Chem. Phys. 45, 1113 (1966).

68. M. Lenzi and H. Okabe, Ber. Bunsenges. Phys. Chem. 72, 168 (1968).

69. R. S. Freund and W. Klemperer, J. Chem. Phys. 47, 2897 (1967).

70. H. Ehrhardt and A. Kresling, Z. Naturforsch. 22a, 2036 (1967).

71. J. D. Morrison, J. Chem. Phys. 22, 1219 (1954).

72. J. W. McConkey, D. J. Burns, and J. M. Woolsey, Proc. Phys. Soc. 1B, 71 (1968).

73. G. Herzberg, Spectra of Diatomic Molecules (D. Van Nostrand Company, Inc., Princeton, N. J., 1950).

74. J. Schoettler and J. P. Toennies, Z. Physik 214, 472 (1968).

75. W.-D. Held, J. Schoettler, and J. P. Toennies, Chem. Phys. Letters 6, 304 (1970).

76. P. F. Dittner and S. Datz, J. Chem. Phys. 49, 1969 (1968).

77. J. H. Moore and J. P. Doering, Phys. Rev. Letters 23, 564 (1969).

78. J. H. Moore and J. P. Doering, J. Chem. Phys. 52, 1692 (1970).

79. T. F. Moran and P. C. Cosby, J. Chem. Phys. 51, 5724 (1969).

80. P. C. Cosby and T. F. Moran, J. Chem. Phys. 52, 6157 (1970).

81. J. J. Thomson, Phil. Mag. 24, 209 (1912).

82. E. W. McDaniel, V. Cermak, A. Dalgarno, E. E. Ferguson, and L. Friedman, Ion-Molecule Reactions (Wiley-Interscience, New York, 1970).

83. P. C. Cosby, The Effect of Ionic Collisions on the Internal Energy of Diatomic Molecules (M. S. Thesis, Georgia Institute of Technology, 1969).

84. J. J. Leventhal and L. Friedman, J. Chem. Phys. 49, 1974 (1968); 50, 2928 (1969).

85. R. F. Borkman, J. Chem. Phys. 53, 3153 (1970).

86. R. E. Christoffersen, J. Chem. Phys. 41, 960 (1964).

87. M. E. Schwartz and L. J. Schaad, J. Chem. Phys. 47, 5325 (1967).

88. F. O. Ellison, N. T. Huff, and J. C. Patel, J. Am. Chem. Soc. 85, 3544 (1963).

89. A. G. Pearson, R. D. Poshusta, and J. C. Browne, J. Chem. Phys. 44, 1815 (1966).

90. J. O. Hirschfelder, J. Chem. Phys. 6, 795 (1938).

91. K. Takayanagi, Progr. Theoret. Phys. (Kyoto) 25, 1 (1963).

92. K. Takayanagi, Advan. At. Mol. Phys. 1, 149 (1965).

93. D. Rapp and T. Kassal, Chem. Rev. 69, 61 (1969).

94. D. Secrest and B. R. Johnson, J. Chem. Phys. 45, 4556 (1966).

95. J. D. Kelley and M. Wolfsberg, J. Chem. Phys. 44, 324 (1966).

96. C. E. Treanor, J. Chem. Phys. 43, 532 (1965); 44, 2220 (1966).

97. E. Kerner, Can. J. Phys. 36, 371 (1958).

98. H. K. Shin, Chem. Phys. Letters 3, 125 (1969).

99. H. K. Shin, J. Phys. Chem. 73, 4321 (1969); J. Chem. Phys. 49, 3964 (1968).

100. R. N. Fox, R. L. Fitzwilson, and E. W. Thomas, J. Phys. E 3, 36 (1970).

101. H. Wollnik, "Electrostatic Prisms," Focusing of Charged Particles. II. A. Septier, Ed. (Academic Press, Inc., New York, 1967).

102. W. R. Gentry, E. A. Gislason, B. H. Mahan, and C.-W. Tsao, J. Chem. Phys. 49, 3058 (1968).

103. R. L. Champion and L. D. Doverspike, J. Chem. Phys. 49, 4321 (1968).

104. J. O. Hirschfelder, C. F. Curtiss, and R. B. Bird, Molecular Theory of Gases and Liquids (Wiley, New York, 1964).

105. E. W. McDaniel, Collision Phenomena in Ionized Gases (Wiley, New York, 1964).

106. J. D. Kelley and M. Wolfsberg, J. Chem. Phys. 24, 1266 (1956).

107. W. Aberth and D. C. Lorentz, Phys. Rev. 182, 162 (1969).

108. J. E. Jordan, S. O. Colgate, I. Amdur, and E. A. Mason, J. Chem. Phys. 52, 1143 (1970).

VITA

Frederick Petty began life in Mobile, Alabama, on November 30, 1944, as the son of Frederick Cecil and Mary Hudak Petty. Shortly thereafter he moved to South America to spend his childhood in Peru and Ecuador.

Mr. Petty graduated from Forest Lake Academy, Maitland, Florida, in 1961, and entered Southern Missionary College, Collegedale, Tennessee, from which he emerged with a Bachelor of Arts degree in English, cum laude, in 1965.

A pleasant but penurious year of teaching junior high school in Rocky Face, Georgia, propelled Petty into graduate school in 1966 at Georgia Tech.

Frederick Petty (Sagittarius) and Karen Fleming (Aries) were married in 1967 and have added no progeny to our overpopulated planet.

Mr. Petty is a member of the American Physical Society, the Georgia Conservancy, Friends of the Earth, Zero Population Growth, Planned Parenthood, and Mensa.